

QUASIGEOSTROPHIC FLOWS AND TURBULENCE

IN A ROTATING HOMOGENEOUS FLUID

BY

Alain Colin de Verdiere

Ingénieur, Ecole Supérieure de Physique et chimie de la Ville de Paris
(1973)

SUBMITTED IN PARTIAL FULFILLMENT OF THE
REQUIREMENTS FOR THE DEGREE OF
DOCTOR OF SCIENCE

at the

MASSACHUSETTS INSTITUTE OF TECHNOLOGY

and the

WOODS HOLE OCEANOGRAPHIC INSTITUTION

August, 1977

Signature of Author.....
Joint Program in Oceanography, Massachusetts Institute
of Technology - Woods Hole Oceanographic Institution,
and Department of Earth and Planetary Sciences, and
Department of Meteorology, Massachusetts Institute of
Technology, August 1977

Certified by.....
Thesis Supervisor

Accepted by.....
Chairman, Joint Oceanography Committee in the Earth
Sciences, Massachusetts Institute of Technology -
Woods Hole Oceanographic Institution

~~Withdrawn~~
WITHDRAWN
MASS. INST. TECH.
MAR 16 1978
FROM
MIT LIBRARIES



Room 14-0551
77 Massachusetts Avenue
Cambridge, MA 02139
Ph: 617.253.5668 Fax: 617.253.1690
Email: docs@mit.edu
<http://libraries.mit.edu/docs>

DISCLAIMER OF QUALITY

Due to the condition of the original material, there are unavoidable flaws in this reproduction. We have made every effort possible to provide you with the best copy available. If you are dissatisfied with this product and find it unusable, please contact Document Services as soon as possible.

Thank you.

Due to the poor quality of the original document, there is some spotting or background shading in this document.

Quasigeostrophic flows and turbulence in a
rotating homogeneous fluid

by

Alain Colin de Verdiere

Submitted to the Department of Physical Oceanography
on August 1977 in partial fulfillment of the requirements
for the Degree of Doctor of Science

from

Massachusetts Institute of Technology

and

Woods Hole Oceanographic Institution

ABSTRACT

Stimulated by new evidence from both "in situ" oceanic observations and results from numerical modelling, a laboratory study of quasigeostrophic flow and turbulence in a rotating homogeneous fluid has been undertaken. Two dimensional turbulence driven by a uniform distribution of sources and sinks which oscillate in time, can be fairly well reproduced in this context. Inertial time scales are about ten times smaller than Ekman spin-up time, and typical Reynolds numbers reach 2000. The observations emphasize the spectral tendency of the energy containing eddies. The case of no topography is first discussed. In steadily forced turbulence, it is observed that the energy containing scale is significantly larger than the forcing scale. In the decaying stage the red cascade is observed and rates of interaction are measured. Theoretical arguments for both behaviors are presented; the former concerning the forced turbulence case is believed to be new.

The forcing is next applied over various large scale topographies, modelling the geophysical beta effect. The polar beta plane geometry preserves the above spectral characteristics but at the same time introduces anisotropy into the flow pattern. A broad westward mean flow develops in the north and is surrounded by a belt of cyclones lying on its southward side. The calculated second-order Eulerian mean flows induced by steadily and uniformly forced Rossby waves in a long zonal channel, exhibit much of the same momentum distribution in the inertial regime. In contrast, the

ABSTRACT (cont.)

"sliced cylinder" geometry which possesses no closed geostrophic contours drastically modifies the above picture. Both mean flow production and a large scale tendency for the eddies are inhibited. The geographical distribution of the eddy intensities and scales is now wildly inhomogeneous.

The second aspect of this work is a study of the interaction of Rossby waves with mean flows. A zonally travelling, forced wave is generated near the southern boundary of a polar beta plane. Due to energy radiation in the free interior and (or) potential vorticity mixing by the finite amplitude waves, a westward zonal flow develops. The effect of the mean flow upon the forced steady waves is to weaken the anticyclones and intensify the cyclones. Pressure time series reveal a growth of harmonics and general spectral broadening as the waves travel freely inwards, suggesting active nonlinear interactions. An experimental test of Rhines' (1977) potential vorticity mixing theory is also presented at free latitudes. The decay period when the driving is suppressed shows that a net transfer from the waves to the mean flow kinetic energy occurs. Connection with hydrodynamic stability theory is discussed.

Interaction of Rossby waves with an externally generated westward mean flow allows one to make a controlled study of the critical layer problem. For small amplitude waves, the mean flow is accelerated in the entire region between the forcing and the critical latitude which acts as a wall for mean wave momentum. In nonlinear runs the steady profile of the westward flow indicates that an accelerating force is acting everywhere, revealing the increasing transmission of wave momentum through the critical layer. At the same time, pressure measurements near the critical point show considerable fine structure developing over a long time scale.

The third part deals with steady isolated source-sink flows in the sliced cylinder geometry. The response of the fluid to a meridionally oriented steady dipole extends exclusively westward of the forcing. The viscously balanced solutions are discussed and relevance to oceanic abyssal circulation is emphasized. With strong driving, the combination of a cyclone to the north and an anticyclone to the south is absolutely stable although the reverse configuration is not. A connection with a certain class of free, steady, isolated, inertial solutions developed recently by Stern (1976) is made.

Thesis Supervisor: Dr. Peter B. Rhines

Title: Senior Scientist

Acknowledgments

This study would have never reached the present state without the help (direct or indirect) of many people. I am particularly grateful to Peter Rhines who aroused my interest in the theory of low frequency flows. Throughout the course of this work, his physical insight and perceptive encouragement never ran out and ultimately taught me how to think rather than what to do. The experimental part was initiated by Angus McEwan from C.S.I.R.O. (Australia). His considerable drive revealed to me a new philosophy for devising laboratory experiments and his help is gratefully acknowledged here. I had many useful conversations with Jack Whitehead on both the theoretical aspects and experimental craftsmanship needed for this study. Moreover he enthusiastically allowed me to mess around in his hydrodynamics laboratory for two years. I address many thanks to Audrey Williams who typed this manuscript and whose sailing oriented conversation reminded me of my ultimate goals. Robert Frazel helped me to solve many practical problems when the appearance of things seemed to be definitely odd.

Many people helped me to put my English writing up on a more scholastic basis and Anglo-Saxon readers will certainly appreciate their efforts.

The DGRST (FRANCE) and the Joint Program in Oceanography, Massachusetts Institute of Technology and the Woods Hole Oceanographic Institution offered a fellowship for the first two years. The National Science Foundation under Grant OCE75-21 674 and the Office of Naval Research under Contract N00014-74-CO262-NR-083-004 supported this study for the final two years.

TABLE OF CONTENTS

	Page
Abstract	
Acknowledgments	
List of Figures	
Introduction	
Part one	
I. The quasigeostrophic vorticity equation	
II. General description of the laboratory techniques	
Part two	
I. Two dimensional turbulence in a rotating fluid of constant height	
II. Two dimensional turbulence on a polar β plane	
A. Spectral evolution of free and forced eddies	
B. Forced Rossby waves in an infinitely long channel	
III. Two dimensional turbulence in the sliced cylinder model	
Part three	
I. Mean flow rectification by topographic Rossby waves	
A. Rossby wave resonance, wave stresses	
B. Potential vorticity mixing and associated finite amplitude effects	
C. The period of decay	
II. The Rossby wave critical layer	
A. Linear theory of the Rossby wave-zonal flow interaction	
B. The laboratory experiment	
Part four	
I. The small amplitude dipole circulation. Experiments and theory	
II. The finite amplitude dipole circulation	
Conclusion	
Bibliography	
Biographical note	

List of Figures

Figure Number		Page Number
1-1	Low pass filtered velocity time series at mooring #564 (37° 30'N, 55° 00'W).	16
1-2	Time - longitude plot of stream function inferred from objective maps of 1500 m currents along 28°N by Freeland, Rhines, Rossby (1975).	17
2-1	Sketch and definition of the topography.	26
2-2	Details of the forcing mechanism: a hydraulic commutator.	26
2-3	The electrical circuit used with the capacitance probe.	31
3-1	Steady state of f-plane forced 2D turbulence. The black segment indicates the forcing scale. Laboratory parameter values are: $\omega/f = 3.8 \times 10^{-2}$, $E = 3 \times 10^{-6}$, $\frac{U'}{fL} = 1.5 \times 10^{-2}$, $\frac{U'L}{\nu} = 988$.	39
3-2	Decaying state of f-plane 2D turbulence as evolved from figure 3-1.	39
3-3	Contours of the transverse correlation function.	41
3-4	Table of parameters and statistics of forced 2D turbulence on an f-plane.	42
3-5	Table of parameters and statistics of decaying 2D turbulence on an f-plane.	48
3-6	Variations of the eddy scales and kinetic energy with ω/f in steadily forced 2D turbulence on an f-plane:	43
	(a) Integral scale and zero-crossing	
	(b) Kinetic energy and enstrophy.	

List of Figures (cont.)

Figure Number		Page Number
3-7	Correlation coefficient in f-plane 2D turbulence: (a) steady state transverse correlation (b) steady state longitudinal correlation (c) decaying state transverse correlation (d) decaying state longitudinal correlation Laboratory parameter values are as in figure 3-1.	49
3-8	Turbulent flow on a polar β -plane. Experimental parameter values are $\Omega = 3.92$ rad/s, $\omega = 0.4$ rad/s, $H = 14.5$ cm, $w = 0.12$ cm/s (a) Transient state (b) Steady state.	52
3-9	The zonally averaged steady mean flow.	54
3-10	The viscous, long wavelength limit: (a) The mean flow RS, the vorticity mixing term DF and the forcing term FT (b) The Stokes drift SD.	65
3-11	The viscous, short wavelength limit: (a) The mean flow RS, the diffusive term DF, and the forcing term FT (b) The Stokes drift SD.	66
3-12	The inertial, short wavelength limit ($\epsilon/\omega = 0.1$).	68

List of Figures (cont.)

Figure Number		Page Number
3-13	The inertial, long wavelength limit ($\epsilon/\omega = 0.1$, $k = 0.628$) for various frequencies (a) $\omega = \omega_0$ (b) $\omega_3 < \omega < \omega_5$ (c) $\omega = \omega_5$ (d) $\omega_5 < \omega < \omega_7$ (e) $\omega = \omega_{11}$	69
3-14	The Eulerian and Lagrangian mean flows in the inertial long wavelength limit ($k = 0.628$, $\epsilon/\omega = 0.1$, $\omega_3 < \omega < \omega_5$); RS is the Eulerian mean flow, SD is the Stokes drift, UL is the Lagrangian mean flow.	71
3-15	The mean flow response to a forcing frequency spectrum containing 9 discrete frequencies in the inertial regime.	68
3-16(a)	2D turbulence in the sliced cylinder model: the steadily forced case. Laboratory parameter values are $\Omega = 5.1$ rad/s, $\omega = 0.43$ rad/s, $H = 25$ cm, $\alpha = 0.23$, $w = 0.12$ cm/s.	78
	(b) The state of decay as evolved from figure 3-16(a).	
3-17	Experimental results for 2D turbulence in the sliced cylinder.	80
3-18	The fluid response to an isolated, oscillating dipole in the sliced cylinder ($\alpha = 0.095$). The darker cir- cular region in the east indicates the position of the dipole.	84

List of Figures (cont.)

Figure Number		Page Number
4-1	The Rossby wave transients induced by the switch-on of the westward travelling ring forcing at the outer boundary. Laboratory parameter values are $\Omega = 3.06$ rad/s, $\omega = 0.4$ rad/s, $H = 7$ cm, $Q = 363$ cm ³ /s, $E = 6.8 \times 10^{-5}$, $U/fL = 2.5 \times 10^{-2}$.	89
4-2	The steady state. The parameters are as in figure 4-1.	89
4-3	The resonance curves: plain curves are deduced from the theory, dots represent experimental values. (a) The near-field region (b) The far-field region.	93
4-4	Pressure time series for different directions of propagation of the forcing: (a) retrograde (b) prograde (c) stationary.	96
4-5	Locus of wavenumbers excited by a westward propagating forcing. Arrows indicate the direction of the group velocity relative to the forcing.	98
4-6	Long exposure photograph, revealing the tilt of the particle orbits.	98

List of Figures (cont.)

Figure Number		Page Number
4-7	<p>Experimental values of the zonally averaged fields as a function of radial distance in the topographic Rossby wave experiment. The experimental parameter values are $\Omega = 3.83$ rad/s, $\omega = 0.4$ rad/s, $H = 10$ cm, $Q = 363$ cm³/s.</p> <p>(a) westward mean flow and Reynolds stress</p> <p>(b) eddy and mean kinetic energy.</p>	100
4-8	<p>Experimental comparison of mean flow acceleration and potential vorticity flux at free latitudes:</p> <p>(a) the initial value problem</p> <p>(b) the steady state</p> <p>Laboratory parameter values are $\Omega = 4.05$ rad/s, $\omega = 0.442$ rad/s, $Q = 360$ cm³/s, $H = 7$ cm.</p>	103 104
4-9	<p>Wave pressure time series for three distinct frequencies of excitation</p> <p>(a) $\omega = 0.216$ rad/s</p> <p>(b) $\omega = 0.167$ rad/s</p> <p>(c) $\omega = 0.124$ rad/s</p> <p>Other parameter values which were held fixed, are: $\Omega = 3.7$ rad/s, $H = 9$ cm, $Q = 300$ cm³/s.</p>	106
4-10	<p>The pressure autospectra corresponding to figure 4.9</p> <p>(a) $\omega = 0.216$ rad/s</p> <p>(b) $\omega = 0.167$ rad/s</p> <p>(c) $\omega = 0.124$ rad/s.</p>	107

List of Figures (cont.)

Figure Number		Page Number
4-11	A pressure time series showing the fast disappearance of the waves when the driving is switched-off.	109
4-12	The decay period of the velocity field: (a) the steady state (b) the decaying state 20 sec after switch-off.	110
4-13	Temporal decay of mean and eddy kinetic energy.	111
4-14	Experimental values of potential vorticity as a function of radial distance as obtained from figure 4-12 (a).	113
4-15	The perturbation phase velocity as a function of $R_o = \frac{\beta b^2}{U_o \pi^2}$ (a) imaginary part (b) real part.	118
4-16	The geometry of the critical layer problem.	124
4-17	Parameter regime for the critical layer experiment.	137
4-18	(a) The mean flow used in the critical layer experiments (b) The steady state of run 1.	138
4-19	Mean flow and Reynolds stress as calculated from run 1 (a) transient and steady state of the zonal flow: curves #2, 4, and 16 correspond to photographs taken respectively at $T/5$, $T/2$ and $4T$, T being the Ekman spin-up time (b) The steady state Reynolds stress (#16).	139
4-20	The transient (a) and steady state (b) of the non-linear run 2.	141

List of Figures (cont.)

Figure Number		Page Number
4-21	Averaged fields as calculated from run 2	143
	(a) Mean zonal flow: curves #1, 2, 4 and 17 correspond to photographs taken respectively at $T/11$, $T/3.5$, $T/1.7$ and $5T$, T being the Ekman spin-up time.	
	(b) Reynolds stress and eddy kinetic energy in the steady state (#17)	
4-22	(a) Pressure time series near the critical level for a run analogous with 2	144
	(b) Pressure autospectra of the above signal at $5T'$ and $31T'$, T' being the wave period.	145
5-1	Time dependent response to an impulsive $\delta(t)$ function dipole in the sliced cylinder. Laboratory parameter values are $\Omega = 5.43$ rad/s, $\alpha = 0.2$, $H = 22$ cm.	148
5-2	The flow induced by a steady dipole	149
	(a) transient	
	(b) steady state	
	Laboratory parameter values are $\Omega = 4.18$ rad/s, $\alpha = 0.095$, $H = 25$.	
5-3	The results of Stommel et al. (1958)	151
	(a) Transport lines	
	(b) Their experiments	
5-4	The streamline pattern of theoretical solution (6)	156
	(a) $\delta = 0.15$	
	(b) $\delta = 0.58$	

List of Figures (cont.)

Figure Number		Page Number
5-5	Meridional flow profiles with stable configuration A. Laboratory parameter values are the following: L the source-sink distance is kept fixed at 8 cm	162

	$\frac{U_{MAX}}{\beta L^2}$	$\frac{U_{MAX}}{RL}$	$L_R = \frac{R}{\beta}$	$L_\beta = \left(\frac{U_{MAX}}{\beta}\right)^{\frac{1}{2}}$
①	1.53	15.2	0.8	9.9
②	0.84	7.6	0.87	7.3
③	0.27	6.8	0.3	4.2

5-6	Two runs with unstable configuration B. (a) $U/\beta L^2 = 1.2$ (b) $U/\beta L^2 = 12.7$	164
-----	--	-----

INTRODUCTION

Because of its immediate consequences for mankind and the relative ease by which observations could be collected, the description of the general circulation of the atmosphere started early in the eighteenth century and attracted many scientific minds for its understanding. With increasing technology, more information was soon gathered on the weather itself and it was quickly realized that an explanation of the former implied knowledge of the second order statistics of the latter. In view of the complexity of the problem, progress toward an understanding of the detailed dynamics has been slow compared to refinement in weather forecasting due to increased numerical capability. One can say that the same story holds true for the ocean, as revealed by the past fifty years.

By use of geostrophy, routine density observations made it possible to infer the baroclinic part of the general oceanic circulation. In the last decade, deep mooring technology allowed a look at what had been summarized in the deep water as levels of no motion. The presence of a very energetic oceanic "weather" exceeding the mean circulation by at least an order of magnitude was discovered, suggesting a very strong interaction between the mean and the eddy part of the flow. During the last Mid-Ocean Dynamics Experiment MODE (1973), a particular eddy was tracked for about three months. A time scale on the order of a month and a length scale of about 100 km were soon agreed upon to define mesoscale eddies, whose signature seems to appear now just about everywhere in the world ocean.

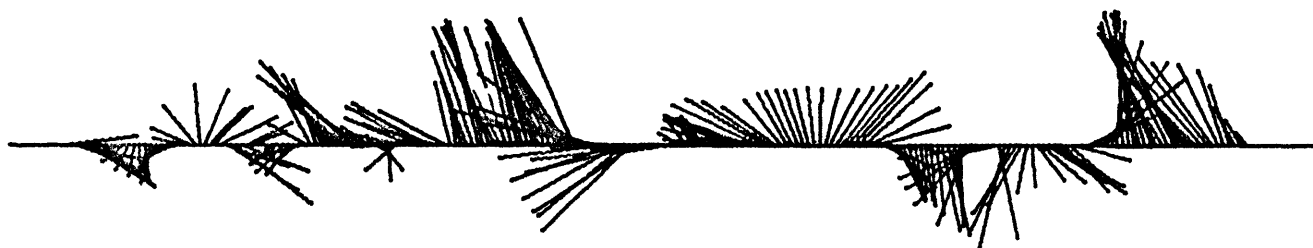
The inherent complexity of the large-scale equilibrium of the ocean necessitates the use and understanding of simpler models focusing on one aspect of the dynamics, which may later be mixed in more sophisticated

studies. It should be remembered that the coincidence of observations with theoretical results do not teach us anything unless we are able to understand the model in simple physical terms. The aim of the present study is to provide part of a physical understanding of certain barotropic flows of a homogeneous fluid over various smooth topographies in a simply shaped rotating container. Most of this work is devoted to flows in which topography and rotation combine to provide a restoring force acting on individual fluid particles which models the beta-effect for quasigeostrophic flows on a rotating earth.

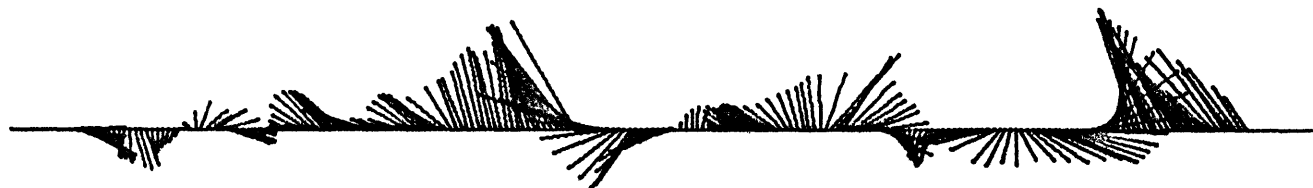
It is important to point out what are the underlying oceanic evidences for undertaking such studies of low frequency homogeneous flows on a beta plane: there is first an historical factor which prompts studies of barotropic flows. Only the velocity shear can be inferred from density measurements and in the past it has been customary practice to assume a level of no motion to infer absolute velocities. Secondly there is now evidence that the vertical structure of low frequency flows can be summarized in terms of a barotropic mode and the first few baroclinic modes (Gould, Schmitz, and Wunsch (1974), Richman (1976)). Recently as part of the POLYMODE experiments, time dependent energetic, almost depth independent flows have been reported from Array II by Schmitz (1977) (see fig. 1-1). As for the importance of the BETA effect, we might advance that it was one of the most ubiquitous features to have come out of the MODE experiment. Eulerian features, such as current veering, or temperature jumps were seen to be strongly spatially correlated on given latitude lines with a time lag indicating phase propagation to the west. Figure 1-2 is an example of such a correlation computed by Freeland, Rhines and Rossby (1975) using the Sofar float body of data. Theoretical

MOORING 564

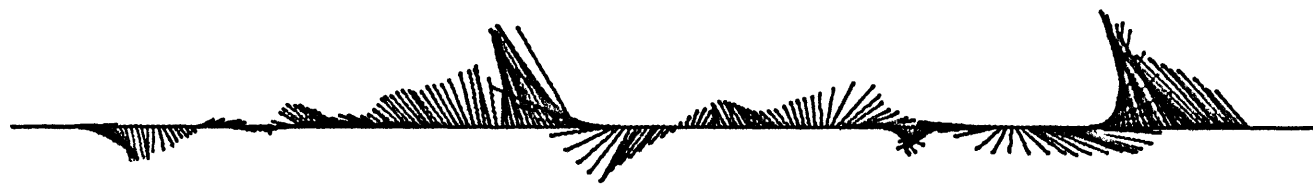
5641A10G24A
027 M



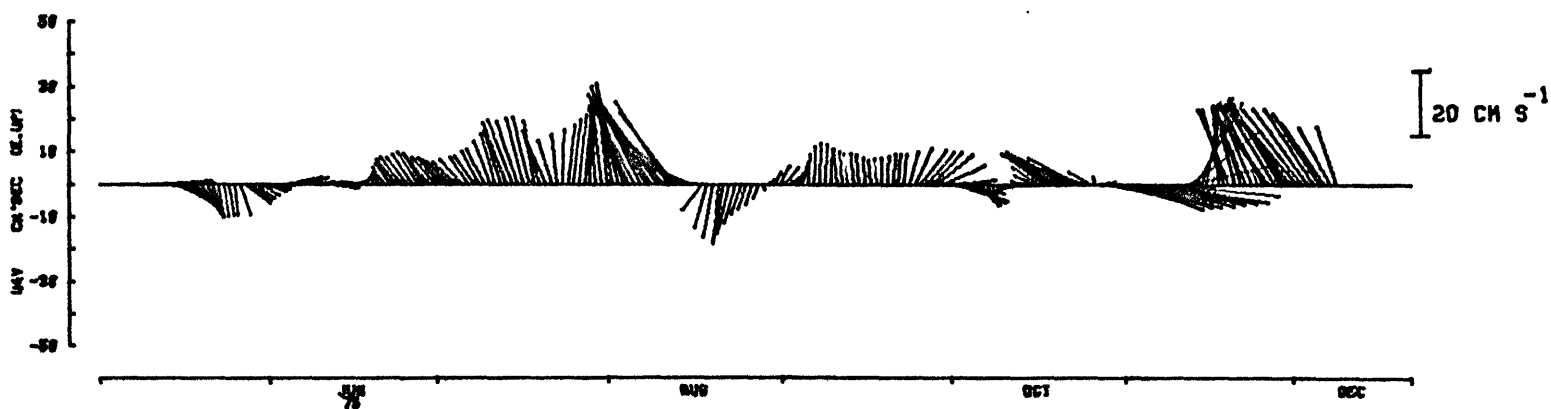
5643A10G24A
1020 M



5644A10G24A
1020 M

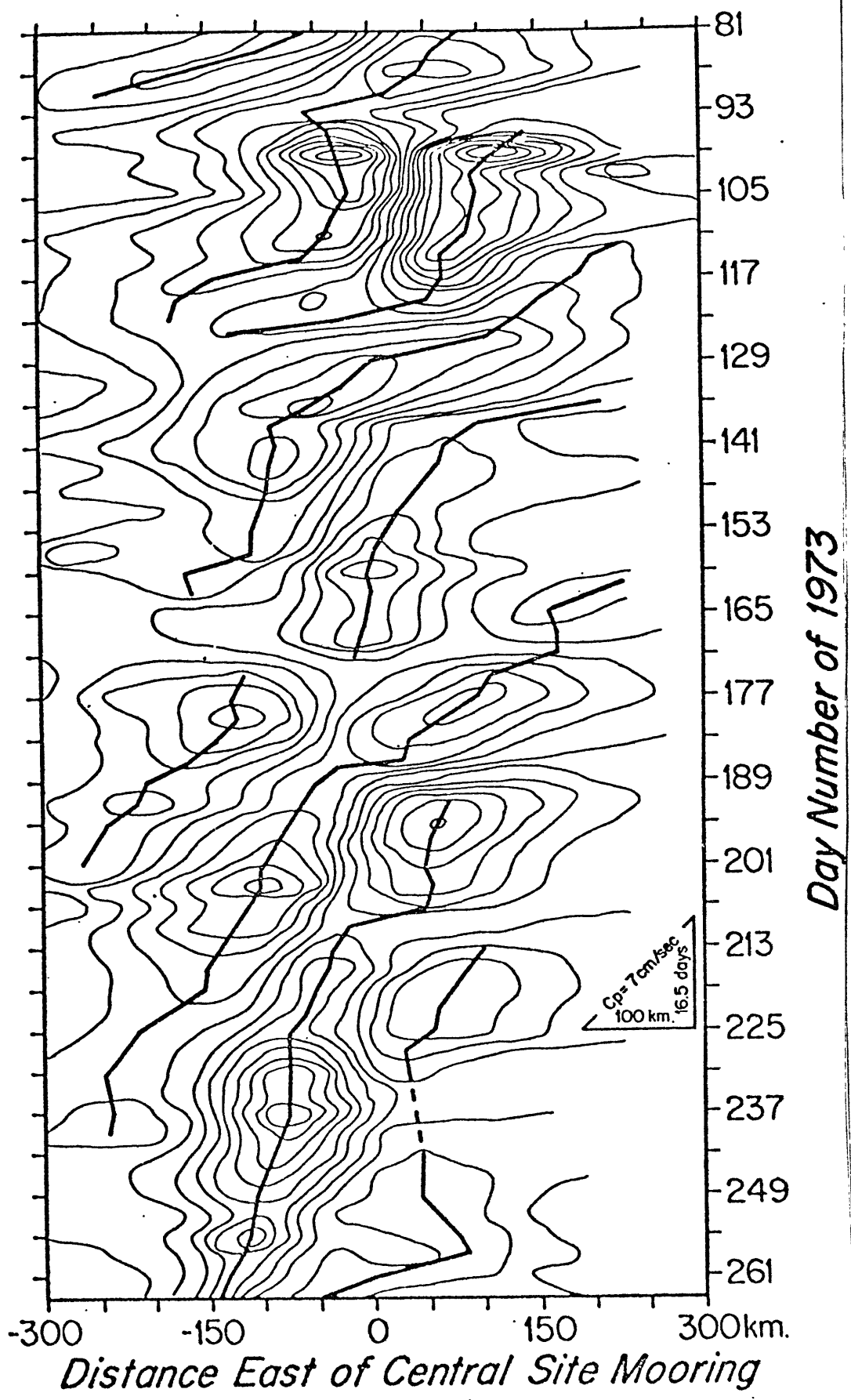


5645A10G24A
1010 M



7-80 40 01-77

1-1 Low pass filtered velocity time series at mooring #564
(37° 30'N, 55° 00'W).



1-2 Time - longitude plot of stream function inferred from objective maps of 1500 m currents along 28°N by Freeland, Rhines, Rossby (1975).

evidence for the importance of the role of the depth independent mode, even in a stratified ocean, is abundant. We might retain the following: it is the barotropic mode which is responsible for the vertically integrated water transport and therefore we might expect its important role in the dynamics of large scale circulation. Recent numerical experiments by Rhines (1976) bear very strongly on this point. In his 2-layer numerical ocean, Rhines considered a number of free spin down experiments: a field of eddies with initial horizontal scales smaller than the internal Rossby radius of deformation and a vertical scale typical of a baroclinic mode evolved at first independently in each layer to a scale close to the Rossby radius, then locking of vorticities of like sign occurred in the vertical to achieve an equivalent state of barotropy. At the other end of the spectrum, initially large scale baroclinic eddies break up into smaller scale eddies on the order of the deformation scale, as classical baroclinic instability would predict, but there again one observes a modal migration toward barotropy with the accompanying transfer from potential to kinetic energy. As those states are reached, simpler ideas concerning the subsequent evolution of a homogeneous, two-dimensional fluid may be applied.

Most of the results obtained in the present work come from observations of laboratory flows. It is believed that the application of laboratory modelling to two-dimensional turbulence studies is rather new and meant to supplement numerical simulation of these processes. On the other hand the modelling of geophysical geostrophic flows in the laboratory has already reached an advanced stage with works by Phillips and Ibbetson (1967), Beardsley (1969, 1975). These studies have focussed primarily on realisations of flows governed by linear theory and its

first non linear corrections. The good ability of these experiments to reproduce features predicted by theory made us believe even more strongly that laboratory experiments were perfectly suited to observe flows with higher "energy levels" remembering the inherent difficulty that numerical models have to cope with: namely the finite number of interactive scales of motions, limiting the inviscidness of the model.

In the first part of this study we will present a derivation of the quasigeostrophic equations of motion for a laboratory ocean and a general description of the basic experimental techniques used. Reference will be made constantly to this part in order to eliminate unnecessary repetition of some material when looking at a particular problem. The second part is concerned with geostrophic eddy-eddy turbulent interaction in three different geophysical contexts:

(1) - f plane model with no topography

(2) - polar beta plane model: the topography is a paraboloid dish, and the geostrophic contours are closed

(3) - sliced cylinder model: the topography consists of a linearly sloping top and the geostrophic contours are open.

In these three cases we are looking at the interaction of turbulent eddies in the presence of dissipation and external forcing. The evolution toward a statistical equilibrium is also described. Global conservation laws for energy and potential entrophy are used for describing the transient and final states of the eddies identified by their length scales and their energy level. Attention is especially directed in cases (2) and (3) to formulate theoretical mechanisms for explaining the observed anisotropy and inhomogeneities of the turbulence.

We will describe in the third part work involved with the classical

interaction of Rossby waves and mean flows. As shown first experimentally by Whitehead (1975) and theoretically by Rhines (1976) freely propagating, finite amplitude Rossby waves are susceptible of generating westward mean flows; that problem is reconsidered in more detail, having in mind a more complete comparison between theory and experiment. By doing so, some new features of the interaction will be revealed. With the versatility of our forcing mechanism it was very tempting to try an interaction between a steady Rossby wave and an externally forced westward mean flow. This particular problem known in the literature as the critical layer problem (when the phase speed of the wave matches the speed of the mean flow at some "critical level") was a unique opportunity to reveal how the time dependent interaction and the steady state depended on the strength of the wave; these features are very difficult to obtain by either analytical or numerical techniques and furthermore they might help in other contexts as the internal gravity wave-mean flow interaction.

Finally the last part deals with apparently simpler steady flows produced by steady dipole forcing in the sliced cylinder model. Relevance of these observations to earlier laboratory studies of abyssal flow is particularly discussed. An interesting instability of the flow is put into evidence and physical arguments will be put forward to hint at its nature.

PART ONE

I. The quasigeostrophic vorticity equation

In this chapter we seek to derive in some orderly fashion the vorticity equation valid for quasi two dimensional flows in a rapidly rotating container when the fractional depth change due to the topography is small. This problem has been looked at in depth by Greenspan (1969) and much of his formalism will be followed, adding in, at the outset, the possible effect of a free surface upon the dynamics. Going through the scaling, is a necessary operation to list accurately the approximations involved and define appropriate non dimensional parameters.

The geometry used is sketched on figure 2-1. The forcing method used throughout this study is to impose the vertical velocity at the bottom through a distribution of sources and sinks. The analysis which will follow is essentially inviscid, the role of the Ekman layers being to impose at any horizontal solid boundary an additional vertical velocity whose value has been calculated once for all in terms of the interior vorticity. This will be incorporated further along in the analysis.

The inviscid form of the Navier-Stokes equation is:

$$(1) \quad \begin{aligned} \frac{\partial \vec{q}}{\partial t} + \vec{q} \cdot \nabla \vec{q} + 2\Omega \vec{k} \times \vec{q} &= - \frac{\nabla p}{\rho} \\ \nabla \cdot \vec{q} &= 0 \end{aligned}$$

with boundary conditions:

$$\text{at } z = -H, \vec{q} \cdot \vec{k} = w(x, y, t)$$

$$\text{at } z = \alpha d(x, y) + \eta(x, y, t), \vec{q} \cdot \vec{k} = \alpha \vec{q} \cdot \nabla d + \frac{D\eta}{Dt}$$

$f = 2\Omega$ is the Coriolis parameter.

α specifies the order of magnitude of the topographic slope.

H is the mean depth of the container.

Introducing the non dimensional primed quantities:

$$(x', y') = (x, y)/L, \quad z' = z/H, \quad t' = \alpha\Omega t, \quad q' = q/\varepsilon\Omega L$$

$$p' = P/(\varepsilon\Omega^2 L), \quad \eta' = \eta/(\varepsilon\Omega^2 L), \quad \text{where } \varepsilon \text{ is the Rossby number } \frac{U}{\Omega L}.$$

The scaling for pressure and wave height come from geostrophy and hydrostatics respectively. The non dimensional equations become after dropping the primes:

$$\alpha \frac{\partial \vec{q}}{\partial t} + \varepsilon \vec{q} \cdot \nabla \vec{q} + 2 \vec{k} \times \vec{q} = - \nabla p$$

$$(2) \quad \nabla \cdot \vec{q} = 0.$$

By linearizing the upper boundary condition, one obtains:

$$\text{at } z = 0, \quad (\vec{k} - \alpha \nabla d) \cdot \vec{q} - \alpha \text{Fr} \delta \frac{\partial p}{\partial t} - \varepsilon \text{Fr} \delta \vec{q} \cdot \vec{\nabla} p = 0$$

$$(3)$$

$$\text{at } z = -\delta, \quad \vec{q} \cdot \vec{k} = w_0 + W_\varepsilon$$

where the following parameters introduced themselves:

$$\text{Fr is the Froude number } \frac{\Omega^2 L^2}{gH},$$

$$\delta \text{ is the aspect ratio } H/L,$$

W_ε is the Ekman pumping introduced arbitrarily at this point as an additional requirement on the vertical velocity at the bottom and

$$\text{whose value is: } w_\varepsilon = \frac{1}{2} E^{1/2} \nabla \times \vec{q}, \text{ and}$$

$$E \text{ is the Ekman number } \nu/\Omega H^2.$$

The logical procedure is now to consider α as the small parameter of the problem, and rescale ε as αR_0 , E as $\alpha^2 E_0$, and w as αw_0 . Doing so introduces naturally the quasigeostrophy of the motions. One now expands pressure and velocity fields as a perturbation series in α :

$$\vec{q} = \vec{q}_0 + \vec{q}_1 + \dots \quad p = p_0 + \alpha p_1 + \dots$$

Substituting into the set of equations (2) and (3), one is led to the following sequence:

$$0\text{th order: } 2\vec{k} \times \vec{q}_0 = -\nabla p_0$$

(4)

$$\nabla \cdot \vec{q}_0 = 0$$

Taking the curl of the momentum equation gives $\frac{\partial \vec{q}_0}{\partial z} \equiv 0$ and we deduce $\vec{q}_0 \cdot \vec{k} \equiv 0$, which states the Taylor-Proudman theorem, i.e., that the velocity field is essentially two dimensional at 0th order in α .

The first order balance removes the degeneracy of the problem through the use of the upper boundary condition:

1_{st} order:

$$\frac{\partial \vec{q}_0}{\partial t} + R_0 \vec{q}_0 \cdot \nabla \vec{q}_0 + 2\vec{k} \times \vec{q}_1 = -\nabla p_1$$

$$(5) \quad \nabla \cdot \vec{q}_1 = 0$$

$$\text{at } z = 0, \quad \vec{q}_1 \cdot \vec{k} - Fr \cdot \delta \cdot \frac{\partial p_0}{\partial t} - R_0 \cdot Fr \cdot \delta \vec{q}_0 \cdot \nabla p_0 - \nabla d \cdot \vec{q}_0 = 0$$

$$\text{at } z = -\delta, \quad \vec{q}_1 \cdot \vec{k} = w_0 + \frac{1}{2} E_0^{1/2} \nabla \times \vec{q}_0.$$

From (4), one derives immediately that $\vec{q}_0 \cdot \nabla p_0 \equiv 0$, and taking the curl of the momentum equation in the set (5) yields:

$$2 \frac{\partial \vec{q}_1}{\partial z} = \nabla \times \left(\frac{\partial \vec{q}_0}{\partial t} + R_0 \vec{q}_0 \cdot \nabla \vec{q}_0 \right).$$

Integrating in z :

$$\vec{q}_1 = \frac{z}{2} \cdot \nabla \times \left(\frac{\partial \vec{q}_0}{\partial t} + R_0 \vec{q}_0 \cdot \nabla \vec{q}_0 \right) + \vec{A}$$

where \vec{A} is an arbitrary constant.

$$\text{at } z = 0, \quad \vec{A} \cdot \vec{k} = \nabla d \cdot \vec{q}_0 + Fr \cdot \delta \cdot \frac{\partial p_0}{\partial t}, \text{ and}$$

$$\text{at } z = -\delta, \quad -\frac{\delta}{2} \cdot \vec{k} \cdot \nabla \times \left(\frac{\partial \vec{q}_0}{\partial t} + R_0 \vec{q}_0 \cdot \nabla \vec{q}_0 \right) + \vec{A} \cdot \vec{k} =$$

$$w_0 + \frac{1}{2} E_0^{1/2} \nabla \times \vec{q}_0.$$

Eliminating \vec{A} between the two last equations and taking an order 1 aspect ratio δ , gives the following:

$$\frac{\partial}{\partial t} \nabla \times \vec{q}_0 + R_0 \vec{q}_0 \cdot \nabla (\nabla \times \vec{q}_0) - 2\nabla d \cdot \vec{q}_0 - 2Fr \frac{\partial p_0}{\partial t} = -2w_0 - E_0^{1/2} \nabla \times \vec{q}_0.$$

From (4) it is seen that $\frac{p_0}{2}$ is a stream function ψ_0 , hence:

$$\frac{\partial \nabla^2 \psi_0}{\partial t} + R_0 J(\psi_0, \nabla^2 \psi_0) - 2J(\psi_0, d) - 4 Fr \frac{\partial \psi_0}{\partial t} = -2w_0 - E_0^{1/2} \nabla^2 \psi_0,$$

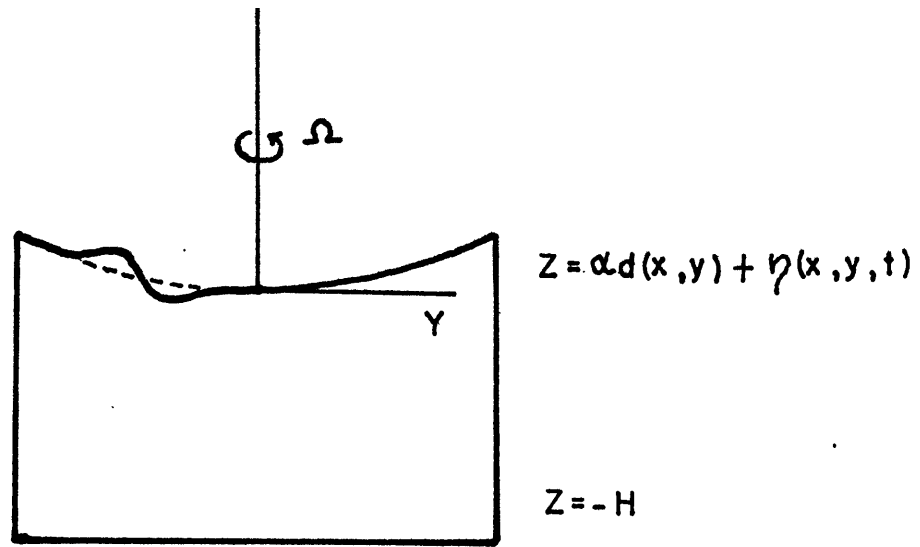
J being the Jacobian operator.

At this stage, it is interesting to rewrite the final equation in dimensional variables:

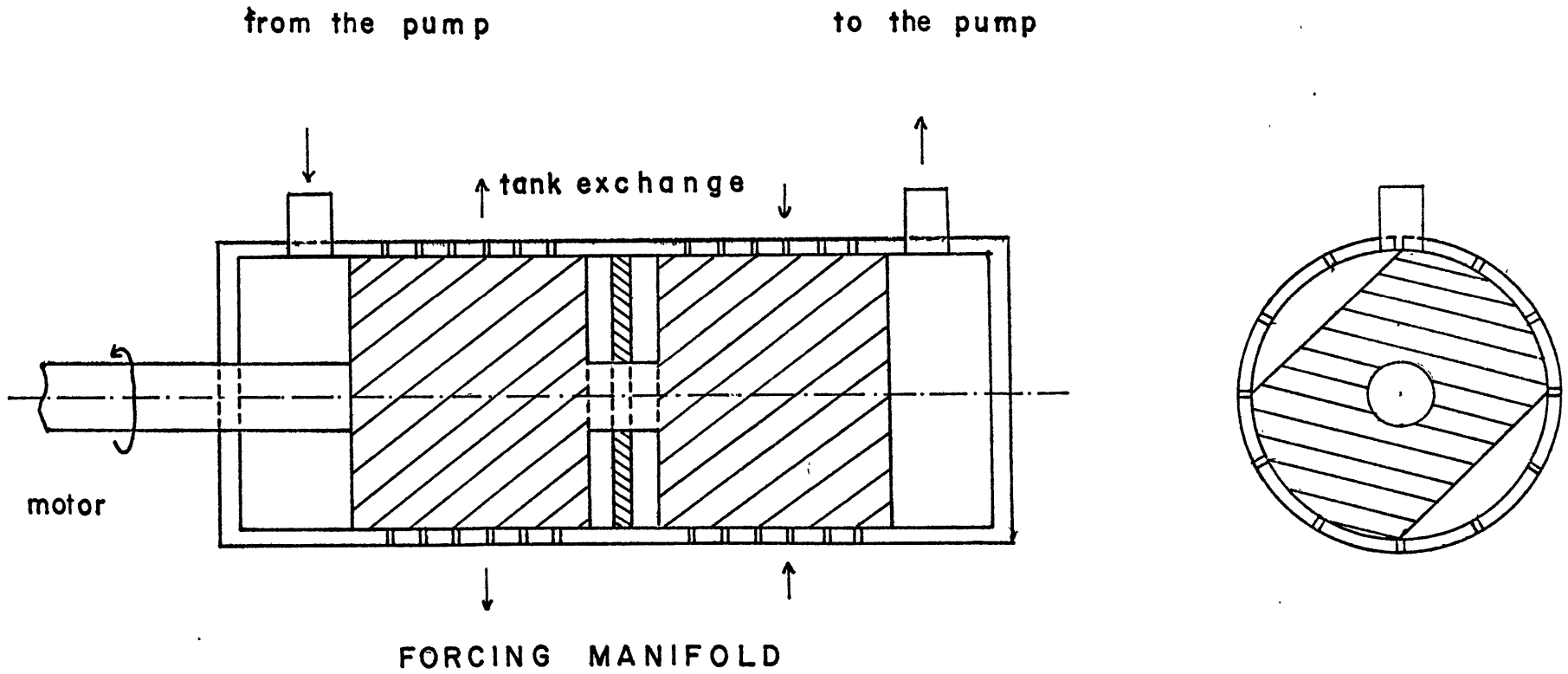
$$(6) \quad \left\{ \frac{\partial}{\partial t} + J(\psi_0, \nabla^2 \psi_0) \right\} \nabla^2 \psi_0 - \frac{f\alpha \nabla d \cdot \vec{k} \times \nabla \psi_0}{H} - \frac{1}{\lambda^2} \frac{\partial \psi_0}{\partial t} = -R \nabla^2 \psi_0 - \frac{fw}{H}$$

where $\lambda = gH/f^2$ is the Rossby radius of deformation and $R = \Omega E^{1/2}$ is the inverse of the Ekman spin down time.

When a second solid horizontal boundary is imposed at the top, (6) is still valid by taking the limit $\lambda \rightarrow \infty$ and doubling the value of R . This last vorticity equation is to be studied using as a lateral boundary condition the fact that the streamfunction must be constant along vertical walls, consistent with our neglect of lateral friction altogether. The present study is not concerned with the role of the Stewartson layers required to bring the velocity to zero at a solid wall. A simple scale analysis shows that away from those boundary layers, the ratio of dissipation of vorticity by lateral friction over Ekman friction is of order $\frac{H}{L^2} \left(\frac{v}{\Omega}\right)^{1/2}$, usually small for good sized eddies, justifying our earlier inviscid interior treatment. Nevertheless, when necessity dictates a look at internal scales of order $HE^{1/4}$, lateral friction will be included directly into (6).



2-1 Sketch and definition of the topography.



2-2 Details of the forcing mechanism: a hydraulic commutator

II. General description of the laboratory techniques

Earlier workers modelling geostrophic motion in the laboratory have used a wide variety of forcing mechanisms: Phillips and Ibbetson used a paddle mechanism mounted on a vertical axis, Beardsley considered the differential rotation of the upper horizontal lid. It turned out that these devices are well suited for generating weak amplitude motions but rather unsatisfactory to produce 2D turbulence. On the other hand it was realized that a distribution of sources and sinks on the bottom of the tank would force the fluid quite naturally by stretching and compressing the water column, modelling rather well the forcing mechanism of large scale flows in both atmosphere and ocean. A consequence of that choice was the ease by which both spatial and temporal aspects of the generating mechanism could be varied.

The design of the forcing mechanism is due to A. McEwan and it is perhaps worth describing it in detail for ways of operating that component might be unclear at first sight. The heart of the system is a manifold shown in figure 2-2, whose function is to distribute fluid from the pump toward the drilled holes at the bottom of the tank: 72 sources and 72 sinks can be used on the two independent sections of the manifold. The rotating shaft of the manifold is driven by a reversible, variable speed electric motor. It is the rotation of the shaft which allows sources and sinks to be turned on and off periodically at each revolution. Varying the spatial distribution of the sources and sinks in the container and on the manifold provides a large number of combinations of forcing patterns. Two of the main combinations used are described. When the spatial distribution in the container is periodic, careful wiring of the connecting tubes onto the manifold allows the modelling

of a travelling forcing wave. At the other extreme when the spatial distribution in the container is uniform, random wiring onto the manifold provided an adequate forcing for generating random turbulence in which case the event that two sources (sinks) chosen randomly in the tank have the same phase, occurs with a probability of 0.166. The forcing used in turbulence studies is thus periodic in time and pseudo random in space with the meaning described above.

The experimental tank itself is a polyester cylinder 62 cm in diameter, 30 cm high, whose bottom is covered by a 2 cm thick foam rubber sheet to allow an increase in the efficient section of sources and sinks, so reducing their jetting effects.

All the experiments are carried out on the one-meter diameter rotating table of the Woods Hole Oceanographic Institution. Its maximum rotation rate is 10 rad/sec and variations of speed are less than 0.3%. The shaft of the table is aligned to within 4 second of arc. We refer to the Ibbetson, Frazel (1965) report for more information.

Measurement techniques are twofold: photographic equipment being available, quasi-Eulerian information is obtained by taking short exposure pictures of tracer particles, and Lagrangian information needed for diffusion studies is derived from movie film. The tracer particles are neutrally buoyant polystyrene beads with typical size of 1/2 mm. Their density may be adjusted by heating them slowly up to 85°C. This is a necessary process to have a good distribution of beads in the vertical in the case of a sealed container without a free surface. The beads are translucent and lighted from the side of the tank by three fluorescent lights. At the same time, a closed circuit television system with video tape recording capability was used and found to be extremely useful to

go through exploratory runs in real time.

It might be interesting to see what is needed to do a meaningful conversion from Lagrangian to Eulerian data:

Lagrangian accelerations at a particle x' is related to its Eulerian counterpart at the fixed point X by:

$$\left(\frac{\partial v_i}{\partial t}\right)_{x'} = \left(\frac{\partial u_i}{\partial t} + u_j \frac{\partial u_i}{\partial x_j}\right)_{X=X(x',t)}$$

Integrating in time following particle x' yields:

$$(v_i)_{x'} = (u_i + \int_0^t u_j \frac{\partial u_i}{\partial x_j})_{X=X(x',t)}$$

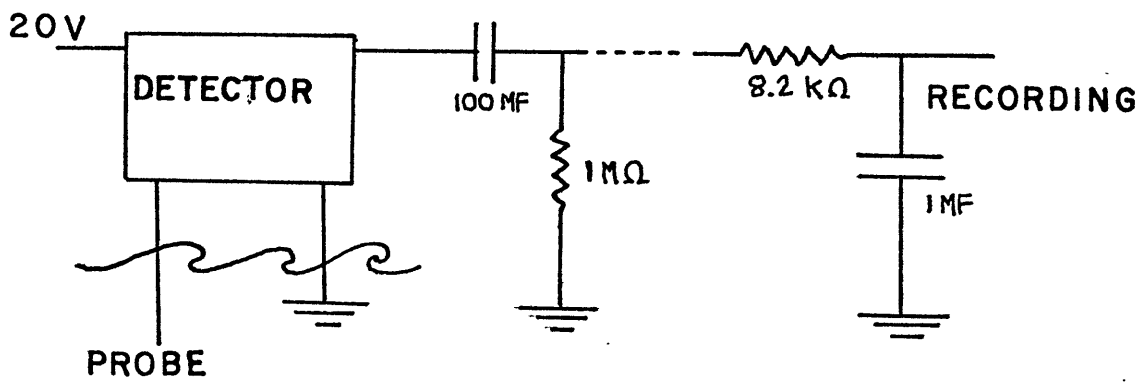
A short time expansion of the above gives:

$$(v_i)_{x'} = (u_i + 2\Delta t \frac{\partial}{\partial x_j} u_i u_j)_{x'}$$

This shows that however small Δt , short scales of motion of order $u_i \cdot \Delta t$ (if any) will bias the Eulerian estimates. One would like to reduce the exposure time Δt as much as possible without impairing the measurement of the streaklines. These were measured with an eye gauge and relative error on the velocity was about 5%. In some of the experiments statistical information about the velocity field was needed. When the turbulence was homogeneous, spatial averaging was carried out over a particular realisation of the field. The selected sampling grid interval of 2.5 cm required the measurement of the velocity field at about 100 points. This sampling scheme was chosen empirically to guarantee

stability of the statistics (total kinetic energy, integral length scale) within 10%.

At one point, true Eulerian information, continuous in time, seemed very desirable and capacitance probes were built in order to sense the "time dependent" free surface displacement. They operate on the principle that a coated wire immersed in a fluid changes its capacity as the depth of immersion varies. The inner metallic conductor and the conducting fluid form the plates, the wire coating being the dielectric. It remains only to transform this capacity in a voltage output. This was done using McGoldrick's scheme (1969). It turns out that this device is very sensitive and linear over the range of amplitudes that we measured. The output of the detector in our experiments consists typically of a 50 mV time dependent signal superimposed on a 20 volt DC part. To suppress the DC part without too much contamination of the wave signal which has a time scale of the order of 10 sec, a high pass filter with a time constant of 100 sec is interposed. It was found necessary to set up a low pass filter at 20 Hz in front of the recording to cut down the high frequency noise caused by the slip rings of the table. The amplitude range caused by topographic Rossby waves being small (1 mm at most) a physically small probe was needed and an ordinary teflon coated wire 35 microns in diameter was chosen. Figure 2-3 shows the circuit. The detector then needed to be tuned for maximum sensitivity and linearity. At a stabilized voltage of 20 v. DC it was found that the sensitivity threshold was about 50 microns, still keeping an adequate signal over noise ratio, and that the maximum gain was about 50 mV/mm. Calibration curves were constructed for both probes at a given mean depth of immersion. This enabled absolute height measurements to be made which then could be compared in different runs,



2-3 The electrical circuit used with the capacitance probe.

provided that the mean immersion of the probe did not change. Surface tension acting on the probe element did not seem to play any detrimental role. All in all, extreme satisfaction resulted from the use of these instruments in view of their low cost and the smallness of our pressure signals.

PART TWO

At the outset, it is of informative value to compare a little more closely the respective advantages and limitations of numerical and laboratory models.

To provide a successful simulation of 2D turbulence, attention must be directed toward maximizing the number of octaves of scales susceptible to interact inertially. Lateral friction is provided at the high wavenumber end of the energy spectrum. Present numerical simulations show that a typical range of 7 octaves is available. This range of scales is of a discrete type. The Reynolds numbers associated with the energy containing eddies is around 100. In the laboratory experiments initiated here, a range of 8 to 9 octaves of scales is available between the size of the box and the viscous cut off. The great advantage over numerical experiments is that this range is continuous. Moreover the Reynolds number of the energy containing eddy is an order of magnitude larger (around 1000). On the other hand scale independent Ekman friction is overwhelmingly present with a typical ratio of Ekman spin up time over inertial time scales of only 10. As in the ocean, the laboratory model requires the additional assumptions of geostrophy and hydrostatics. Although these are usually correct in the energy containing range, difficulty might arise at the small scales of motion. Recalling from part one that geostrophy holds when ϵ is small and that the pressure remains hydrostatic if $(\epsilon\delta)^2$ is also small, evaluation of these parameters for the small scale motion show that the energy spectrum must be steeper than K^{-4} in order to secure further use of the quasigeostrophic vorticity equation(6). Thus as for the inviscid mesoscale oceanic motions, but to a lesser degree, ageostrophic effects might well appear in the laboratory context before the lateral dissipation range is reached.

Further improvements to attain higher laboratory Reynolds number, still retaining geostrophy, might prove prohibitive from an engineering point of view since it requires a larger container and higher rotation rates.

I. Two dimensional turbulence in a rotating fluid of constant height

Two dimensional turbulence has been considered an important aspect of atmospheric dynamics for the past twenty years. Both the possible relevance to certain aspects of the large scale atmosphere, and the advantage over 3D turbulence in numerical simulation favored its development. It was recognized early (Fjortoft, 1953) that conservation of both total energy and enstrophy for an inviscid fluid leads to a spectral transfer of energy toward the larger scales. At the same time, random migration of fluid particles conserving their own vorticity produces more and more convolution in the vorticity contours, transferring effectively the vorticity to smaller scales of motion. Kraichnan (1967), then, postulated that on each side of forcing wavenumber there might exist two inertial ranges: one below in which the energy spectrum is function only of the rightward energy flux and wavenumber, and one above where the vorticity spectrum is function only of the leftward vorticity flux and wavenumber, the latter yielding a K^{-3} slope for the energy spectrum. This result interested meteorologists because of observations of such a spectral slope in both temperature and horizontal wind spectra in the range of wavenumber 7-15, well above direct forcing action such as baroclinic instability of the mean zonal flow. Charney (1971) showed that after re-scaling the vertical coordinate, the same spectral slope could be expected in the case of geostrophic turbulence after hypothesizing isotropy between horizontal and vertical directions. Numerical simulations of 2D turbulence have been numerous, confirming the "red cascade" but being inconclusive concerning the predicted inertial ranges, due to lack of numerical resolution.

A laboratory experiment on two dimensional turbulence is attractive because it is free of the scale limitations of its numerical analog. Because vertical motions are inhibited by rotation in a homogeneous fluid, it was thought that tendencies toward coalescence of vortices of like sign could be detected; the measured cascade rate could then be compared with values obtained from numerical studies. No attempt was made to construct the energy spectrum although our experiments were rather high Reynolds number experiments: the actual bias due to both sampling and error measurements would have prevented meaningful comparison of spectral slope with theory. In particular, attempts to resolve the small scale contributions of the Eulerian velocity field using streak photographs are bound to be unsuccessful as shown earlier, but the small scale is crucial to the enstrophy cascade to higher wavenumbers. An important weakness of such a laboratory model is the difficulty of obtaining good statistical estimates for the various fields.

Despite these limitations the experiments were run as follows: the sources and sinks were spread out over the entire bottom with a uniform grid spacing of about 4 cm. As explained in PART I, each source (sink) was assigned a random position on the forcing manifold according to a table of random numbers. Various runs were then executed for low ratios of $\frac{\omega}{f}$, at the same maximum forcing amplitude (ω being the forcing frequency and f the Coriolis parameter). When the fluid was at rest in the rotating frame, the periodic forcing was impulsively turned on, and the turbulence allowed to reach a statistical steady state; at this point we let the motion decay freely. Short exposure photographs were made during the two stages, providing quasi-Eulerian information.

Casual observation of the flow field revealed the following facts: in the forced turbulence case, eddies initially at small forcing scale grow in size until some kind of equilibrium is reached. In the decaying turbulence case, the turbulence grows to even larger scales until the bulk of the motion is dissipated by scale independent friction. For references visualize the flow in figures 3-1, 3-2. To obtain a more objective description, a number of specific runs were analyzed quantitatively. To measure both length scales and kinetic energy for the flow, the usual procedure is to introduce spatial Eulerian correlation functions. In isotropic 2D turbulence they have some important properties, summarized below.

The correlation function is defined as:

$$R_{ij}(\vec{r}) = \overline{u_i(\vec{x}) u_j(\vec{x} + \vec{r})}$$

The bar represents a suitable average depending on the properties of the turbulence. It can be more conveniently written in terms of longitudinal and transversal correlation functions, $\overline{u^2} f(r)$ and $\overline{u^2} g(r)$ respectively:

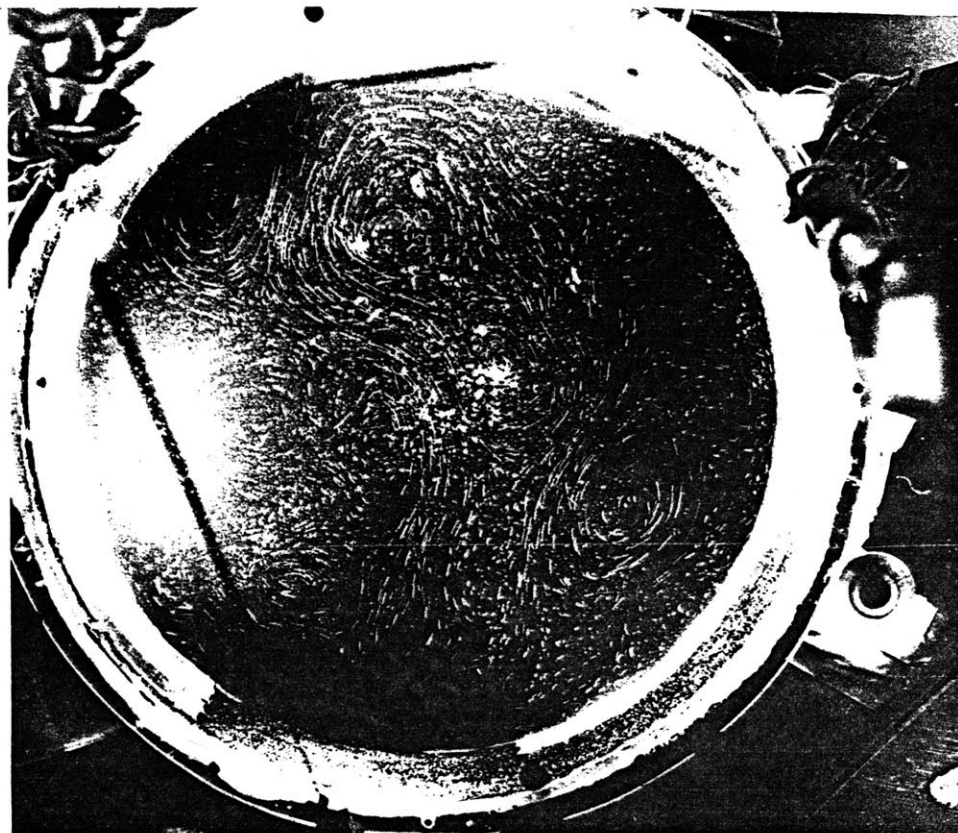
$$R_{ij}(\vec{r}) = \overline{u^2} \left[\frac{(f - g)}{r^2} r_i r_j + g \delta_{ij} \right]$$

$$\text{with } g = f + r \frac{\partial f}{\partial r}$$

From measurements of f and g , a reasonable eddy length scale can be identified, for instance by the zero crossing of $g(r)$ or by the longitudinal integral scale $L_p = \int_0^{\infty} f(r) dr$. Moreover by expanding f



3-1 Steady state of f-plane forced 2D turbulence. The black segment indicates the forcing scale. Laboratory parameter values are: $\omega/f = 3.8 \times 10^{-2}$, $E = 3 \times 10^{-6}$, $\frac{U'}{fL} = 1.5 \times 10^{-2}$, $\frac{U'L}{\nu} = 988$.



3-2 Decaying state of f-plane 2D turbulence as evolved from figure 3-1.

and g near the origin, one can obtain the microscales λ_p and λ_n :

$$\lambda_p^2 = -\frac{1}{f''(0)} \quad \text{and} \quad \lambda_n^2 = -\frac{1}{g''(0)}$$

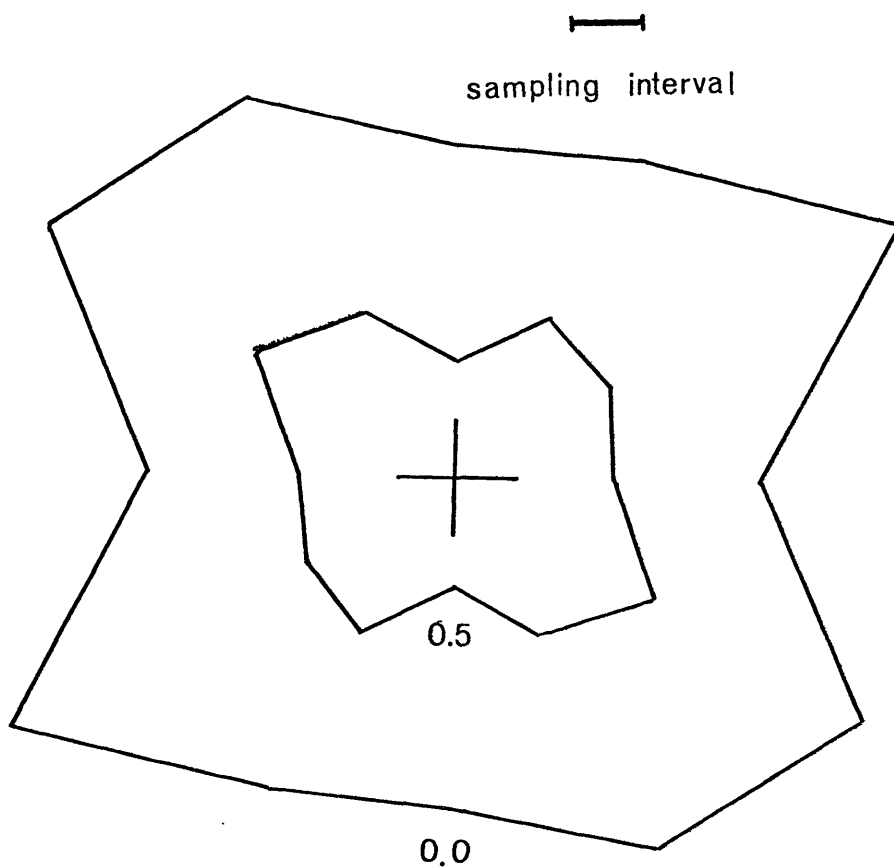
Using the relation between f and g one finds: $\frac{\lambda_p}{\lambda_n} = \sqrt{3}$.

These scales allow computation of the rms vorticity in the fluid:

$$\overline{\omega_i^2} = -\nabla^2 R_{ij} \Big|_{r=0} = 8 \frac{\overline{u^2}}{\lambda_p^2}$$

The practical procedure used to get the functions $f(r)$ and $g(r)$ from streak photographs was to accumulate product of velocity $u_p(\vec{x}_0) u_p(\vec{x}_0 + \vec{\Delta}r)$, $u_n(\vec{x}_0) u_n(\vec{x}_0 + \vec{\Delta}r)$ for a given orientation of the radius vector and various values of Δr , the sampling interval being 2.7 cm. Products with given separation $\vec{\Delta}r$ were then averaged over \vec{x}_0 , a permissible operation in view of the homogeneity of the turbulence. This was done for ten selected orientations of the radius vector as a test for isotropy: typical contours of these spatial correlations appear in figure 3.3. As a result correlation functions were further averaged around circles, since the field appears sufficiently isotropic. From these heavily averaged estimates, integral scale, microscale and zero crossing were obtained for each run. The results for forced and decaying turbulence are displayed in tables 3-4 and 3-5 respectively.

Before inferring any conclusions from those, the conservation laws for total energy and enstrophy in the basin shall be considered. The derivation of the vorticity equation given earlier does not hold in the limit of no topography ($\alpha \rightarrow 0$). However, the quasigeostrophic vorticity equation on an f plane can be found by applying the same general

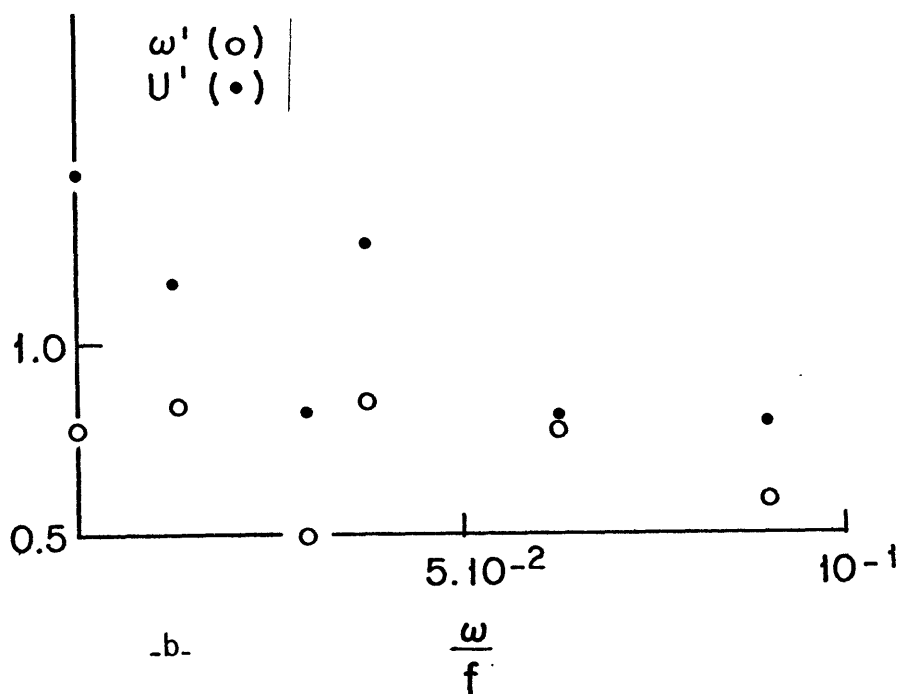
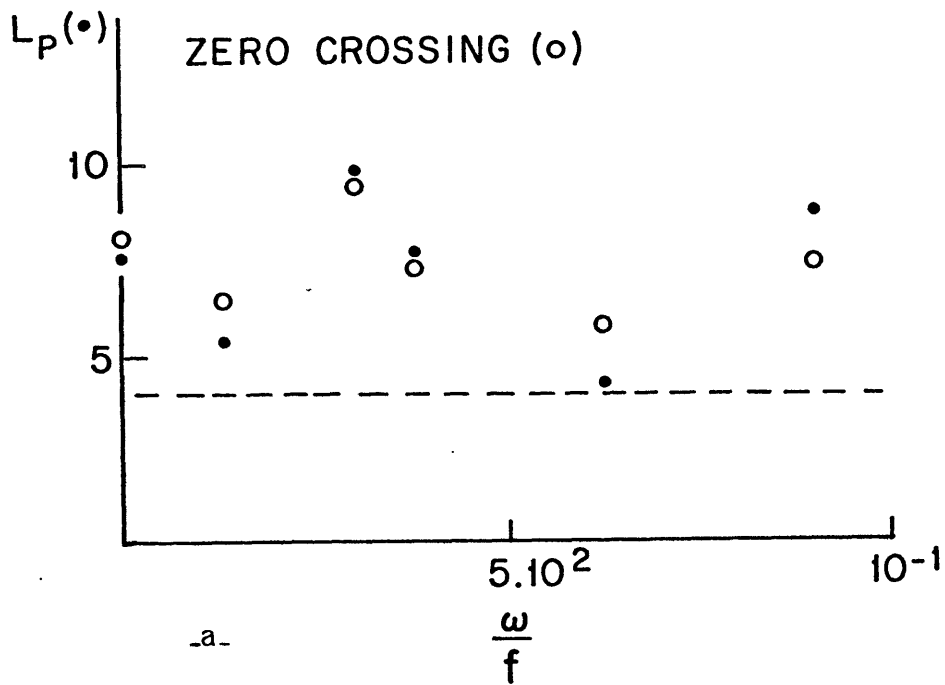


3-3 Contours of the transverse correlation function.

TABLE 3-4

Summary of parameters and basic statistics of forced 2D turbulence on an f plane (CGS units)

$\Omega(\text{rad/s})$	3.2	5.23	5.23	4.33	2.32	5.14
$\omega(\text{rad/s})$	0.4	0.4	0.14	0.78	0.14	0
$u' = (\overline{u^2})^{1/2}$	0.78	1.27	1.16	0.8	0.82	1.43
$L_p = \int_0^L f(r) dr$	4.31	7.78	5.36	8.91	9.75	7.56
Zero crossing for $g(r)$	5.96	7.2	6.56	7.37	9.7	8.0
λ_p	2.84	4.2	3.9	3.71	4.68	5.29
λ_n	2.24	2.95	3.0	2.9	3.02	3.86
λ_p/λ_n	1.27	1.42	1.29	1.27	1.55	1.37
$\omega' = (\overline{\omega^2})^{1/2}$	0.78	0.85	0.84	0.6	0.49	0.77
$\frac{u' L_p}{\nu}$	338	988	620	712	800	1080
$\frac{u'}{fL_p}$	2.8×10^{-2}	1.5×10^{-2}	2×10^{-2}	10^{-2}	1.8×10^{-2}	1.84×10^{-2}
$\frac{\omega}{2\Omega}$	6.25×10^{-2}	3.8×10^{-2}	1.3×10^{-2}	9×10^{-2}	3×10^{-2}	0
$\frac{2\pi W}{\omega H}$	8.4×10^{-2}	8.4×10^{-2}	2.4×10^{-1}	4.3×10^{-2}	2.4×10^{-1}	∞
$\frac{R}{\nu} \left(\frac{u'}{\omega}\right)^2$	2.6	7.4	6.3	5.3	5.9	11.3



3-6 Variations of the eddy scales and kinetic energy with ω/f in steadily forced 2D turbulence on an f-plane:

- (a) Integral scale and zero-crossing
- (b) Kinetic energy and enstrophy.

procedure using $\frac{\omega}{f}$ as the small parameter instead of the bottom slope, ω being the forcing frequency. By so doing, the 3 dimensional inertial wave modes are filtered out. Because of the cascade of vorticity to smaller scales, lateral friction cannot be neglected and it is included here in order to dissipate enstrophy at the very small scales.

The vorticity equation now reads

$$(1) \quad \frac{\partial \nabla^2 \psi}{\partial t} + J(\psi, \nabla^2 \psi) = -R \nabla^2 \psi - \frac{f}{H} w + \nu \nabla^4 \psi, \quad \text{with } R = 2E^{-\frac{1}{2}} \Omega^{-1}.$$

Multiplying (1) by ψ and integrating spatially over the basin:

$$(2) \quad \left(\frac{\partial}{\partial t} + 2R \right) \frac{\overline{|\nabla \psi|^2}}{2} = \frac{f}{H} \overline{w\psi} - \nu \overline{|\nabla^2 \psi|^2} \quad \text{where } (\overline{\quad}) = \iint_D (\quad) dS$$

Multiplying (1) by $\nabla^2 \psi$ and integrating yields further:

$$(3) \quad \left(\frac{\partial}{\partial t} + 2R \right) \frac{\overline{|\nabla^2 \psi|^2}}{2} = -\frac{f}{H} \overline{w \nabla^2 \psi} - \nu \overline{|\nabla(\nabla^2 \psi)|^2}.$$

With these two powerful conservation laws at hand, the experiments can be considered in more detail; first the steadily forced case shall be investigated.

The results in 3-4 indicate that the experiments have rather high Reynolds number compared to their numerical analogs. Estimates of rms velocity and vorticity indicate that a typical ratio of Ekman friction to lateral friction $\frac{R}{\nu} \left(\frac{u}{\omega} \right)^2$ is about 5, which says that Ekman friction is a little more efficient than lateral friction in damping the bulk of the kinetic energy. In figure 3.6 (b) the rms velocity decreases with $\frac{\omega}{f}$ as is consistent with a balance between the first and fourth terms in

equation (1). On the other hand the rms vorticity seems rather less sensitive to that parameter, perhaps because of a sampling problem in the microscale calculations, as indicated by low values of λ_p/λ_n compared to the predicted $\sqrt{3}$ for 2D isotropic turbulence. Figure 3-6 (a) shows that both the Eulerian integral scale and the zero crossing of the transverse correlation function are significantly larger than the forcing scale. These estimates for the eddy scale appeared to be smaller by a factor of 2 than the largest visual eddy diameter.

Lilly (1969, 1972), trying to test Kraichnan's prediction concerning the existence of inertial ranges, observed the same large scale tendency for forced 2D numerical turbulence. A proof of why this should be true will now be presented, (No such proofs seem to have yet appeared in the literature.) For simplicity, assume the energy spectrum to be continuous rather than discrete as the presence of solid boundaries would require: this does not affect the general validity of the derivation.

Let $E(k) dk$ be the contribution to $\frac{|\nabla\psi|^2}{2}$ from the wavenumber band $k, k + dk$. In statistically steady turbulence, the zeroth, first and second moment of the energy spectrum are steady.

$$(4) \text{ Identifying } \frac{|\nabla\psi|^2}{2} = \int_0^{\infty} E(k) dk, \quad \frac{|\nabla^2\psi|^2}{2} = \int_0^{\infty} k^2 E dk \text{ etc... and}$$

defining the energy containing scales as $\langle k \rangle = \frac{\int_0^{\infty} k E dk}{\int_0^{\infty} E dk}$, we consider the

steady state forms of (2) and (3) and subtract $\langle k \rangle^2$ times equation (2) from (3) after rearranging terms resulting in:

$$(5) \quad 2\nu \frac{[\overline{k^2} \cdot (\overline{k})^2 - (\overline{k^0})^2 \overline{k^4}]}{(\overline{k^0})^2} + 2R \frac{[(\overline{k})^2 - \overline{k^0} \overline{k^2}]}{\overline{k^0}} = \frac{f}{H} (\langle k \rangle^2 \overline{w\psi} + \overline{w\nabla^2\psi})$$

with the convention that $\overline{k^n} = \int_0^\infty k^n E(k) dk$. To estimate the sign of the left handside of (5) a convenient form of Schwartz's inequality may be applied.

If $n(x)$ and $e(x)$ are two integrable functions on the interval $[a, b]$, we have:

$$\left| \int_a^b h \cdot e dx \right|^2 \leq \int_a^b h^2 dx \int_a^b e^2 dx.$$

This applied to the lateral friction term in (5) yields successively:

$$\overline{k^2} \cdot (\overline{k})^2 \leq (\overline{k^2})^2 \cdot \overline{k^0} \leq (\overline{k^0})^2 \cdot \overline{k^4}.$$

Therefore the first term is negative. The second term related to the effect of Ekman friction can be evaluated in the same way:

$$(\overline{k})^2 \leq \overline{k^0} \cdot \overline{k^2}.$$

The second term is also negative and it can be concluded that:

$$(6) \quad \langle k \rangle^2 \overline{w\psi} + \overline{w\nabla^2\psi} \leq 0.$$

If the forcing wavenumber spectrum is strongly peaked at the wavenumber k_F , it appears that: $k_F^2 = -\overline{\psi\nabla^2 w} / \overline{\psi w}$.

For more general forcing distributions, the above expression could be taken as a definition of the forcing scale. After noticing that $\overline{w\nabla^2\psi}$ is equal to $\overline{\psi\nabla^2 w}$, substituting the forcing scale in (6) gives:

$$(7) \quad (\langle k \rangle^2 - k_F^2) \overline{\psi w} \leq 0.$$

$\overline{\psi w}$ is the generation term for the mean kinetic energy, equal in the steady state to $2R \cdot \overline{k^0} + 2\nu \cdot \overline{k^2}$, i.e., a positive definite term. Expression (7) says that the energy containing scale must be greater than the forcing scale. It may be reasonably expected that this spectral

definition of the energy containing scale does not preclude application of the above result to the experiments in which other definitions of the eddy scales have been used.

The more extensively studied case of freely decaying turbulence may now be considered. An inspection of table 3.5 shows that in the three runs examined, the length scale estimates grow in the decay state, a well known result also found in numerical studies. The Eulerian correlations in both initial and final states appear for comparisons in figure 3-7.

The reason for this spectral tendency can be found rigorously from the conservation laws of energy and enstrophy, Fjortoft (1953), Batchelor (1953). The nonlinear interactions are willing to disperse energy in Fourier space, but the constraint of total energy and enstrophy conservation forces the center of gravity of the spectrum to larger scale, while at the same time, the fourth moment of the spectrum increases as the vorticity contours get convoluted just as do passive dye lines in the fluid.

Rhines (1975) has given values for the cascade rates of such spin down experiments which are independent of the Reynolds number as to be expected from Batchelor's similarity solution (1969). Rhines finds: $\frac{d \langle k \rangle^{-1}}{dt} = 3.10^{-2} U_{rms}$. To apply this to the experiments with a non negligible bottom friction and where length scales other than $\langle k \rangle^{-1}$ are estimated, it is transformed into:

$$\frac{d L_p}{dt} = C \cdot U_{rms} e^{-Rt}$$

where L_p is the integral scale. By integrating this equation between initial and final state, one may compute values of C as:

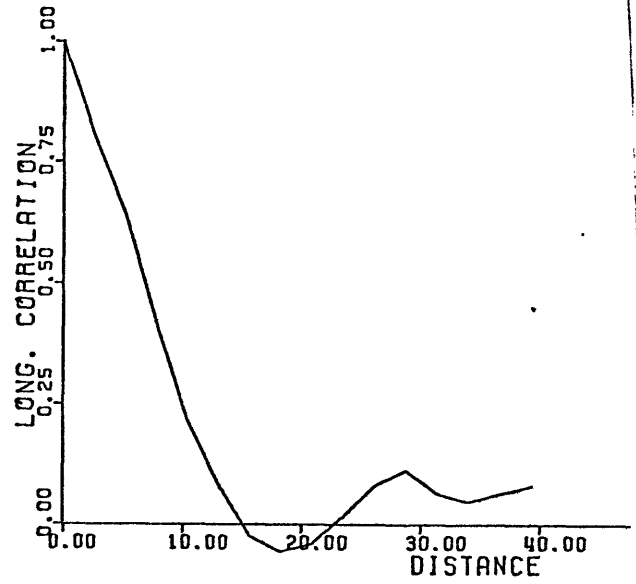
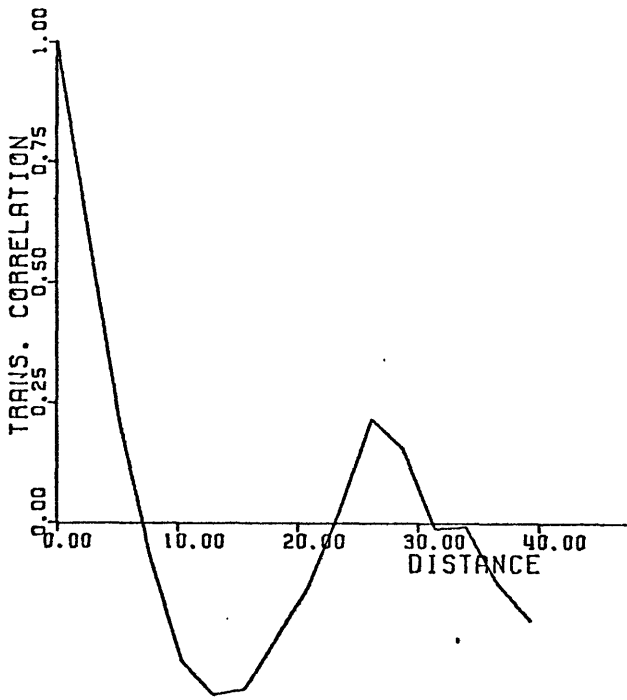
TABLE 3-5

Initial and final states of decaying 2D turbulence on an f-plane

	Run 1		Run 2		Run 3	
	Initial State t = 0	Final State t = 77s	Initial State t = 0	Final State t = 56s	Initial State t = 0	Final State t = 77s
Ω	3.2		5.23		2.32	
ω	0.4		0.4		0.14	
u'	0.78	0.183	1.27	0.173	0.82	0.2
L_p	4.31	5.61	7.78	12.7	9.75	13.5
Zero crossing for g(r)	5.96	9.1	7.2	7.14	9.7	10.4
λ_p	2.84	3.56	4.2	4.27	4.68	5.0
λ_n	2.24	2.7	2.95	3.52	3.0	4.4
ω'	0.78	0.145	0.85	0.11	0.49	0.11
$\frac{u' L_p}{\nu}$	338		988		800	
$\frac{u'}{fL_p}$	2.8×10^{-2}		1.5×10^{-2}		1.8×10^{-2}	

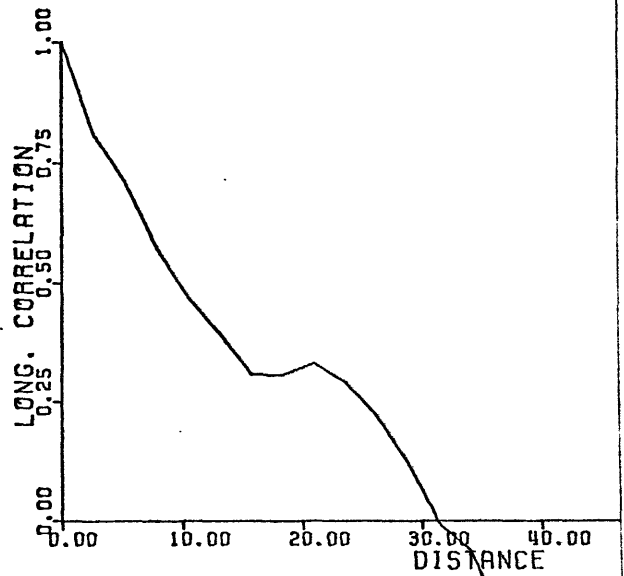
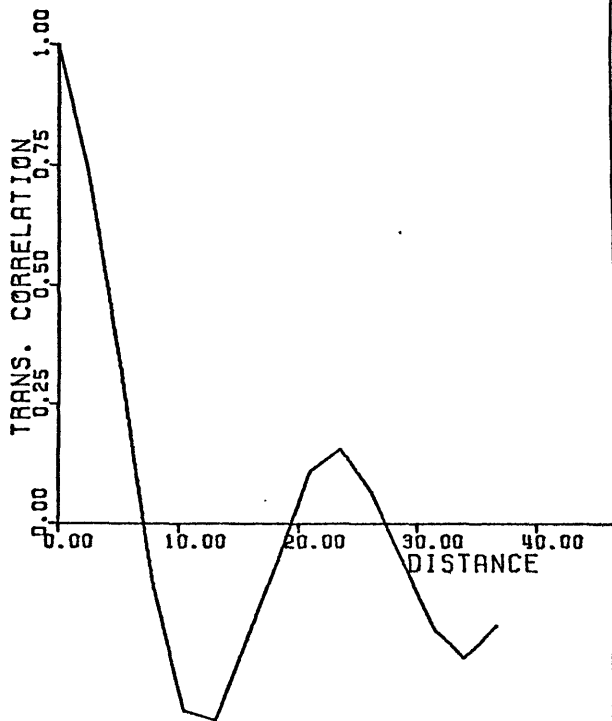
-a-

-b-



-c-

-d-



3-7 Correlation coefficient in f-plane 2D turbulence:

- (a) steady state transverse correlation .
- (b) steady state longitudinal correlation
- (c) decaying state transverse correlation
- (d) decaying state longitudinal correlation

$$C = \frac{L_p(t) - L_p(t_0)}{[U(t_0) - U(t)](t - t_0)} \cdot \text{Log} \frac{U(t_0)}{U(t)}$$

where t_0 is the initial state.

	RUN 1	RUN 2	RUN 3
C	4.1×10^{-2}	16×10^{-2}	11×10^{-2}
R	1.8×10^{-2}	3.6×10^{-2}	1.8×10^{-2}
$R_e = \frac{UL_p}{\nu}$	338	988	800

If one makes the rough order of magnitude correspondence between $\frac{\langle k \rangle^{-1}}{\pi}$ and L_p , the value of C from lower Reynolds number numerical studies comes out to be 9.4×10^{-2} , in reasonable agreement with the above experimental values. Typical relative errors on the above values of C are about 20%.

The large scale tendencies for both forced and decaying turbulence as observed and explained theoretically in this section is a common connecting link throughout this study. It reveals itself in many peculiar ways, sometimes identified as manifestations of negative viscosity phenomena, so unfamiliar in the three dimensional turbulent world.

II. Two dimensional turbulence on a polar β plane

Although the exploration of pure two dimensional turbulence began almost a generation ago, it is only very recently that the ways of thinking and methods used in turbulence have started to be applied to more geophysically relevant situations. Work by P. Rhines (1975) who included the presence of the β effect in a turbulent numerical model with periodic boundary conditions, is very relevant here. A conspicuous development of the flow field was observed in these spin down experiments. Unforced eddies initially at small scales, coalesce in much the same way as described in the preceding section, until energy containing scale reaches the level at which Rossby waves can propagate, thus effectively braking the cascade and introducing anisotropy in the velocity field. The end state of the cascade is a banded structure of quasisteady zonal currents. In the meantime the continuous deformation of potential vorticity contours caused by mixing is severely reduced as fluid particles start feeling the beta restoring force.

Along the same lines, Bretherton and Haidvogel (1976) considered the decay of a pack of eddies above rough topography in a closed basin and found that in the end state the currents flowed mainly along the large-scale topography, anticyclonically around bumps. They then hypothesized that such a state could be one of minimum potential enstrophy for a given energy level, because the small scale enstrophy cascade allowed lateral or higher order computer friction to damp enstrophy faster than energy. Both these numerical experiments were carried out in geometries with closed geostrophic f/H contours.

The laboratory experiments to be described below make use of a geophysically analogous geometry and are meant to provide real fluid



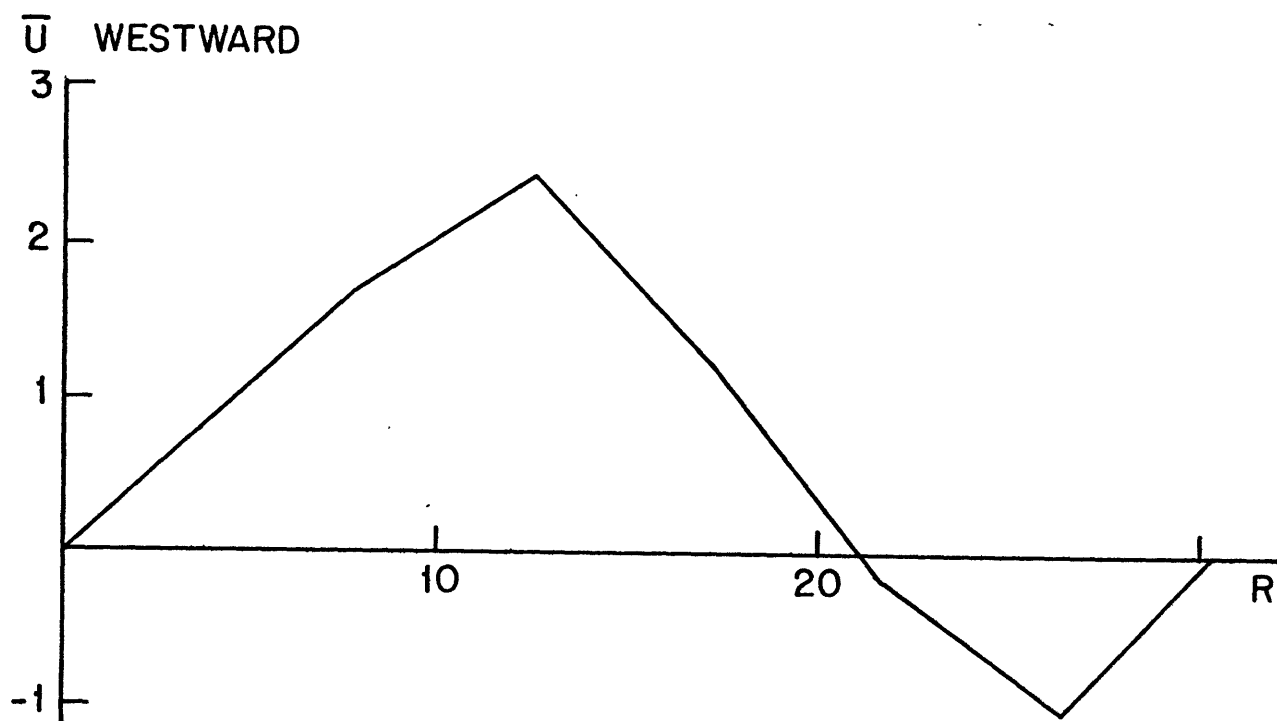
3-8 Turbulent flow on a polar β -plane. Experimental parameter values are $\Omega = 3.92$ rad/s, $\omega = 0.4$ rad/s, $H = 14.5$ cm, $w = 0.12$ cm/s

(a) Transient state

analogous of the above numerical free problems. The container, centered on the axis of the rotating table, is allowed to spin with its free surface developing a paraboloid of revolution. This models either an isolated topographic bump in an f plane ocean or a polar basin on a rotating spherical cap with flat bottom. The latter interpretation and associated vocabulary will be used here. The shallow center is identified as the north pole and beta increases linearly radially toward the southern boundary. The time-periodic forcing pattern is identical with the one used in Section I.

Applying the driving abruptly, small scale eddies are first generated. After an inertial time scale or so, they have grown remarkably large, while at the same time a strong westward mean flow has developed around the north pole. The statistically steady state consists of a prominent westward current with an associated belt of cyclones along the southern boundary. The transient and statistically steady flows are shown on figure 3-8. The mean profile of the steady zonal current is plotted on figure 3-9 for a typical run. It was obtained by zonally averaging east-west velocities from streak photographs. The latitudinal sampling interval was 3 cm and about 20 uniformly spaced velocity measurements were taken over each latitude circle. The meridionally integrated angular momentum contained in the westward jet is about $-3800 \text{ cm}^4/\text{s}$ while it is $3200 \text{ cm}^4/\text{s}$ in the eastward return flow: the total angular momentum balance is thus achieved in this run to within 20% indicating that the forcing puts negligible amounts of direct "torque" in the fluid.

After that brief presentation of the results, the rest of this section is devoted to developing an understanding of the observed mean flow generation processes and tendencies to large scale.



3-9 The zonally averaged steady mean flow.

A. Spectral evolution of free and forced eddies

With the free surface condition defined as:

$$z = \frac{\Omega^2 r^2}{2g}$$

the appropriate vorticity equation from Part I is:

$$(8) \quad \frac{\partial}{\partial t} (\nabla^2 \psi - \frac{\psi}{\lambda^2}) + J(\psi, \nabla^2 \psi) + \frac{f}{4\lambda^2} \frac{\partial \psi}{\partial \theta} = -R \nabla^2 \psi + \nu \nabla^4 \psi - \frac{f}{H} w$$

where $\lambda = \frac{(gH)^{\frac{1}{2}}}{f}$ is the Rossby radius of deformation.

If the scale of the motion is smaller than λ , then the second term in (8), which represents introduction of vorticity through free surface deformations, can be neglected and the surface is dynamically rigid. Since tendencies toward larger scales for the eddies are found in the experiments, caution dictates retention of those terms, noting that typical values for the experimental Rossby radius are about four times smaller than the diameter of the container.

Conservation laws (integrated over the basin) give

$$(9) \quad \frac{\partial}{\partial t} \left(\frac{|\nabla \psi|^2}{2} + \frac{\psi^2}{2\lambda^2} \right) = -2R \frac{|\nabla \psi|^2}{2} - \nu |\nabla^2 \psi|^2 + \frac{f}{H} \overline{w\psi}$$

and then the total enstrophy:

$$(10) \quad \frac{\partial}{\partial t} \left(\frac{|\nabla^2 \psi|^2}{2} + \frac{1}{\lambda^2} \frac{|\nabla \psi|^2}{2} \right) = -2R \frac{|\nabla^2 \psi|^2}{2} - \nu |\nabla(\nabla^2 \psi)|^2 - \frac{f}{H} \overline{w \nabla^2 \psi}$$

It is worth noting that the topographic - Beta term does not introduce any novel feature in the conservation laws, which is a general result for geometries with closed geostrophic contours. Furthermore the second term in (9) represents the potential energy stored in the free surface.

The spectral evolution of a set of free inviscid eddies is investigated first, to see if the free surface terms might reverse the now classical tendencies:

Let $C(k)$ and $P(k)$ be the kinetic and potential energy spectrum respectively. From their definitions it is found that:

$$P(k) = (k\lambda)^{-2} C(k).$$

The total energy spectrum $E(k)$ is the sum of the kinetic and potential energy spectrum. Omitting the right hand sides of (9) and (10), one derives:

$$(11) \quad \frac{\partial}{\partial t} \overline{k^0} = 0$$

$$(12) \quad \frac{\partial}{\partial t} \overline{k^2} = 0$$

where as usual

$$\overline{k^n} = \int_0^{\infty} k^n E(k) dk.$$

Expressions (11) and (12) indicate that "total" energy and enstrophy are also invariants of the motion. The requirement that the breadth of the spectrum increases in time due to non-linear interactions shows, as earlier, that the "total" energy containing scale $\langle k \rangle^{-1}$ increases in time. Because the kinetic and potential energy spectra are, respectively, the high and low pass filtered versions of the total energy spectrum, both will tend to larger scale. The kinetic energy of eddies initially at scales smaller than the Rossby radius of deformation will move its center of mass toward the Rossby radius while at the same time it is converted into potential energy. At scales larger than the Rossby radius, the main transfer of energy is a red cascade of potential energy. Although either form of energy may be present and conversions from one to

the other are possible, the flow must migrate to larger scales as its spectral contents become richer. There are no processes like baroclinic instability in a stratified fluid that can generate small scale transient motions from the potential energy stored in the free surface.

The large scale circulation of steadily forced eddies is even simpler to prove. The left hand sides of expressions (9) and (10) vanish, reducing them to those considered earlier on an f-plane. Thus, the derivation given there holds here as well. Both of these results are consistent with our earlier observations of eddies on a Beta plane.

An investigation of the generation of Eulerian mean flows on a beta plane can now be undertaken. Use will be made of a simple, steady, linear model of forced Rossby waves in which the second order mean currents are calculated in detail.

B. Forced Rossby waves in an infinitely long channel

It is perhaps important to realize why attention is directed to simplified analytical models for an understanding of steadily forced flow. After Whitehead's (1975) observations that purely periodic forcing acting on a Beta plane led to strong Eulerian mean flows, westward in free regions and eastward in forced ones, Rhines (1977) demonstrated that such westward flows were the result of an irreversible meridional mixing of fluid parcels conserving their potential vorticity. At that time, explanation of the eastward flow over the forced regions originated from angular momentum considerations, assuming that the forcing put no torque on the fluid. In our experiments, in which the fluid is forced uniformly everywhere, it seemed very natural to seek an extension of Rhines' finite amplitude theory which would be valid over forced regions. The inherent difficulties of this problem are now briefly exposed.

The vorticity equation derived in Part I can be written on a constant, infinite Beta plane as:

$$(13) \left(\frac{D}{Dt} + R \right) q = R\beta y + F,$$

$\frac{D}{Dt}$ being the material derivative, β being $\frac{f}{H} \frac{\partial H}{\partial y}$, F a possible forcing function, and $q = \zeta + \beta y$ the potential vorticity. The zonally averaged complete x-momentum equation may be manipulated to yield:

$$(14) \left(\frac{\partial}{\partial t} + R \right) \bar{u} = \bar{q}v$$

where it has been assumed that the forcing does not introduce any direct mean force on the fluid.

To obtain a simple expression for the meridional transport of potential vorticity one may construct the time integral of (13) following a fluid parcel which had potential vorticity q_0 at latitude and time $t = 0$:

$$q = q_0 e^{-Rt} + R\beta \int_0^t y(t') e^{R(t'-t)} dt' + \int_0^t F(x(t'), y(t'), t') e^{R(t'-t)} dt'$$

Zonally averaging the transport qv along a "fixed" latitude line yields:

$$(15) \bar{q}v = \bar{q}_0 v e^{-Rt} - R\beta \int_0^t \bar{k}(z) e^{-Rt} dt + \int_0^t \overline{v(y,t) F(y(t'), x(t'), t')} e^{R(t'-t)} dt'$$

where the diffusivity is:

$$\bar{k}(t) = \frac{1}{2} \frac{D(y-Y_0)^2}{Dt} = \int_0^t R(\tau) d\tau$$

$R(\tau) = \overline{v(t)v(t-\tau)}$ being the Lagrangian autocorrelation function.

The first term in (15) represents the viscous spin down of the initial potential vorticity transport. It is the important term where one considers initial value problems (These will be looked into in Part III of this study.)

The second term which remains in the steady balance, is the planetary vorticity mixing term and the last one is the direct forcing contribution to the potential vorticity transport, when fluid particles happen to alter their potential vorticity while wandering over forced regions. Using simple kinematical arguments, Taylor (1921) constructed the short and long time behavior of the diffusivity $\bar{k}(t)$. Combined with the intuition available to determine the sign of $\bar{k}(t)$ (as emphasized by Rhines (1977)), one is in a position to make a reasonable estimate of the second term. On the other hand, no simple ideas were found to illuminate the behavior of the Lagrangian velocity-forcing correlation involved in the last term. In the steady state, the potential vorticity transport is balanced by the frictional force proportional to the mean zonal flow and this prevents us from making any predictions about the zonal flow, when the fluid is forced uniformly everywhere, as in the experiments. Therefore, it was necessary to look for a model whose dynamics could be solved explicitly. The relation (15) could then be calculated and hopefully understood.

The model used is linear, steadily forced and viscous. Its geometry consists of an infinitely long zonal channel on a Beta-plane, preserving the essential feature of the experiments, namely the existence of closed geostrophic contours. The relevant "linear" vorticity equation is simply:

$$(16) \quad \frac{\partial \nabla^2 \psi}{\partial t} + \beta \psi_x = -R \nabla^2 \psi + F(x, y, t)$$

where bottom friction is the dissipative mechanism and $F(x, y, t)$ represents a forcing function. The object is to solve (16) subject to the boundary conditions that $\psi = 0$ at $y = 0$, and a , the sides of the

channel. An alternative version to (14) is:

$$(17) \quad \left(\frac{\partial}{\partial t} + R\right) \bar{u} = - \frac{\partial}{\partial Y} \overline{uv}.$$

The term on the right hand side is the divergence of the Reynolds stress.

Knowing ψ , the steady mean flow, if any, will be obtained from:

$$(18) \quad R \bar{u} = \frac{\partial}{\partial Y} \overline{\psi_x \psi_y}.$$

Scaling time by $(\beta a)^{-1}$, length by a , ψ by $\frac{aF}{\beta}$ the following non-dimensional vorticity equation is obtained:

$$(19) \quad \nabla^2 \psi_t + \psi_x = - \epsilon \nabla^2 \psi + G(x, y, t) \quad \text{where} \quad \epsilon = \frac{R}{\beta a}.$$

Let us recall that interest is somewhat arbitrarily restricted to the steady forced solution of equation (19), therefore we look solely at that part of the solution remaining after the transients generated by the switch-on have been damped out by friction in a 'time of order ϵ^{-1} .

The free inviscid normal modes are:

$$\psi_n = \sin n\pi y e^{i(kx + \omega_n t)}$$

with ω_n satisfying the dispersion relation:

$$\omega_n = \frac{k}{k^2 + n^2 \pi^2}.$$

Assume at first the obvious forcing function

$G(x,y,t) = e^{i(kx+\omega t)} \sin n\pi y$, whose envelope has the normal mode shape in the meridional direction. The solution of (19) satisfying the boundary conditions is:

$$\psi(x,y,t) = \mathcal{R} \left\{ \frac{(\omega - \omega_n + i\varepsilon) e^{i(kx+\omega t + \frac{\pi}{2})} \sin n\pi y}{(k^2 + n^2\pi^2) ((\omega - \omega_n)^2 + \varepsilon^2)} \right\}$$

As the vorticity is constant over a streamline, the above solution satisfies the complete non linear vorticity equation, the non linear terms vanishing identically. As a result the Reynolds stresses also vanish and no mean flow can be generated. At this point, it was necessary to consider a forcing distribution richer in meridional scales, hoping that interaction of different scales would generate mean flows. For this purpose and with experimental comparisons in mind, a constant forcing across the channel was chosen. Hence

$$G(x,y,t) = e^{i(kx + \omega t)} L(y) \quad \text{with } L(y) = 1 \text{ for } 0 < y < 1.$$

The solution to (19) is found by expanding the unknown ψ and the forcing $L(y)$ in terms of the inviscid normal modes. The Fourier coefficients of the forcing are $L_{2p+1} = \frac{4}{\pi(2p+1)}$, $L_{2p} = 0$ and the result is:

$$(20) \quad \psi(x,y,t) = \left\{ \frac{4e^{i(kx+\omega t + \frac{\pi}{2})}}{\pi} \sum_p \frac{(\omega - \omega_{2p+1} + i\varepsilon)}{[(\omega_{2p+1} - \omega)^2 + \varepsilon^2]} \frac{\sin(2p+1)\pi y}{(2p+1)(k^2 + (2p+1)^2\pi^2)} \right\}$$

The coefficient of the Fourier series, shows the familiar amplitude and phase expressions found in resonance problems: the denominator

controls the amplification of a particular harmonic and the numerator expresses the phase difference between that particular harmonic and the forcing which is the crucial part of mean flow generation. Using the solution (20), the Reynolds stress divergence $-RS$ can be obtained and one finds:

$$(21) \quad RS = 8k\varepsilon \sum_{p,q} B_{2p+1} B_{2q+1} (2q+1)^2 (\omega_{2p+1} - \omega_{2q+1}) \sin(2p+1)\pi y \sin(2q+1)\pi y$$

$$\text{with } B_{2p+1} = [(k^2 + (2p+1)^2 \pi^2) (2p+1) (\omega_{2p+1} - \omega)^2 + \varepsilon^2]^{-1}.$$

The expression (21) shows again that self-interaction of harmonics does not contribute to the divergence. The double sum (21) will usually be evaluated numerically for different values of the three parameter k , ω and ε . Before proceeding, however, an alternative expression for the Reynolds stress divergence can be found as indicated earlier. It enables us to separate out the effects of the potential vorticity mixing of the forcing.

Equation (15), non dimensionalized, is used to calculate the diffusive term DF and the forcing term FT . Lagrangian path integrals occurring in (15) are calculated to first order in the wave steepness, consistent with the neglect of the non linear terms in (16). The results after some algebra are:

$$(22) \quad DF = \frac{-8 k^2 \varepsilon}{\pi^2 (\varepsilon^2 + \omega^2)} \sum_{pq} B_{2p+1} B_{2q+1} \sin(2p+1)\pi y \sin(2q+1)\pi y$$

$$[\varepsilon^2 + (\omega_{2p+1} - \omega_0)(\omega_{2q+1} - \omega_0)]$$

and

$$(23) \quad FT = \frac{8 k \epsilon}{\pi^2 (\epsilon^2 + \omega^2)} \sum_{pq} \frac{B_{2p+1}}{2q+1} \sin(2p+1)\pi y \sin(2q+1)\pi y \cdot \omega_{2p+1}$$

and one can check that $RS = DF + FT$ as given by (21), (22) and (23).

Another quantity of interest is the "Stokes drift" of the solution (20), and the related Lagrangian second order mean currents. Because the Eulerian velocity gradients are important, particle paths are not exactly closed. The net drift experienced by a passive tracer in the flow is simply the sum of the Eulerian mean currents RS and the Stokes drift SD . Using (20), one finds that:

$$(24) \quad SD = \frac{8k\epsilon}{\omega} \sum_{p,q} B_{2p+1} B_{2q+1} [(2p+1)^2 \sin(2p+1)\pi y \cdot \sin(2q+1)\pi y - \\ (2p+1)(2q+1) \cos(2p+1)\pi y \cos(2q+1)\pi y] \\ [\epsilon^2 + (\omega_{2p+1} - \omega)(\omega_{2q+1} - \omega)].$$

This bears a direct relation to the experiments in which the mean currents measured are in fact the Lagrangian ones. Dependence of the strength and structure of the mean flow upon the forcing parameters k , ω and ϵ may now be investigated. For convenience, when $\omega_{2p+1} < \omega < \omega_{2p-1}$, one defines:

$$\Delta\omega = \omega_{2p-1} - \omega_{2p+1} = 8\pi^2 \frac{pk}{[k^2 + (2p-1)^2\pi^2][k^2 + (2p+1)^2\pi^2]}$$

$\Delta\omega$ is the discrete equivalent to the north-south group velocity of inviscid Rossby waves in an infinite medium.

The viscous regime specified by a large value of ϵ/ω is described first. In this regime $\frac{\Delta\omega}{\epsilon}$ is also small and it indicates that

the resonance will be poor as waves do not feel the boundaries of the channel.

When the forcing scale is very large, the double Fourier series can be summed analytically with the following results:

$$RS = \frac{k^2}{48 \epsilon^3} (-5y^4 + 10y^3 - 6y^2 + y)$$

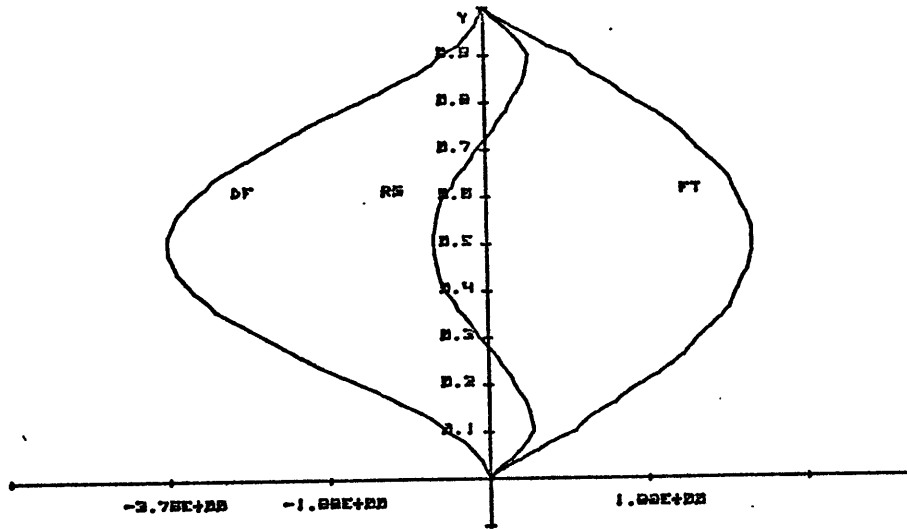
$$DF = -\frac{k^2}{8 \epsilon^3} (y - y^2)^2$$

$$FT = \frac{k^2}{24 \epsilon^3} (y^4/2 - y^3 + y/2)$$

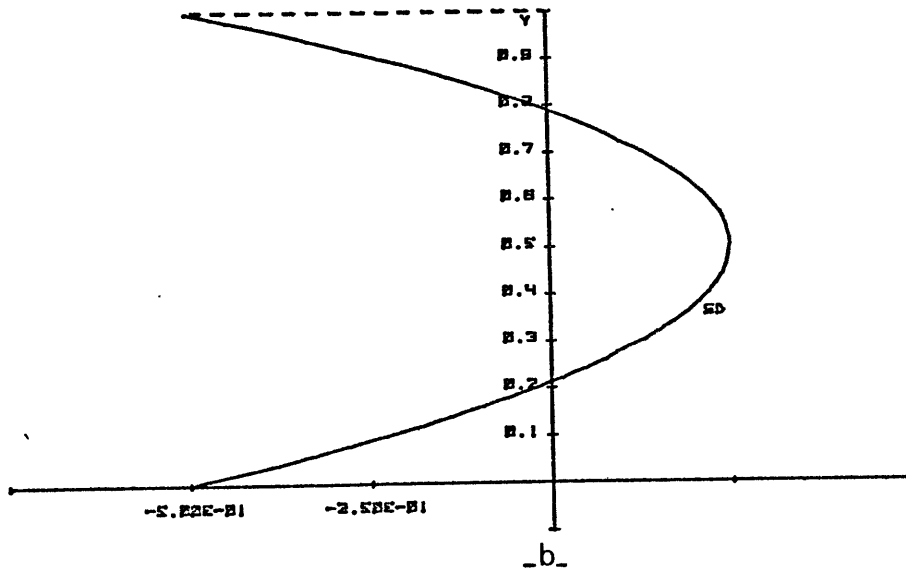
$$SD = \frac{k}{4 \epsilon \omega} (-3y^2 + 3y - \frac{1}{2}).$$

These expressions are plotted on figures 3-10(a) and (b). The structure of the mean current is westward in the interior and eastward near the boundaries. The diffusive term is always negative, small near the wall and large in the interior compared to the forcing term which is positive, large near the walls and smaller in mid channel. However the scale factors show that the Eulerian mean flow is very small compared to the Stokes drift which is eastward in the interior and westward near the walls. This indicates that the Lagrangian mean flow will swamp the mean Eulerian picture. In these runs, the friction coefficient is large and only a small Eulerian flow is needed to balance the Reynolds stress. On the other hand the Stokes drift, a purely kinematical effect, makes reference to friction only indirectly through the solution (20).

When the forcing scale is small, the Eulerian mean flow is insignificant throughout the channel. The diffusive and forcing terms are



a

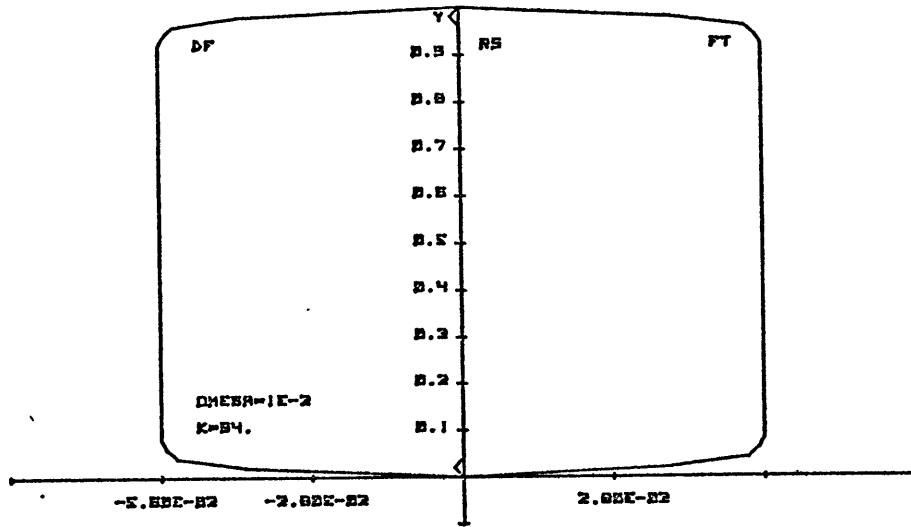


b

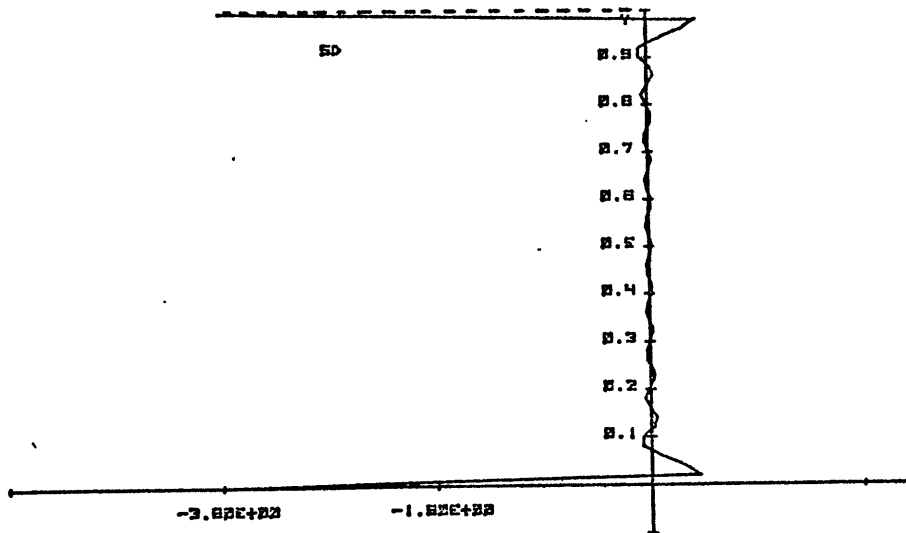
3-10 The viscous, long wavelength limit:

(a) The mean flow RS, the vorticity mixing term DF and the forcing term FT

(b) The Stokes drift SD.



-a-



-b-

3-11 The viscous, short wavelength limit:

(a) The mean flow RS , the diffusive term DF , and the forcing term FT

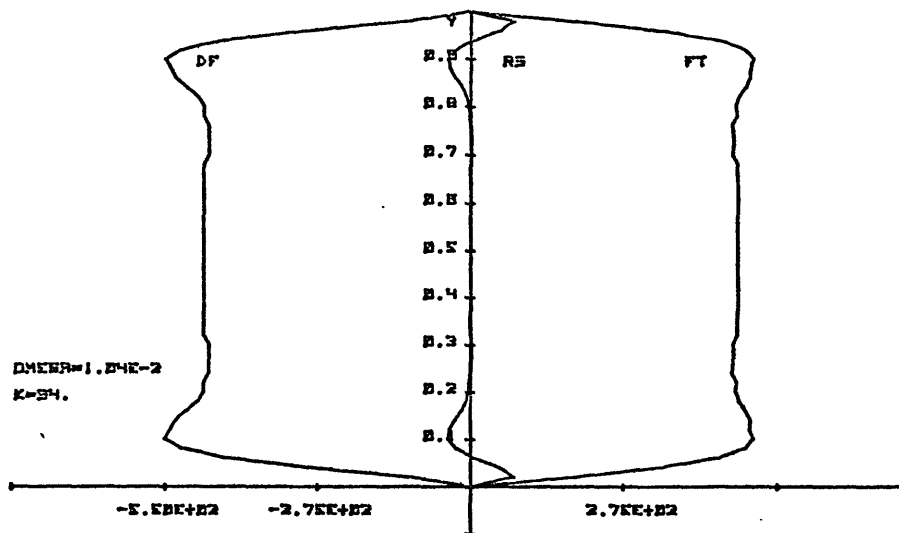
(b) The Stokes drift SD .

constant and balance each other while the much larger Stokes drift which vanishes in the interior, indicates Lagrangian flows to the east and then to the west when approaching the walls. Refer to figures 3-11 (a) and (b).

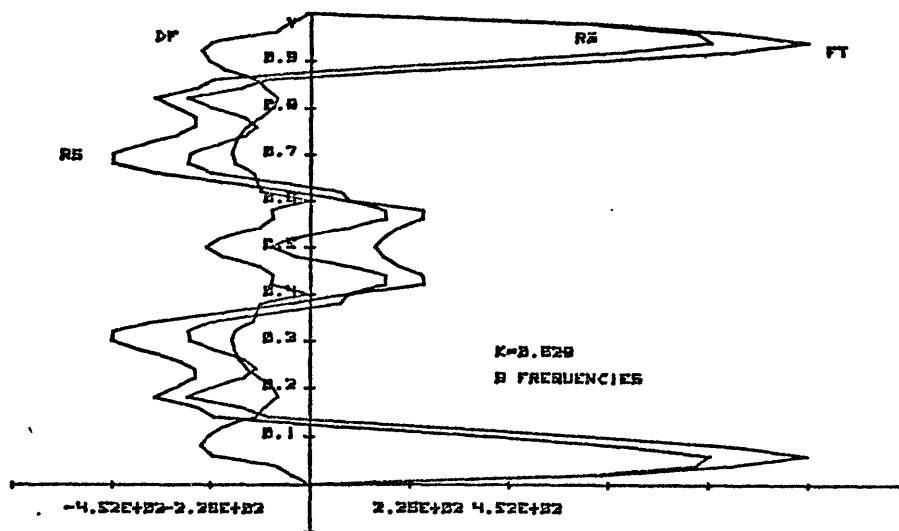
Let us examine now the more interesting inertial regime when ε/ω is small. The Stokes drift is now typically smaller than the Eulerian mean flow. Lagrangian mean flow will be a very good indicator of the Eulerian one.

When the meridional or zonal forcing scale is small enough, such that $\frac{\Delta\omega}{\omega}$ is smaller than ε/ω , then $\frac{\Delta\omega}{\varepsilon}$ is smaller than unity. Again the resonance will be poor as neighboring harmonics in (20) will have roughly the same amplitude and phase. The results shown in figure 3-12 indicate that the mean momentum is concentrated along the zonal boundaries, where it is westward in the interior and eastward close to the walls.

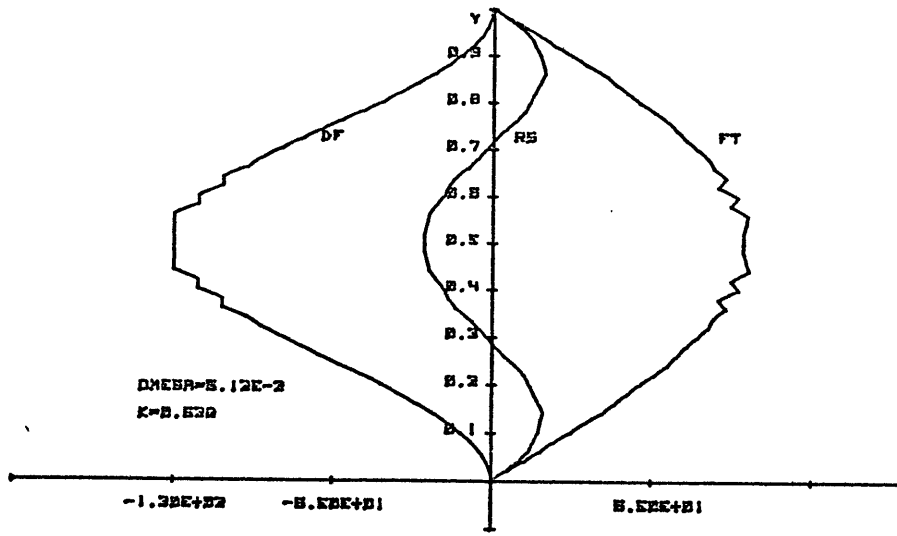
When the forcing scale is large enough such that $\frac{\Delta\omega}{\omega}$ is greater than $\frac{\varepsilon}{\omega}$, then $\frac{\Delta\omega}{\varepsilon}$ is larger than unity. When the forcing excites one of the inviscid normal frequencies, the amplitude of that coefficient of that particular mode in the solution (20) is magnified. It turns out that this particular resonant structure may also leave its signature in the mean current pattern, modifying the simple structure found up to now. When the forcing excitation is off resonance, then the amplitude of the mean flow drops sharply and its meridional structure is usually an hybrid of the two adjacent resonant modes. Note this behavior for the five runs presented in figure 3-13. In these cases the zonal forcing wavelength and the Q of the cavity $\frac{\omega}{\varepsilon}$ are held constant (both equal to 10), while the forcing frequency gradually decreases, thereby exciting smaller meridional scales. When ω falls below ω_5 , considerable fine structure appears and eastward jets may now be found in the interior.



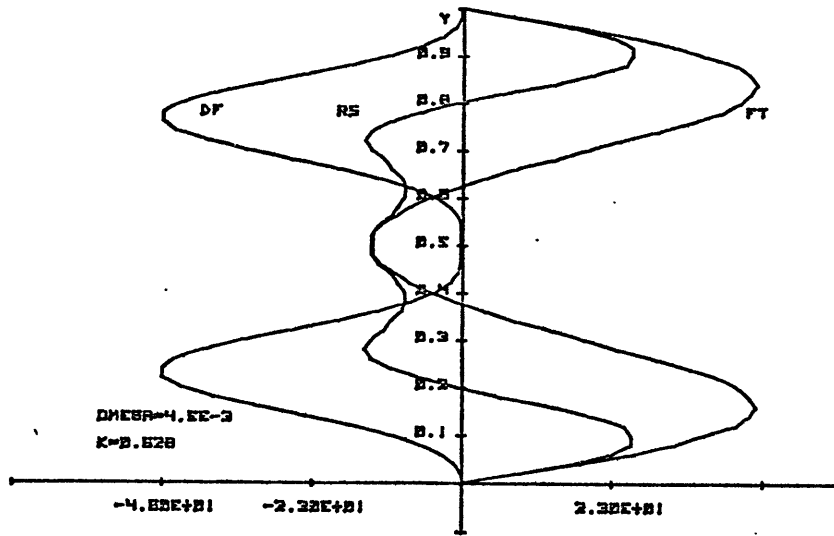
3-12 The inertial, short wavelength limit ($\epsilon/\omega = 0.1$).



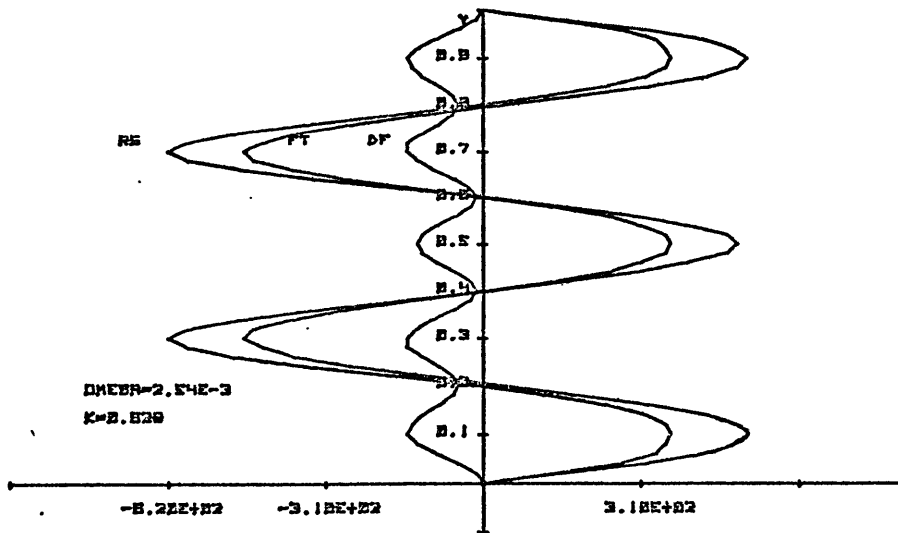
3-15 The mean flow response to a forcing frequency spectrum containing 9 discrete frequencies in the inertial regime.



-a-



-b-

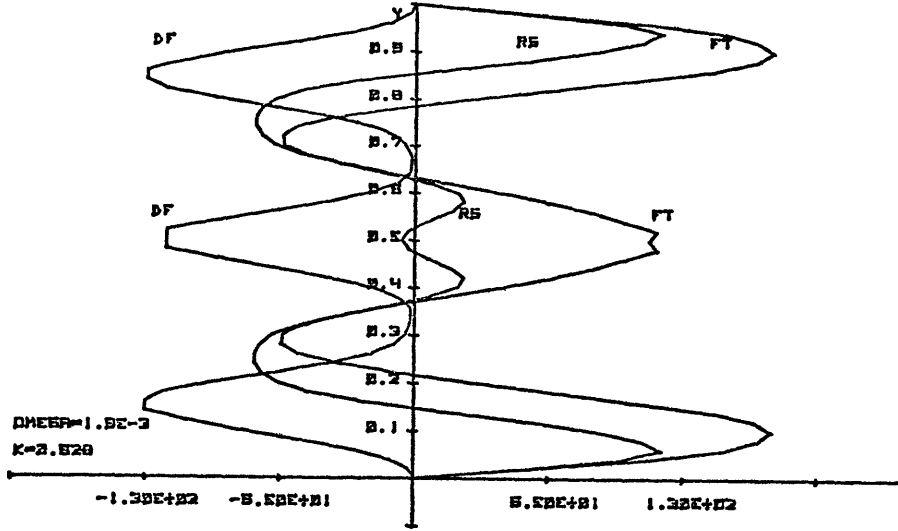


-c-

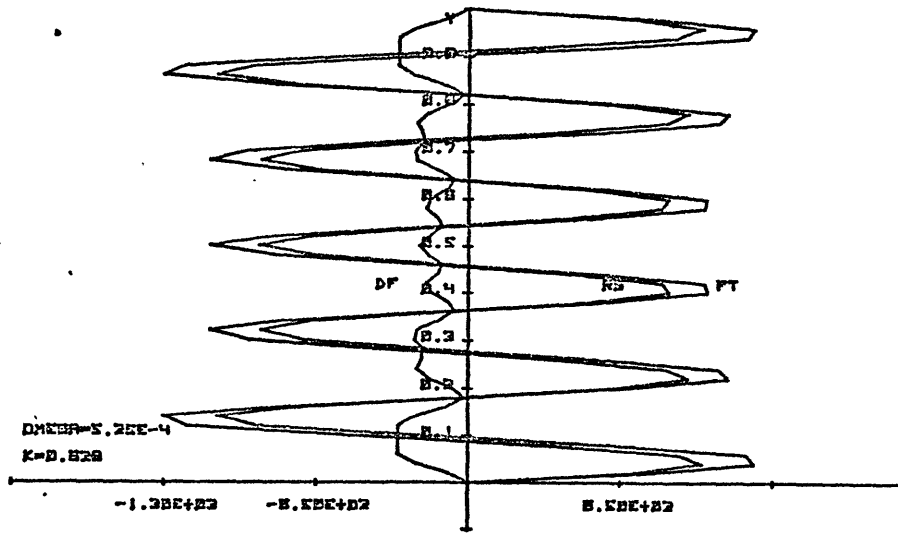
3-13 The inertial, long wavelength limit ($\epsilon/\omega = 0.1$, $k = 0.628$) for various frequencies

(a) $\omega = \omega_0$

(b) $\omega_3 < \omega < \omega_5$



-d-

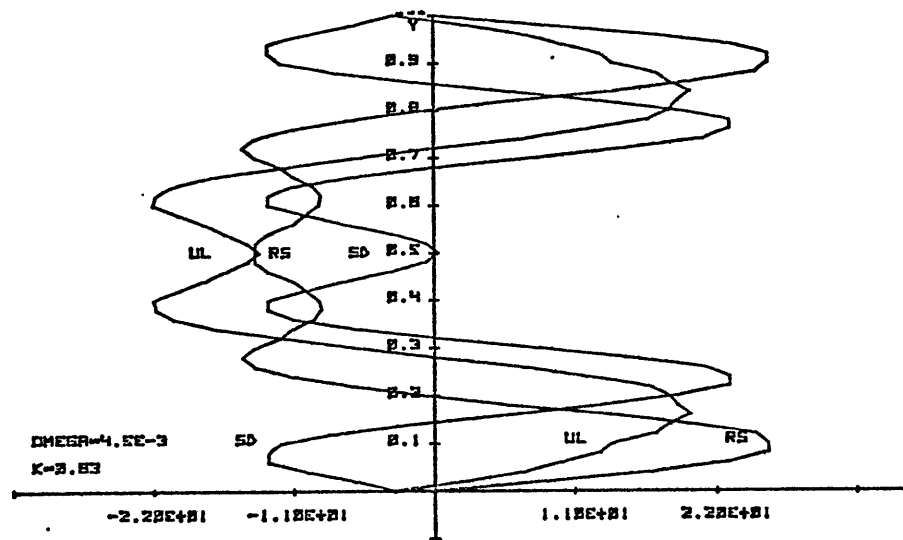


-e-

3-13 The inertial, long wavelength limit ($\epsilon/\omega = 0.1$, $k = 0.628$) for various frequencies

(d) $\omega_5 < \omega < \omega_7$

(e) $\omega = \omega_{11}$



- 3-14 The Eulerian and Lagrangian mean flows in the inertial long wavelength limit ($k = 0.628$, $\epsilon/\omega = 0.1$, $\omega_3 < \omega < \omega_5$); RS is the Eulerian mean flow, SD is the Stokes drift, UL is the Lagrangian mean flow.

Although the intricacy of the picture has increased a great deal, one may still find important internal consistencies in the structure, which aid in the development of a physical understanding. First, an eastward jet is always found at each zonal boundary. Second, the "interior" meridionally averaged mean momentum, is always westward since the total mean momentum is zero. Third, the diffusive term is negative everywhere. Its absolute value is small near the boundaries compared to the forcing terms which is positive in this region. On the other hand, the forcing term may be of any sign and amplitude in the interior.

For completeness we have also plotted in figure 3-14, the Eulerian mean flow, the Stokes drift and their sum for one of the above runs. It will be seen that the structure of the Lagrangian mean flow does not differ essentially from the rectified Eulerian mean flow.

When the bandwidth of the forcing wavenumber or frequency spectrum increases, these observations lead one to expect a sharpening of the eastward jets near the wall and a broadening of the region of westward momentum in the interior. Indeed, this was demonstrated in a numerical calculation designed to test it. With a constant friction parameter (3.7×10^{-5}) and zonal wavenumber (0.628) the individual responses to nine various forcing frequencies were computed and averaged. With a frequency range that was bounded by ω_5 and ω_{11} and a mean Q of about 15, the response to each individual frequency yielded considerable fine structure in the mean flows. The total response shown in figure 3-15, now reveals a much simplified pattern, with the smoothed interior flow almost everywhere westward and the sharpened eastward jets along the walls.

To summarize the results of the model in the inertial regime, one may say that subjected to a meridionally uniform forcing with varied

space and time scales, the fluid responds by building up a mean state in which the meridionally averaged correlation $\overline{\psi y}$ is systematically positive. $\overline{\psi}$ is the mean state stream function. As the forcing spectrum gets richer, the tendency for a simple broad westward interior flow with confined return flows on the boundary seem to develop.

In reference to the laboratory experiments, it is hoped that any doubts concerning the true inertial nature of the laboratory flows have vanished since the viscous regime of the model indicates opposite Lagrangian mean flows to the one observed. On the other hand, the inertial regime shows considerable qualitative agreement, the laboratory value of Q being about 10 for the lowest Rossby modes.

At this point it seem desirable to gain some physical understanding for the above mean flow structure. The following arguments are restricted to the more interesting inertial regime when the concept of group velocity may be used. Near each zonal boundary, with an energy source acting quite close to the boundary, the net wave energy flux must be inward since partial reflexion of energy occurs at the boundary. The meridional extent of that inward energy flux region will be larger as the north south group velocity increases while dissipation diminishes (i.e., the energy reflexion coefficient will increase). From the Rossby waves dispersion relation, one concludes immediately that a northward group velocity (respectively southward) is associated with streamline patterns tilted in the northwest-southeast direction (respectively northeast-southwest). This tilt of the wave troughs is just what is needed to generate eastward jets at each wall. This reasoning leads to the belief that the eastward jet region must increase when $\frac{\Delta\omega}{\epsilon}$ increases. (Remember that $\Delta\omega$ is a "discrete type" group velocity equivalent.) Consider

then the five runs shown in figure 3-13 carried out at constant k and ε/ω . In these experiments lower forcing frequencies and hence lower $\frac{\Delta\omega}{\varepsilon}$ make the eastward jets shrink to the sides of the channel.

Turning to an interpretation of the forcing and diffusive term in (13), one may note the following: In a wavelike steadily forced motion, one expects the meridional dispersion $\overline{(y - y_0)^2}$ to increase from zero to a small constant value. This makes the sign of the diffusive term in equation (13) unequivocally negative. Because this term is quadratic in the meridional velocity while the forcing term is linear (for small meridional displacements), one is led to expect that near the walls the eastward jets will be driven primarily by the positive forcing terms. On the contrary, in the interior, the diffusive term is responsible for driving the westward flow, while the forcing term may take any value and sign. We may only say that the total meridional average of the forcing term must be positive to counterbalance the effect of mixing of potential vorticity by the waves.

This quasilinear analysis has provided a reasonable comparison with the turbulent regime of the experiments. The meridional fine structure that appears in the model distribution of the mean flows for low driving frequencies must be considerably reduced for turbulent flows. Indeed it is known that large scale flow tendencies occur over such beta plane geometries. A limited quantity of information relevant to the turbulent experiments is available directly from the finite amplitude transport equation (15).

In the steady limit of (15), the mixing term is negative everywhere because in a homogeneously forced fluid the diffusivity \bar{k} is positive and vanishes at the boundaries. Since the total angular momentum is

conserved, one concludes that the meridional average of the forcing term in (15) is positive. As indicated earlier, the forcing term is greater than the mixing term near the southern boundary where v' vanishes. Consequently an eastward flow must be present near the wall. In the interior the mixing term is greater than the forcing term on the "average" and drives the return westward flow.

Although anticyclones gather in the north while cyclones are pushed far south (figure 3-9), one may show that the area-averaged $\overline{\zeta y}$ correlation vanishes assuming homogeneity of the forcing. Thus while the experiments and the model reveal a non-zero, positive $\overline{\psi y}$ correlation, no net vorticity partition is associated with it.

Considering the transient westward flow associated with the impulsive switch on of the turbulence, (figure 3-8), the present use of (15) is limited. It is only when the driving is independent of longitude that one may assert that the mixing term in (15) grows initially as t faster than the forcing term, inducing the retrograde flow in the interior where $\overline{v^2}$ is large. In the experiments, however, the forcing although statistically homogeneous is not longitude independent, and one encounters therefore the same difficulties as in the steady limit.

III. Two dimensional turbulence in the "sliced cylinder" model

The geometry examined in the preceding paragraph could be thought of as a model of the polar cap of a barotropic atmosphere. The present "sliced cylinder" was introduced first by Pedlosky and Greenspan (1967) to simulate accurately in the laboratory the large scale oceanic circulation. The geometry is one of a cylinder of revolution whose top surface has been tilted through an angle α to the horizontal. The geostrophic $\frac{f}{H}$ contours are now straight line running east-west and intersecting the walls. Intensive study of both the steady and time dependent response has been made by Beardsley (1969, 1975). The success of these experiments in reproducing both the Stommel and Munk's solution of the wind driven oceanic circulation, and in shedding light on the unsteady currents, led to the undertaking of turbulent experiments in which the focus is on the structure of the eddies themselves. In particular the eddies' ability to generate mean flows, as suggested by Pedlosky (1965)'s quasilinear analysis, needed to be evaluated and compared to our earlier experiments with closed geostrophic contours.

The forcing function used here is homogeneous on the bottom and again of the pseudo-random type. The forcing amplitude is meant to be large enough to generate turbulent eddies, while keeping the Rossby number $\frac{U}{fL}$ small (L being an eddy scale). The experiments were run for various values of effective beta, Coriolis parameter and forcing amplitude. Both the steadily forced stage and the decaying period were observed.

Throughout the runs the turbulent eddies behave in a similar way and can be described as follows: When the forcing is impulsively turned on, small scale eddies are generated. The subsequent scale evolution does not depart much from the initial configuration. However, spatial in-

homogeneity develops quickly. Larger eddy scales and less kinetic energy are found in the eastern basin compared to the western one. A more peculiar north-south inhomogeneity is also observed, i.e., the kinetic energy is significantly larger in the north. When the forcing is turned off and the eddies allowed to decay, no significant scale change and no hint of anisotropy is seen; the turbulence simply dies out in a spin-up time scale. No mean flow whatsoever can be detected in either case. But a word of caution is appropriate here: without a current meter in the flow it is difficult to rule out the possibility of mean flows much slower than a typical rms velocity. Indeed recent oceanic observations have shown that statistically significant time averaged Eulerian mean flow can be found superimposed over much more energetic motions. We conclude therefore, that any mean flows were at least an order of magnitude smaller than eddy velocities.

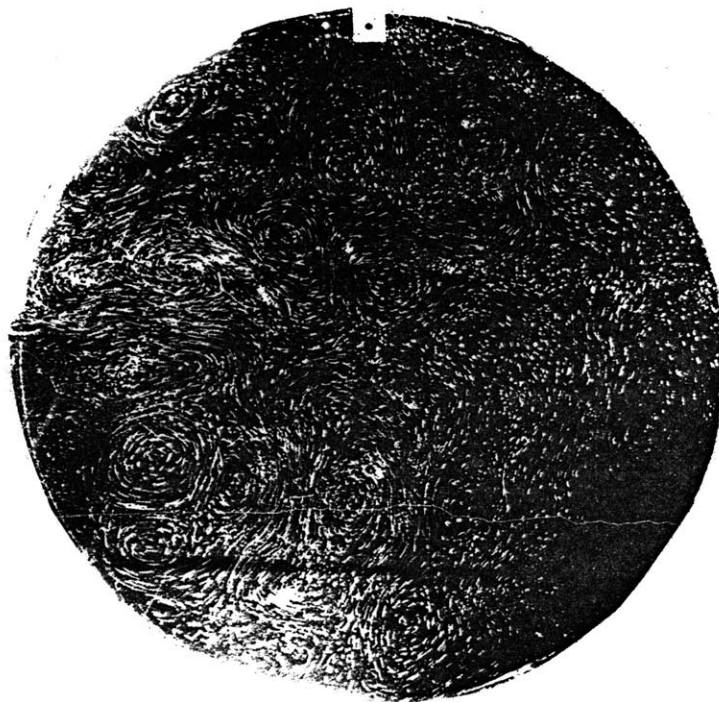
A description of both the forced and the decaying aspects of the turbulence may be found in figures 3-16 and 3-17 respectively. A visual comparison of eddy scale with figures 3-1, 3-2 and 3-9 will convince one that no large scale kinetic energy cascade was found in either the forced or decaying experiments.

To present an intercomparison of the various runs explored, both spatial kinetic energy and eddy length scale estimates were made. The latter were roughly computed by counting the number of velocity reversals normal to a straight line drawn on a streak photograph. This was averaged for many such lines. Such a "mean radius" of typical eddies is thought to be a crude estimate of the zero-crossing of the transverse correlation function. It enables one to compute an important parameter, namely

$M = 4\pi^2 \cdot \frac{u'}{\beta L^2}$. M is a measure of the non-linearity in the vorticity



3-16 (a) 2D turbulence in the sliced cylinder model: the steadily forced case. Laboratory parameter values are $\Omega = 5.1$ rad/s, $\omega = 0.43$ rad/s, $H = 25$ cm, $\alpha = 0.23$, $w = 0.12$ cm/s.



3-16 (b) The state of decay as evolved from figure 3-16 (a).

equation and the ratio of a particle speed to the Rossby wave phase speed for motions of scale L . Table 3-17 summarizes the important results of the above analysis carried out for 5 selected forced runs.

Comparing runs 1 and 3, or runs 4 and 5 shows that doubling the Coriolis parameter doubles the kinetic energy. In the same way a look at runs 1 and 5, or 2 and 4, reveals that doubling the forcing amplitude almost quadruples the kinetic energy. This indicates that the generation term $\overline{w\psi}$ for the mean kinetic energy increases roughly like the square of the forcing amplitude and like the square root of the Coriolis parameter. Although many more runs would be needed to establish the proper power law with accuracy, the tendency is at least exhibited here. Significant zonal inhomogeneity is seen in both energy level and eddy scale. The energy in the western basin exceeds that in the eastern by about 30%. The eddy scale in the east exceeds the one in the west by typically 40%. Significant meridional inhomogeneity is also present, the energy in the north being about 40% larger than in the south. Eddies seem to be fairly isotropic in the west while in the east meridional kinetic energy usually exceeds the zonal part. Greater energy and shorter length scale in the west makes the flow very turbulent there ($M = \frac{U'}{c}$ reading 15), while less energy and longer length scale make the eastern part more linear. At the same time, the fluid could be considered as very diffusive in all those runs since meridional particle excursions were huge compared to the eddy scale.

It is worthwhile to write down the conservation laws for kinetic energy and enstrophy again in order to explain some of the observed inhomogeneities.

TABLE 3-17

Experimental results for the turbulent "sliced cylinder" experiments
(CGS units)

	run 1	run 2	run 3	run 4	run 5	
$\Omega(\text{rad/s})$	3.0	5.1	6.9	5.13	2.75	
$\omega(\text{rad/s})$	0.28	0.43	0.28	0.44	0.28	
w	0.12	0.12	0.12	0.056	0.056	
$\frac{wT}{H}$	0.14	9.5×10^{-2}	0.14	4×10^{-2}	7×10^{-2}	
$\frac{U_{\text{rms}}}{fL}$	1.2×10^{-2}	10^{-2}	10^{-2}	5.3×10^{-3}	7.7×10^{-3}	
Western basin	KE	0.79	1.22	1.56	0.4	0.18
	L	6.3	5.0	4.3	5.8	5.0
	u'/v'	1.	0.97	1.08	1.04	1.1
	M	11.6	13.4	15.0	5.68	9.46
Eastern basin	KE	0.62	0.95	1.17	0.24	0.12
	L	9.5	9.5	5.5	8	7.0
	$\frac{u'}{v'}$	0.92	0.71	1.17	0.79	0.89
	M	4.5	3.5	8.	2.32	3.9
$\frac{KE(\text{west})}{KE(\text{east})}$	1.26	1.28	1.33	1.66	1.5	
$\frac{KE(\text{north})}{KE(\text{south})}$	1.33	1.77	1.29	1.48	1.89	

$$(28) \quad \left(\frac{D}{Dt} + R\right) \nabla^2 \psi + \frac{f\alpha}{H} \psi_x = -\frac{f}{H} w$$

where α is the slope of the top surface, and $\psi = 0$ is the boundary condition at a wall. The total kinetic energy obeys:

$$(29) \quad \left(\frac{\partial}{\partial t} + 2R\right) \frac{\overline{|\nabla\psi|^2}}{2} = \frac{f}{H} \overline{w\psi},$$

and total enstrophy:

$$(30) \quad \left(\frac{\partial}{\partial t} + 2R\right) \frac{\overline{|\nabla^2\psi|^2}}{2} = -\frac{f}{H} \overline{w\nabla^2\psi} - \frac{1}{2} \frac{f\alpha}{H} \oint_{\partial D} |\vec{u}|^2 \sin\theta \, d\ell$$

The fact that the geostrophic contours are now open introduces a new term on the right hand side of (30) as noted by Rhines (1975). ($|\vec{u}|$ is the velocity amplitude along the boundary and θ is the angle of a positively directed vector tangent to the boundary with respect to east.) Arguments put forward earlier to explain the red cascade are no longer valid here because enstrophy may be generated (respectively dissipated) at a western boundary (respectively eastern). This zonal enstrophy inhomogeneity favors small scale motion in the west and larger scale in the east. Rhines then argues that small scale motion propagating slowly will also favor western concentration of eddy energy. These statements, valid for turbulence, rationalize much of what has been observed in the experiments. Nevertheless it is interesting to formulate them using inviscid Rossby wave reflexion properties. Because of the meridional barriers preventing zonal energy propagation, both small scale and large scale waves must exist in the interior. If large scale energy were to increase, small scale energy would increase as well in order to satisfy

the no energy flux conditions, thereby forbidding the red cascade.

Furthermore it is well known that waves of zonal wavenumber k_i impinging on a meridional western wall reflects with a larger wavenumber k_r .

One may show further that:

$$\frac{E_i}{E_r} = \frac{k_i}{k_r} \quad \text{and} \quad \frac{S_i}{S_r} = \left(\frac{k_i}{k_r}\right)^2,$$

where E_i, S_i are the incident energy and enstrophy respectively and E_r, S_r the reflected quantities. This leads again to western energy and enstrophy intensification for the waves.

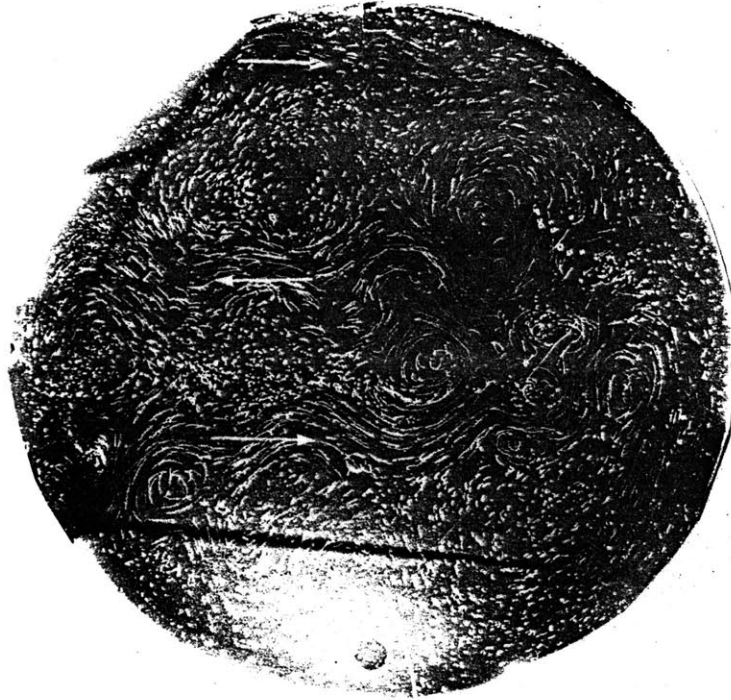
Although the experiments have verified most of the mental pictures developed above, some unexpected features were discovered. The strong meridional energy inhomogeneity belongs to this category. One thinks immediately that forcing or dissipation might act at different efficiencies in both shallow and deep regions if it weren't for the fact that their ratio (in (29) say) is depth independent (assuming that bottom friction is the important dissipative process). This makes it difficult to take any position on that issue. Northern intensification of flows in a beta plane basin is not new however as Veronis (1965) noticed when computing non-linear correction to the "steady" Stommel's solution of the wind driven ocean circulation. Beardsley (1975) also saw northern intensification in the laboratory when studying large scale Rossby waves. He attributed the effect to nonlinearity although the closed particle orbits of his figures indicate a very linear flow. In table 3-18, meridional inhomogeneity is seen to increase as the forcing amplitude is lowered, making a nonlinear mechanism doubtful at best. A possible rationalisation, independent of the generating and dissipative mechanism, might come from

the fact that topographic wave energy tends to build up while moving into shallower water (i.e., a region of higher equivalent beta). This is so because incident rays normal to the topographic contours are bent gradually along the contours and tend to bunch together at a caustic running parallel to the topography. Wave energy is thus focussed at such a singular line.

The last surprise came finally from the absence (or weakness) of rectified mean flows. Relating to the earlier polar beta plane experiments, one is led to believe that efficient mean flow production and large scale spectral cascade are two phenomena which cannot be dissociated. Absence of closed geostrophic contours seems to conceal both. Imagining the simplest steady driving acting in the two geometries (polar beta plane, sliced cylinder) helps to understand the difference of amplitude of steady flows in the two cases. Assuming the bottom surface to rotate steadily slightly faster than the container, currents of order τ/R will exist in the former geometry, but only of order $\frac{\nabla \times \tau}{\beta}$ in the latter, their ratio being large (of order $\frac{L\beta}{R}$) in the inertial regime. (τ is the applied stress, L its scale). This is a quite plausible "interior" scaling but caution is dictated because we know that western intensification in the sliced cylinder may sustain swifter local flows of order τ/R also. The above interior argument is only suggestive of the mean flows differences observed in the turbulent experiments. Geophysically this seems to bear upon the large differences of the ratio of mean over eddy kinetic energy found in the atmosphere of the earth and in the oceanic basins.

Concerning the gyre scale inhomogeneity of the eddy kinetic energy in the ocean, one may reasonably hope that the rough picture developed by

north



3-18 The fluid response to an isolated, oscillating dipole in the sliced cylinder ($\alpha = 0.095$). The darker circular region in the east indicates the position of the dipole.

Swallow (1961) will be improved through the considerable efforts of the POLYMODE experiments. The present experiment suggests a drop in time dependent barotropic energy of about 30%, going from the western to the eastern basin.

To close this paragraph, a very brief description of a complementary experiment in the sliced cylinder will be made. The forcing in this experiment consisted of an oscillating source sink dipole oriented normally to the latitude lines and situated east of the center of the tank. With large amplitude but isolated forcing, strong rectified mean flows lying west of the dipole built up after half a dozen periods of oscillation. Figure 3-18 shows both the structure and direction of the mean flows. The mean flows are now concentrated close to the forcing latitude, westward in the north and eastward in the south, with the circulation closing itself at the western wall where an intense meridional current flows southward with boundary layer character. It overshoots inertially before turning back east again. A large, somewhat more intermittent, anticyclone can also be found north of the westward flow. The same consistent pattern was found to hold for many runs in which bottom slope, rotation, forcing frequency and amplitude were varied. This experiment was designed to test the effect of meridional walls on the qualitative mean flow picture found by Whitehead in his polar beta experiments. The changes (as witnessed by the mean gyre in 3-18) are profound. It is interesting to observe that turbulent interaction of isolated eddies (rather than closely packed as in the preceding case) leads to the generation of strong inertial mean flows in this model. It is fair to say that the direction and sense of the mean circulation have so far eluded theoretical interpretation.

PART THREE

Certain novel aspects of the classical interaction of Rossby waves with a mean zonal flow are discussed here in the light of new experimental results. Meteorologists, having the westerlies at hand, identified the large scale perturbations of the jet streams as quasistationary Rossby waves embedded in the mean zonal flow, and developed the barotropic instability theory of such flows. Oceanic evidence for both Rossby and topographic waves has been reviewed in a comprehensive way by Rhines (1977). Simulated by possible geophysical implications and by the importance of mean flows in general for transporting passive markers far away from their source, it is wished to explore certain aspects of the role of wave momentum flux carried by Rossby waves and the various conditions under which it may be used to accelerate mean flows. Although the concepts embodying the energy propagation at the group velocity by wave packets are built up on solid theoretical grounds for both linear and nonlinear waves in homogeneous slowly varying media, it appears that the mean momentum associated with waves in fluids does not lend itself to an easy interpretation as say, in electromagnetic waves. However for dispersive waves a knowledge of the direction of energy travel implies a well defined wavecrest orientation. This anisotropy is associated with a mean wave stress which may be used to accelerate a mean flow if genuine radiation from a forced region occurs. Another radically different approach makes use of vorticity mixing concept introduced by Taylor (1915) and used in geophysical situations by Rhines (1977). In unforced regions, some reasonable knowledge about the diffusivity of turbulence is sufficient to predict the mean currents in the fluid.

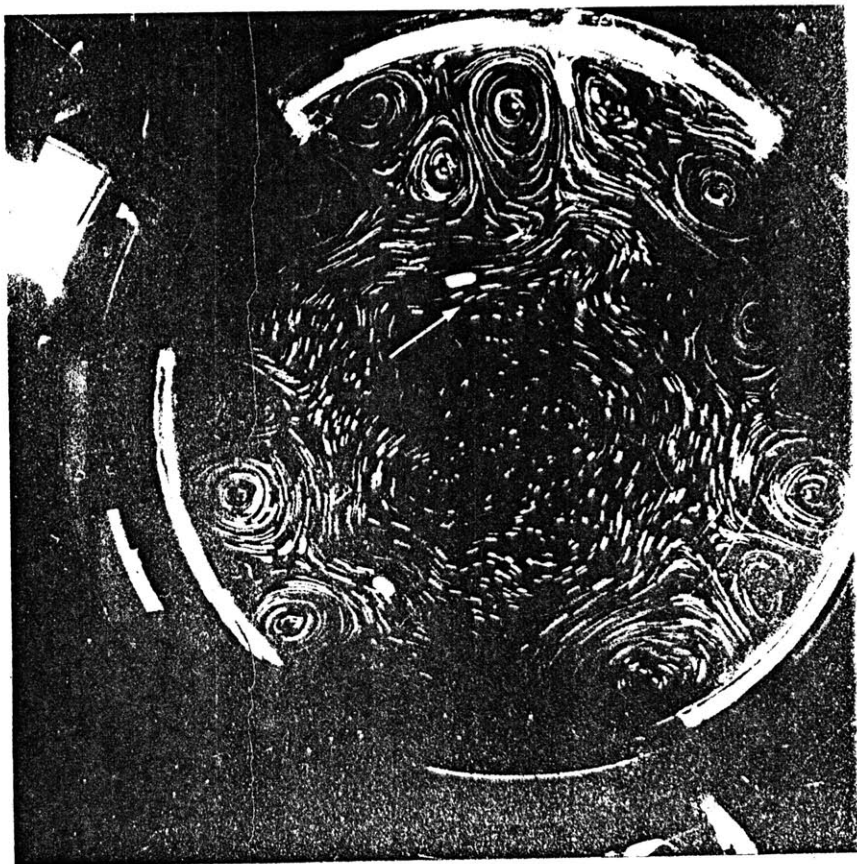
I. Mean flow rectification by topographic Rossby waves

Rossby wave radiation was invoked in an oceanic context by R. Thompson (1971) for explaining the systematically negative Reynolds stress (\overline{uv}) of long period motions at site D north of the Gulf Stream. The latter was suggested as a likely energy source, for the topographic Rossby wave dispersion relation associates northward group velocity with negative stresses. In the laboratory, Whitehead's experiment is just a variant of this mechanism. The present experiment relies freely upon these ideas, the novel feature being a rather sophisticated forcing mechanism, which allows one to visualize quite well the forced eddies and the mean circulation.

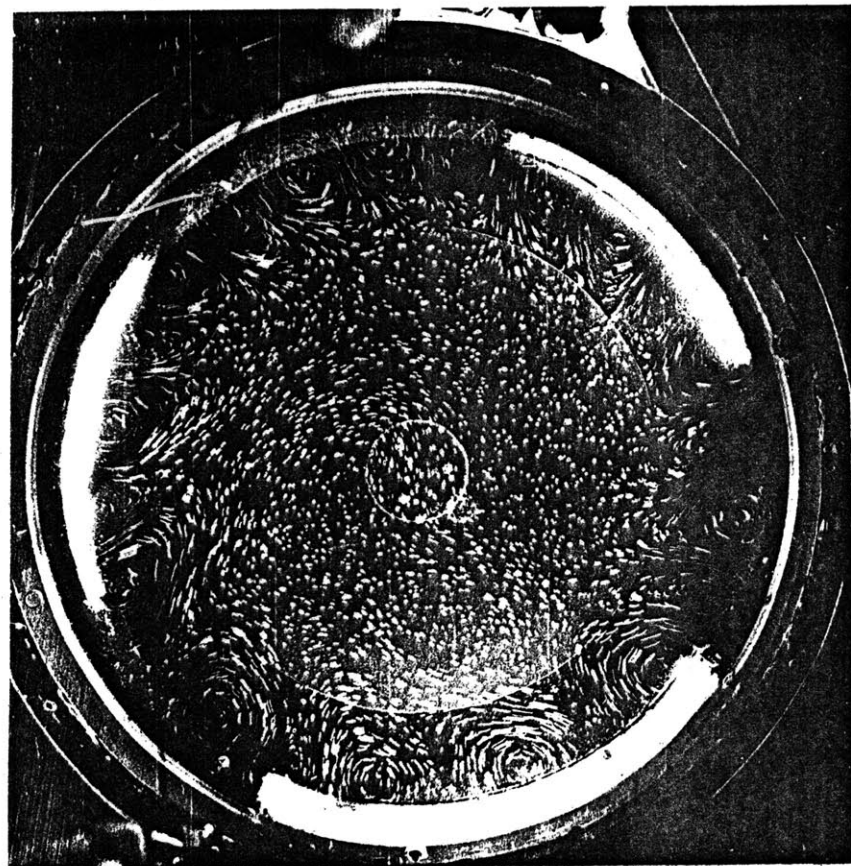
The geometry used is the polar beta plane with a free surface. Driving is provided by a zonal ring of sources and sinks distributed along the outer wall. As explained in Part I, the use of the forcing manifold allows the generation of a wave travelling in a prograde or retrograde sense. A zonal wavenumber of 12 was chosen to favor both zonal homogeneity and possible nonlinear interactions. A typical experiment was run as follows: when a state of rest is obtained in the rotating frame, the forcing is impulsively turned on until a steady state is reached after a few spin-up times. Both transient and steady state were recorded photographically. The evolution of the flow pattern, when the forcing influence propagates westward, may be seen on figures 4-1 and 4-2. The northwest-southeast tilt of the eddies in the transient phase and the mean westward circulation found in the steady state are very clear features.

It is planned to present first an essentially linear analysis of the small amplitude flow and then to focus on an alternative exposition

4-2 The steady state. The parameters are as in figure 4-1.



4-1



The Rossby wave transients induced by the switch-on of the westward travelling ring forcing at the outer boundary. Laboratory parameter values are $\Omega = 3.06$ rad/s, $\omega = 0.4$ rad/s, $H = 7$ cm, $Q = 363$ cm³/s, $E = 6.8 \times 10^{-5}$, $U/fL = 2.5 \times 10^{-2}$.

of vorticity mixing theory whose validity remains at large amplitude. In both sections some efforts will be made to confront experimental data against theoretical results. The very striking spin down experiment will be described separately at the end.

A. Rossby wave resonance, wave stresses

Although the forced waves have a scale much smaller than the dimensions of the basin, it is to be expected that minimizing frictional effects will enable wave resonance to show up, allowing the experimental determination of the frequencies of the inviscid free Rossby modes. The wave frequency varying like f^3 and the inverse of the spin down time R like $f^{\frac{1}{2}}$ (f being the Coriolis parameter) such advantage was gained by going to high rotation rate. In practice, one is limited in reaching too high values because the fractional depth change must remain small within the quasigeostrophic approximation. In the present geometry this turns out to be a condition of small Froude number $\frac{f^2 L^2}{gH}$. For order one aspect ratio container, a small slope of the free surface is thus required. This constraint of small Froude number renders negligible the vortex stretching caused by free surface motions. Keeping in mind this parameter regime, an optimum value had to be found for the Coriolis parameter. (Notice that a change in the depth of the fluid will not affect the value of the quality coefficient $Q = \frac{\omega}{R}$ of the "cavity" remembering that Ekman friction is the important dissipative mechanism here.)

The linear, steady, forced solution may be found by solving the following vorticity equation:

$$(1) \quad \frac{\partial}{\partial t} (\nabla^2 \psi - \frac{\psi}{\lambda^2}) + \frac{\psi_{\theta}}{4\lambda^2} = -\varepsilon \nabla^2 \psi - \frac{w}{H}$$

with $\psi = 0$ at $r = a$.

Local north is at the shallow center of the container, time has been nondimensionalised by the Coriolis parameter and $\varepsilon = R/f$. The inviscid free normal modes are:

$$(1) \quad \psi_m = J_n \left(\eta_m \frac{r}{a} \right) e^{i(\omega t + n\theta)}$$

J_n is the n^{th} order Bessel function of the first kind, and η_m its m^{th} zero. The dispersion relation needing to be satisfied is:

$$(2) \quad \omega_m = \frac{n}{4(1 + \eta_m^2 \frac{\lambda^2}{a^2})}$$

As usual it associates large frequencies with large meridional scale (small η_m). The radial equation derived from (1) having a turning point, the radial envelope of the normal mode J_n changes its nature as its argument is smaller or larger than n . Thus when r is greater than $r_c = \frac{a \cdot n}{\eta_m}$, the Bessel function has oscillatory character while for smaller values of r it is evanescent. This corresponds physically to the impossibility for a wave packet starting from the outer wall to reach the center. As it moves into shallower water, beta decreasing linearly, its meridional scale must increase. This augments and bends the group velocity more eastward till the packet is essentially reflected at a critical latitude, limiting thereby further meridional penetration of energy.

Again the normal modes satisfy also the nonlinear version of (1). The forced solution is found by expanding the forcing over the normal modes. The following forcing function was chosen:

$$w = w_0 \frac{\delta(r - r_0)}{r} e^{i(\omega t + n\theta)}$$

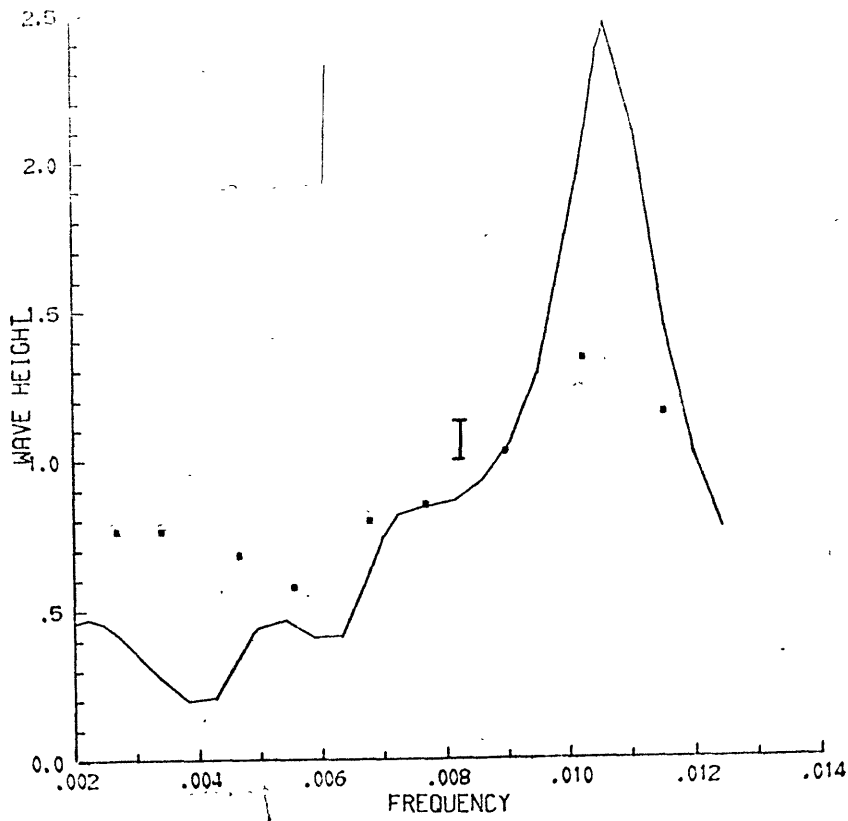
The radial part is idealised by a Dirac δ function rather than a more distributed forcing as in the experiments. This simplification is probably a good one when the scales of motion are larger than the effective size of the driven region. The travelling wave is assumed to be harmonic in the zonal direction and in time although a square wave was forced in the experiments. It will be seen that this richness of harmonics has some important consequences in the nonlinear regime but of no real concern here. At any rate the nondimensional solution of the forced equation turned out to be:

$$(3) \quad \psi = \Re \left\{ 2e^{i(\omega t + n\theta)} \sum_{m=1}^{\infty} \frac{[i(\omega - \omega_m) - \epsilon]}{[(\omega - \omega_m)^2 + \epsilon^2]} \frac{J_n(\eta_m \frac{r_0}{a}) J_n(\eta_m \frac{r}{a})}{\eta_m^2 [J_{n+1}(\eta_m)]^2} \right\}$$

in which the approximation $\frac{a}{\eta_m \lambda} \ll 1$ has been made. This is valid for comparing with our experiments because $\frac{a}{\lambda}$ never exceeds 2 or 3 and the smallest value of η_m is 16.70 for a mode of number 12.

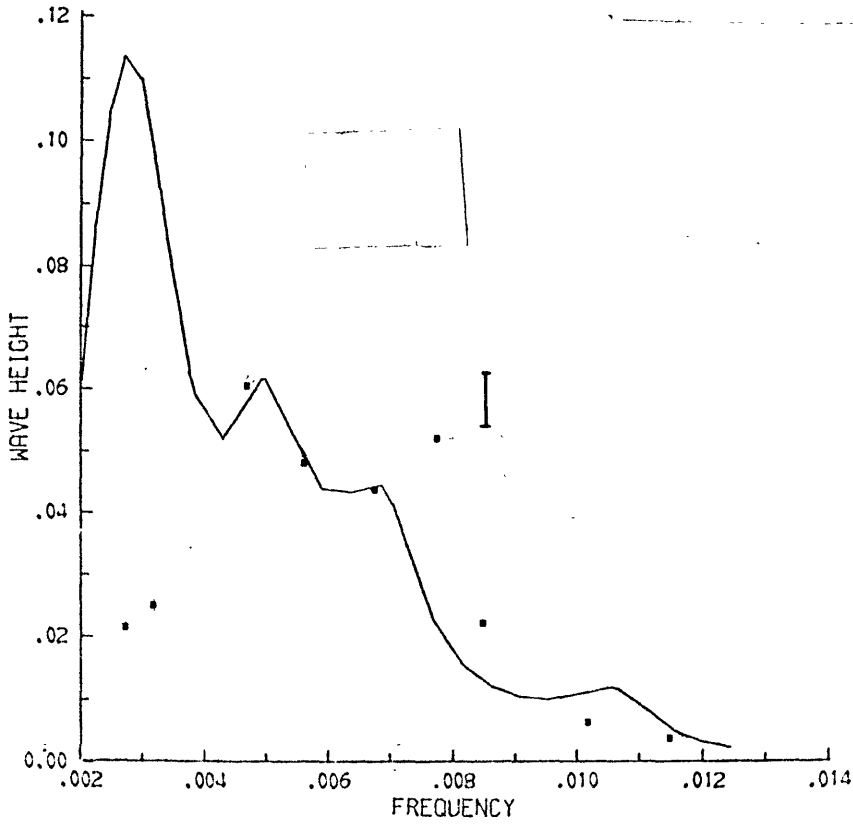
The easiest check to see if the solution (3) has anything to do with the experiment is to sense the free surface elevation as a function of time and compare the rms pressure with the amplitude found from (3). There is however an unknown adjustable parameter which is the forcing amplitude w_0 . Although the mass flux is known, there are no direct ways of inferring the vertical velocity because the effective area of sources and sinks covered by a diffuser is essentially unknown. Instead the present comparison provides a way of estimating it. This value was then used to scale the data at other frequencies.

RØSSBY WAVE SPECTRUM, R1=24



-a-

RØSSBY WAVE SPECTRUM, R1=12



-b-

4-3 The resonance curves: plain curves are deduced from the theory, dots represent experimental values.

(a) The near-field region

(b) The far-field region.

Pressure was measured using capacitance probes at two points in the tank, one in the near forcing region and one in the far field. Because the Rossby wave pressure signal is very small one could not go as low in forcing amplitude as one wished for a test of linear theory. The smallest free surface elevation that we could detect with still a good signal over noise ratio was about 50 microns. This corresponded to particles speed of the order of the phase speed for the gravest Rossby modes, making a linear comparison still a rough one.

Figures 4-3 show the comparison between experimental data and the theoretical curves computed from (3). One can see that a reasonable agreement exists for the general frequency dependence. The lowest mode is slightly resonant in the near field but the theoretical resonance curves look sharper. At low frequencies the comparison becomes a bad one as nonlinearity creeps in. The spectral broadening of the empirical curves was seen very clearly in runs of increasing forcing amplitude. This is to be expected from the general tendency for nonlinearity to whiten spectra. One will notice in figure 4-3 (b) that the presence of beta critical latitudes is well demonstrated: the driving frequency must be below a certain cut-off for any wave energy to reach the far field probe. Again from runs with increasing forcing amplitude, one could see more and more energy tunneling through the critical latitude when the driving frequency was above the "linear theory" low frequency cut-off.

A further and more important check on the validity of the linear theory could be provided in a simple way by the versatility of the forcing mechanism. The well ordered "steady" waves found in the retrograde case (Figures 4-1, 4-2) were replaced by quite an unsteady, messy pattern when the forcing moved in a prograde sense showing that the fluid dis-

liked such excitations. To have quantitative estimates of that repulsion, three pressure traces shown on figure 4-4 were obtained in the near and far field region when a large constant amplitude forcing pattern moved in a prograde or retrograde sense, or did not move at all. The enhancement of the signal for the retrograde case demonstrates quite clearly the necessity for the forcing speed to match the Rossby wave speed in order that significant motions be produced. For smaller forcing amplitude the signal corresponding to the prograde case looked exceedingly small.

The question of the mean wave stresses will now be discussed. Although all the needed information is contained in the exact solution (3) the mathematical form is not very enlightening. A more suitable, qualitative approach might be to rely on the wave packet concept in an infinite medium as developed by Lighthill (1967). In order for wave forms varying like $e^{i(kx - \omega t)}$ to be solutions of the vorticity equation, the following dispersion relation is required:

$$\omega = - \frac{\beta k}{k^2 + l^2}$$

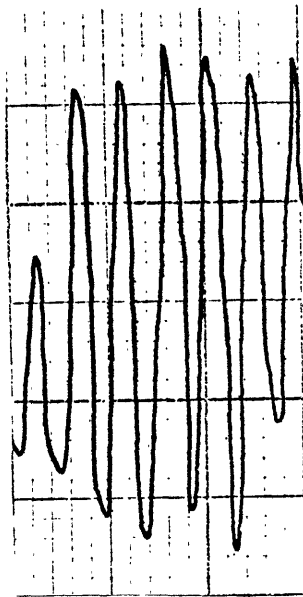
k and l denote the zonal and meridional wavenumber respectively.

Lighthill demonstrates that travelling forcing effects generate waves whose crests are stationary relative to the velocity of the forcing region. Away from the westward moving forcing region, they will be found in the direction of the relative group velocity with wavenumbers satisfying:

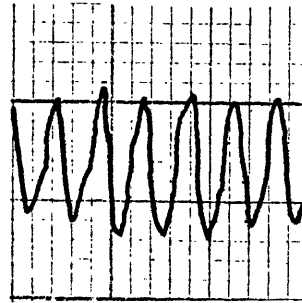
$$-\frac{\beta k}{k^2 + l^2} = -kU, \quad U > 0.$$

The possible wavenumber vectors may lie on the l axis and on a

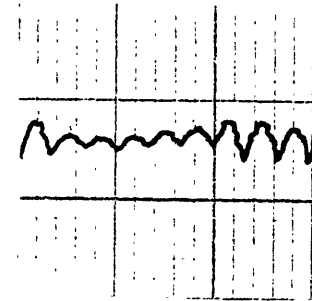
NEAR FIELD



-a-

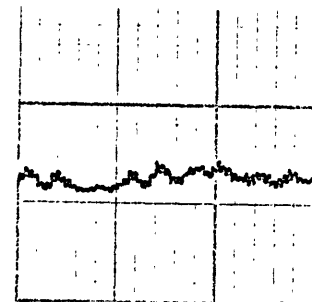
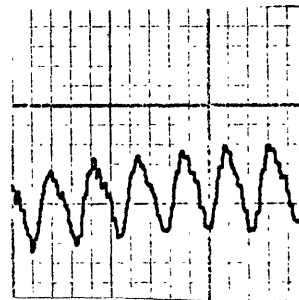
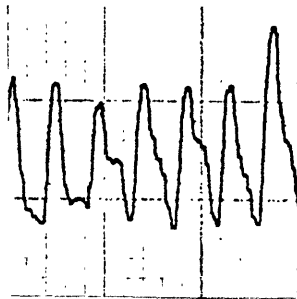


-b-



-c-

FAR FIELD



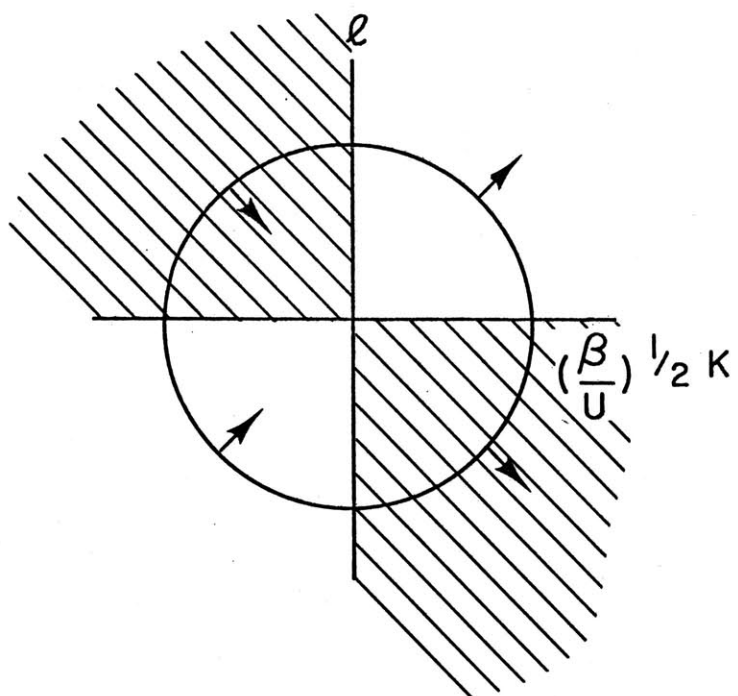
4-4 Pressure time series for different directions of propagation of the forcing:

- (a) retrograde
- (b) prograde
- (c) stationary.

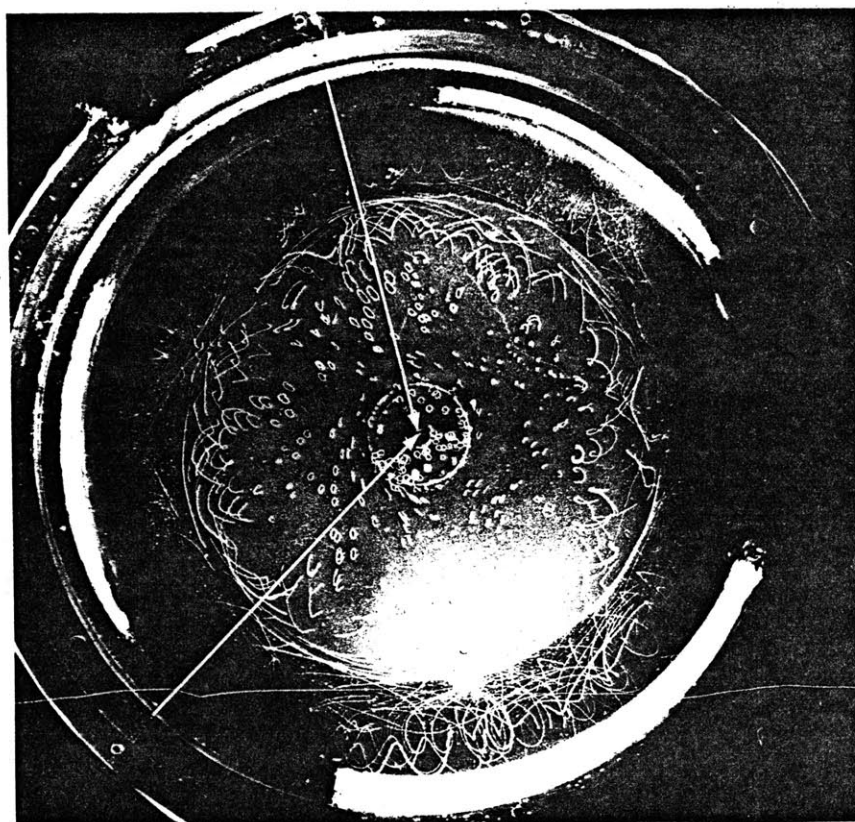
The forcing intensity is such that $\frac{c}{U} = 1.5$

circle of radius $(\frac{\beta}{U})^{\frac{1}{2}}$ centered at the origin. The former family with zero zonal wavenumber will not be excited because our forcing spectrum has no energy there. On the other hand, wavenumbers lying on the circle will be excited. On figure 4-5 we have plotted this locus with the direction of the group velocity. It is seen that all waves trail the forcing pattern as the group velocity points toward the east. Since the forcing region in our experiments is bounded to the south by a wall, the northern interior will be filled up by waves found in the first and fourth quadrant of figure 4-5 exclusively. This indicates in turn a northwest-southeast orientation of the wave crest. This orientation could be seen very clearly in movie films. In order to include the evidence here, long exposure photographs over one forcing period were made for small amplitude forcing so that particle paths were essentially closed. Figure 4-6 reveals the elliptical orbits with orientation as deduced from the theory. One may also see that the size of the ellipses decreases going north because of the usual geometrical spreading of energy going away from a source. These two effects, orientation and varying size of the orbits, are just the necessary ingredients to produce a positive divergence of the waves Reynolds stresses. The net westward mean flow which results may thus be considered generated by Rossby wave radiating away.

As suggested earlier this wavelike mechanism for westward mean flow generation away from energy sources is recovered by the large amplitude validity of the vorticity mixing theory. Along with its exposition the interesting nonlinear phenomena arising from the experiments with the retrograde forcing pattern will now be discussed.



4-5 Locus of wavenumbers excited by a westward propagating forcing. Arrows indicate the direction of the group velocity relative to the forcing.



4-6 Long exposure photograph, revealing the tilt of the particle orbits.

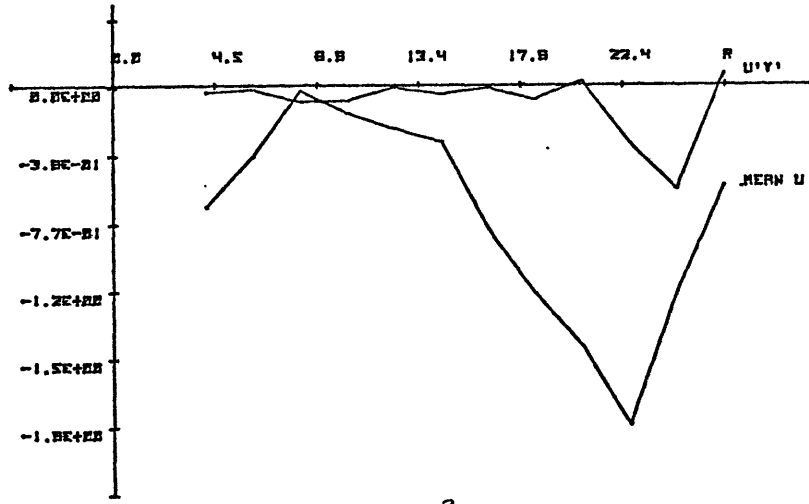
B. Potential vorticity mixing and associated finite amplitude effects

The stage for the matters to be discussed has already been set in Part II, paragraph B. One must emphasize that investigation of a mean flow acceleration as a divergence of a Reynolds stress is of little informative value usually, because the concept accumulates in itself possibly different physics. The novelty of a vorticity mixing approach is that it allows the explicit separation of the free and forced contributions to the Reynolds stress. Although what one can say about forced regions is limited, considerable intuition is available to predict mean flows over the free latitudes of a forced beta plane as shown by Rhines' explanation of Whitehead's experiment.

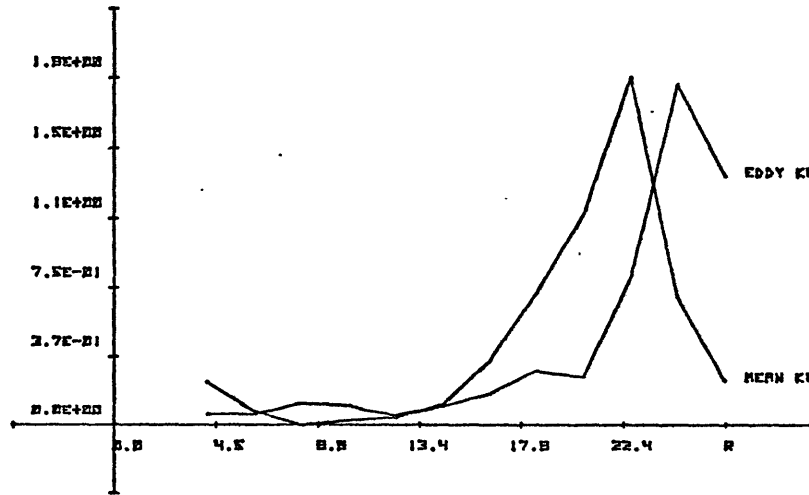
The starting point is the expression (15) in Part II. The transport of the initial potential vorticity by the eddies $\overline{q_0 v}$ can be rewritten as $-\beta \overline{k}$, \overline{k} being the usual zonally averaged meridional diffusivity of fluid parcels from their rest latitude. One obtains equivalently:

$$(4) \quad \overline{qv} = -\beta \overline{k} e^{-Rt} - R\beta \int_0^t \overline{k}(\tau) e^{-R\tau} d\tau + \int_0^t \overline{vF} e^{R(t'-t)} dt'$$

This expression predicts that at free latitudes y , where no contribution to \overline{qv} comes from parcels having wandered over "steadily forced" latitudes, a westward mean flow is to be expected both in the transient regime (from the first term in (4)) and in the steady case (from the second term in (4)), because of the positive diffusivity induced by the continuous forcing. This is clearly what happened in the experiments as witnessed by figures 4-1, 4-2. The meridional structure of the mean flow and the Reynolds stress is shown in figure 4-7 for a large amplitude run. Not represented thereon is a persistent eastward flow



- a -



- b -

4-7 Experimental values of the zonally averaged fields as a function of radial distance in the topographic Rossby wave experiment. The experimental parameter values are $\Omega = 3.83 \text{ rad/s}$, $\omega = 0.4 \text{ rad/s}$, $H = 10 \text{ cm}$, $Q = 363 \text{ cm}^3/\text{s}$.

(a) westward mean flow and Reynolds stress

(b) eddy and mean kinetic energy.

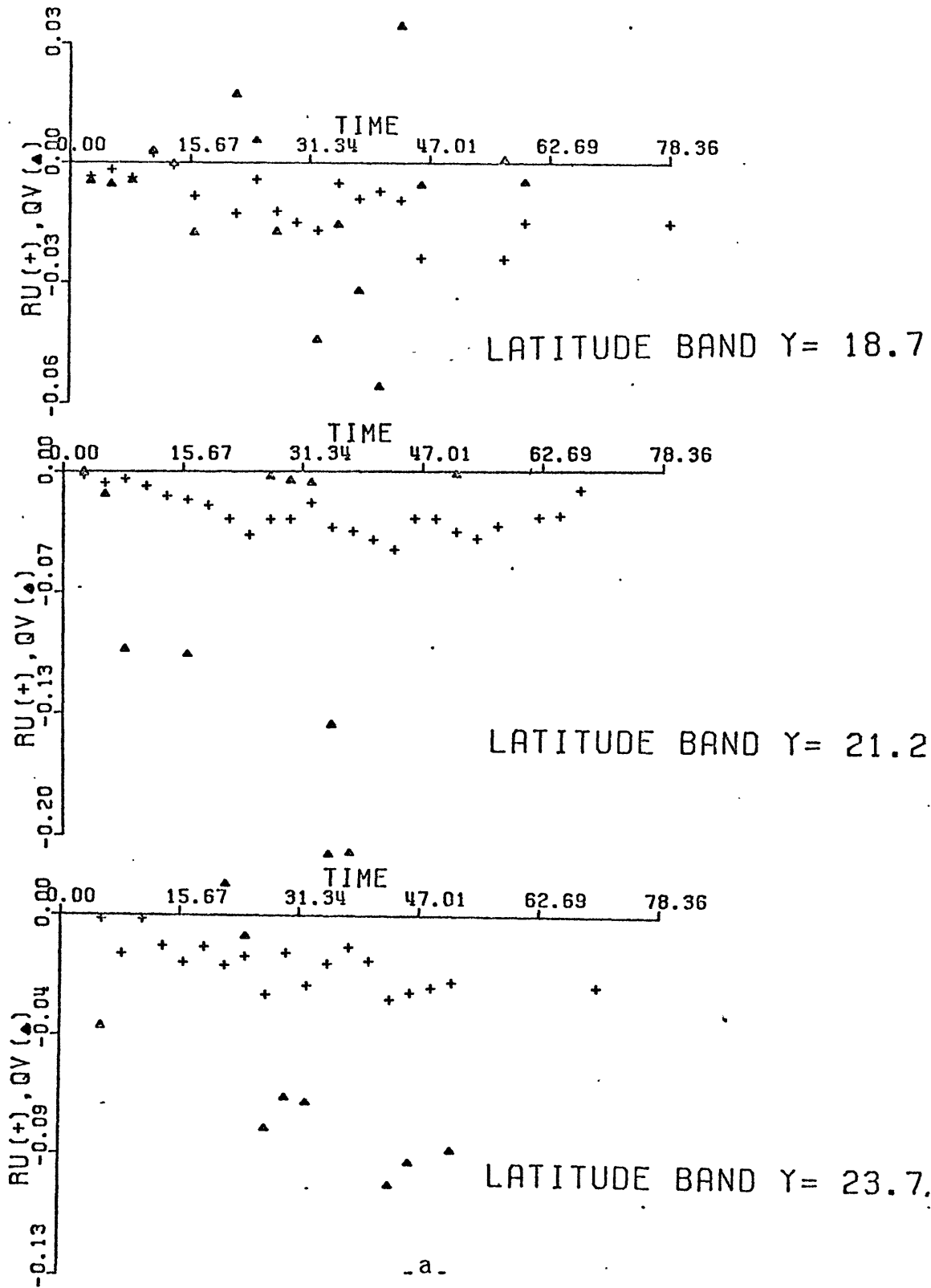
found over the forcing region quite close to the southern wall. Lighting deficiencies prevented accurate measurements there. This prograde mean flow is nevertheless an essential ingredient to balance out the total angular momentum. Again the precise way by which correlation forcing-meridional velocity build up in (4) to reach that goal is obscure.

As may be seen on the photographs, the anticyclones have disappeared over the ring forcing regions. The retrograde sense of the interior mean flow is evidently just what is needed to intensify cyclones and weaken anticyclones at the forcing latitudes. A further check on this process was carried out by devising the same experiment but replacing the upper paraboloidal surface by a rigid flat lid. Initially small eddies of either sign were found in the driving region. They exhibited the usual tendency to grow to larger scales "irrespective of their signs". The beta effect introduces therefore an asymmetry: the anticyclones grow preferentially to larger scales (to form the westward interior mean flow) while cyclones stay at smaller scales tied up to the driven region. As in the polar beta plane turbulence case, one may show however that the area-averaged $\overline{\xi y}$ correlation vanishes because of forcing axial symmetry.

It was decided finally to test the steady part of relation (4) directly. At free latitudes, the amplitude of the westward flow must finally equilibrate to $\beta \int_0^t \overline{k(\tau)} e^{-R\tau} d\tau$. A number of Lagrangian particle paths were extracted from movie films, and digitized for building up zonally averaged Lagrangian velocity correlation. Being forbidden to average meridionally or temporally by the nonhomogeneity and nonstationarity of the statistics made the calculation difficult, for at any given time and any given latitude, a large number of fluid parcels just crossing the control line is needed for constructing meaningful zonal averages.

We never had enough! To increase the number of degrees of freedom, the zonal average was applied to a narrow latitude band rather than to a line as in (4). Fixes were taken roughly every fifth of a wave period, an operation which effectively low pass filter the data. This does bias the small time behavior of the empirical diffusivity but must leave the large time behavior essentially unchanged. The steady part of \overline{qv} involves a time integral of the diffusivity weighted by an Ekman friction term, one may reasonably think that the bias from the temporal sampling will decrease as $\frac{R}{\omega}$. With typically more than 700 fixes spread over a spin up time scale, it was found that the number of degrees of freedom at a given time and latitude band oscillated between 5 and 15, which indeed is not very much in view of the large amount of data input. Bearing in mind those inescapable limitations, the results of such free latitude computations are shown on figure 4-8 for the transient and steady case respectively. The meridional transport of potential vorticity is always negative and has roughly the same magnitude as the mean flow divided by the spin down time, indicative of a (only) gross qualitative agreement with the theory. Increasing the data base for improving further the statistics seemed both unrewarding and prohibitive: doubling the number of fixes would decrease the sampling error by a factor of $\sqrt{2}$ only.

Although visual information was adequate for revealing the mean flows, the primary goal of this experiment, pressure time series turned out to be invaluable here for unraveling the associated finite amplitude modifications of the Rossby waves. As before the probes were set up in the near and far field. Several runs with constant, large forcing amplitude and of decreasing frequency were made. Although not much modification occurred at the near field instrument, the interior probe showed



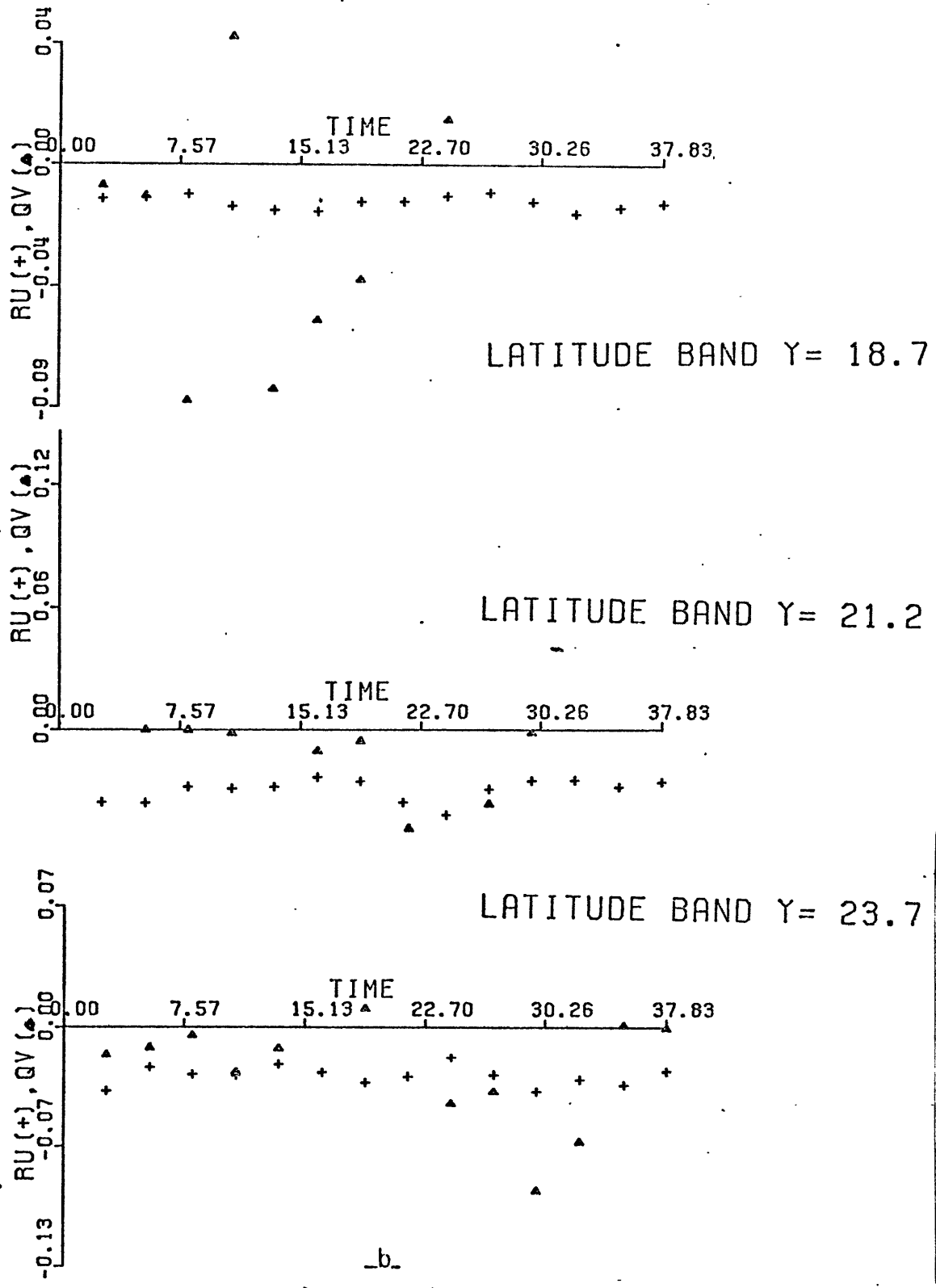
- a -

4-8 Experimental comparison of mean flow acceleration and potential vorticity flux at free latitudes:

(a) the initial value problem

Laboratory parameter values are $\Omega = 4.05 \text{ rad/s}$,

$\omega = 0.442 \text{ rad/s}$, $Q = 360 \text{ cm}^3/\text{s}$, $H = 7 \text{ cm}$.



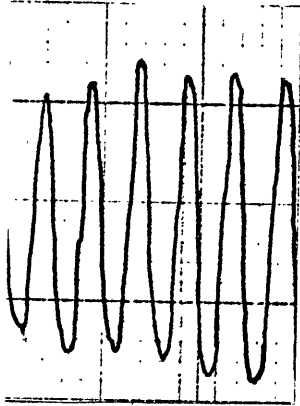
4-8 Experimental comparison of mean flow acceleration and potential vorticity flux at free latitudes:

(b) the steady state

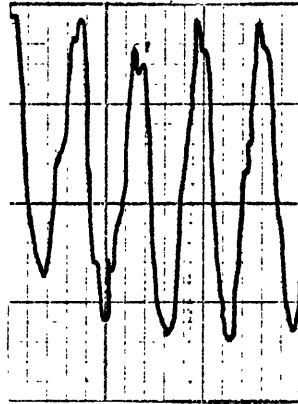
Laboratory parameter values are $\Omega = 4.05$ rad/s,
 $\omega = 0.442$ rad/s, $Q = 360$ cm³/s, $H = 7$ cm.

the build up of second and third harmonics as the frequency decreased. Wave forms are shown on figure 4-9. Digitization of the wave form over "one period of the primary wave" enabled us to construct the high frequency part of the pressure autospectrum. The corresponding spectra to 4-9 are plotted on figure 4-10. Lowering the driving frequency thus broadens the spectra. The observation that harmonics (2ω , 3ω , etc...) occur at an unvariable place on the back of the primary wave train suggest that they travel at the same phase velocity as the basic wave. This indicates that we are dealing with a genuine manifestation of non-linear interaction of the primary wave. The further degeneration of the wave form at lower driving frequencies brings to mind the sideband instability mechanism put forward by Benjamin and Feir (1967) to explain the instability of a quasi-monochromatic surface wave on deep water. Such a possibility for Rossby wave instability requires separate investigation.

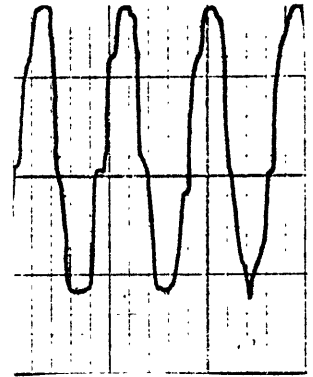
That the disintegration of the primary wave occurs as the driving frequency decreases while the amplitude of the wavemaker remains the same, is not a surprising fact however. The time T_p needed for an energy signal to go from the forcing region to the far field probe varies like the inverse of the meridional group velocity and therefore increases with lower frequencies. The nonlinear interaction time T_i varies like a wavelength divided by particle speed. Since the dispersion relation associates small wavelength with small frequency, one expects T_i to decrease with the driving frequencies. The number N of possible nonlinear interactions of the primary wave as it moves from the forced region to the far-field instrument varies like T_p/T_i . From the above two statements one concludes therefore that N will increase drastically



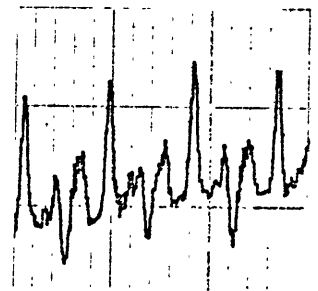
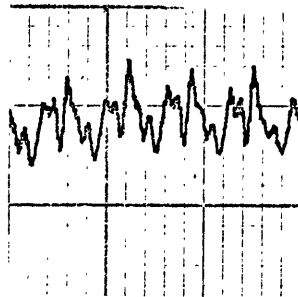
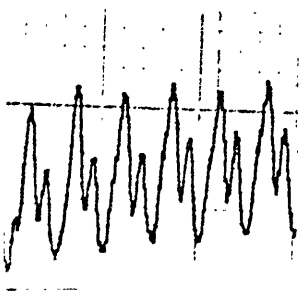
-a-



-b-



-c-



4-9 Wave pressure time series for three distinct frequencies of excitation

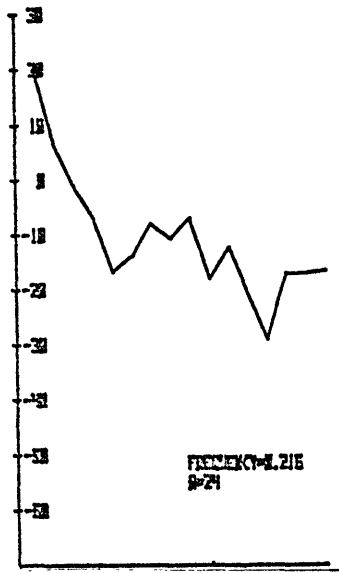
(a) $\omega = 0.216$ rad/s

(b) $\omega = 0.167$ rad/s

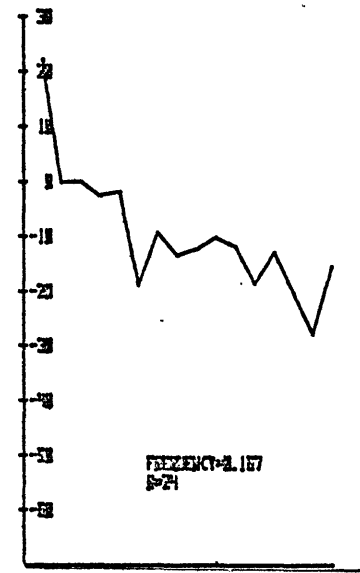
(c) $\omega = 0.124$ rad/s

Other parameter values which were held fixed, are:

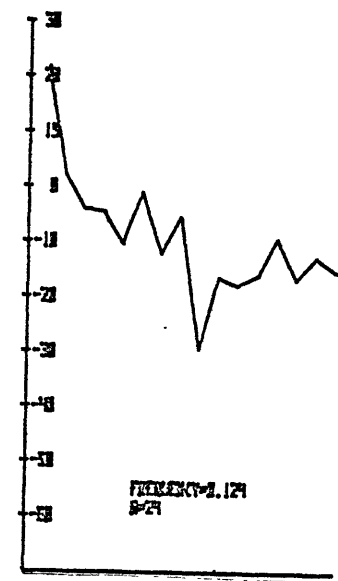
$\Omega = 3.7$ rad/s, $H = 9$ cm, $\varrho = 300$ cm³/s.



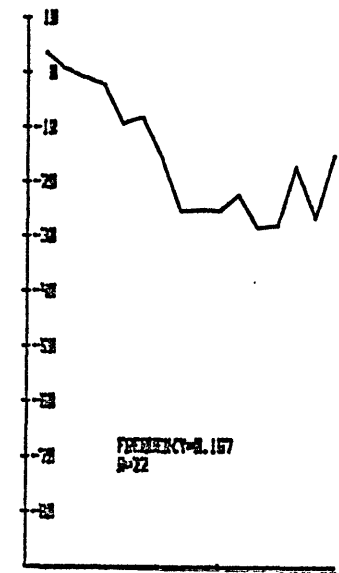
.a.



.b.



.c.



4-10 The pressure autospectra corresponding to figure 4.9

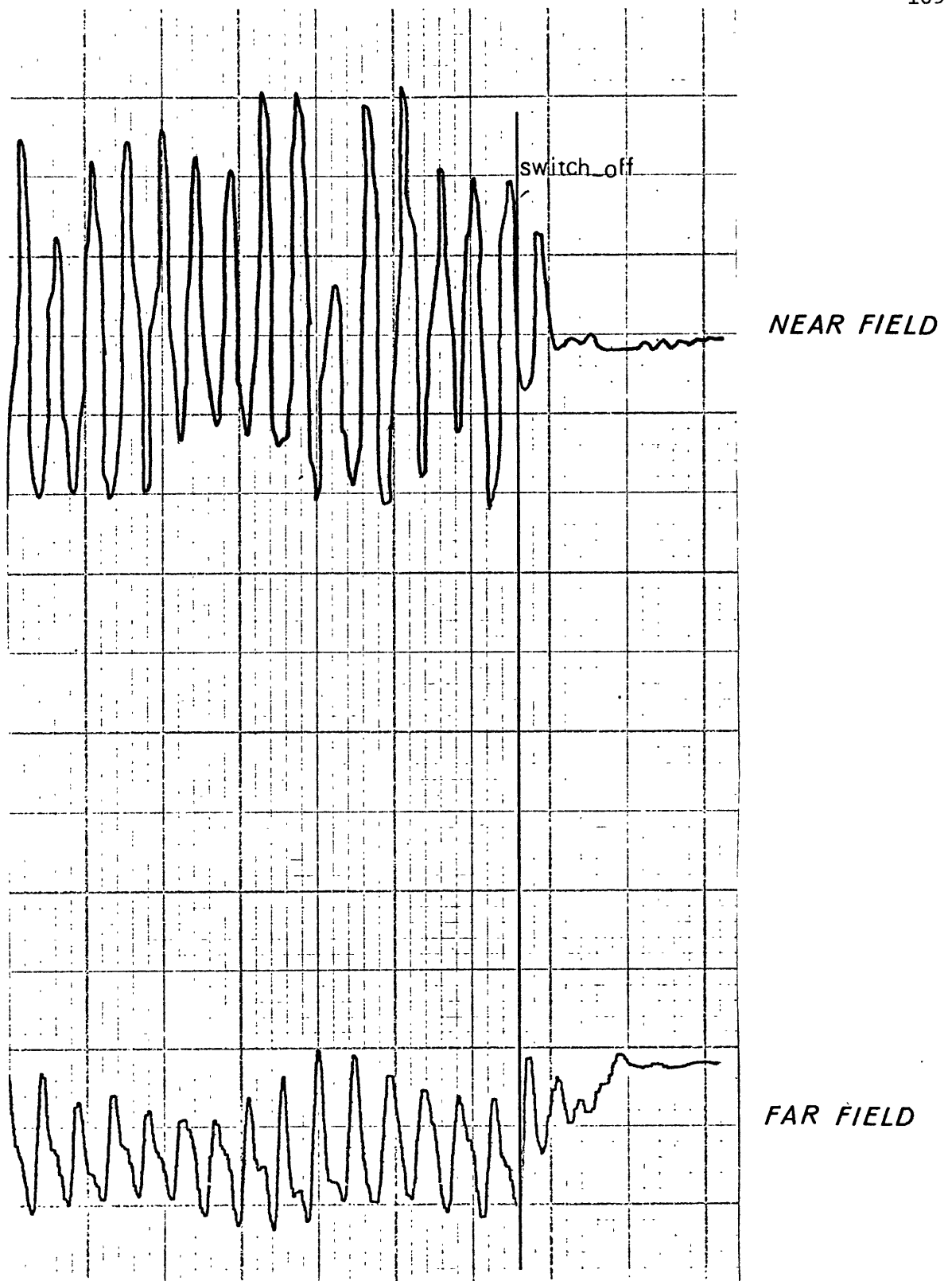
- (a) $\omega = 0.216$ rad/s
- (b) $\omega = 0.167$ rad/s
- (c) $\omega = 0.124$ rad/s.

as the forcing frequency decreases, making thereby the nonlinear energy transfer between Fourier components more promiscuous and complete.

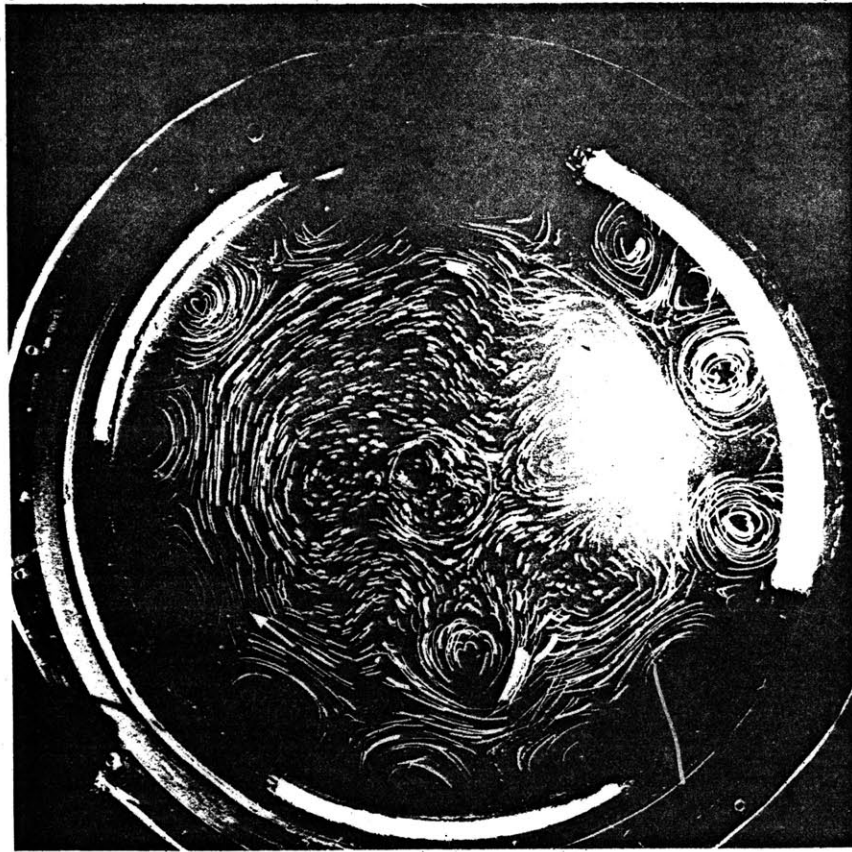
C. The period of decay

When mean flows and eddies reached their steady state, suppression of the driving led at first sight to anomalous behavior. The signals of the fluctuations turned out to be strongly damped as shown on figure 4-11. The damping time scale of the eddies was close to the inertial time scale, itself much smaller than the Ekman spin down time. Such fast disappearance of the signal at a fixed point is due partly to wave energy radiating away from the region of concentrated forcing. However this does not tell the whole story. The evolution of the flow field itself revealed much more. On figure 4-12 compare the initial state with the decaying stage two inertial time scales later. Evidence for unequal disappearance of mean flows and fluctuations seems to be there. To test further the idea, spatial averaging of both mean and fluctuating eddy kinetic energy was achieved as a function of the decay time with results depicted on figure 4-13. The slow (respectively fast) decay of the mean kinetic energy (respectively eddy kinetic energy) compared to the Ekman time scale is particularly significant. On the other hand the total kinetic energy decays with the appropriate viscous time scale. At the same time the meridional distribution of eddy kinetic energy initially concentrated in the south, has spread out uniformly in the basin during the decay while no appreciable change was found for the distribution of the mean kinetic energy.

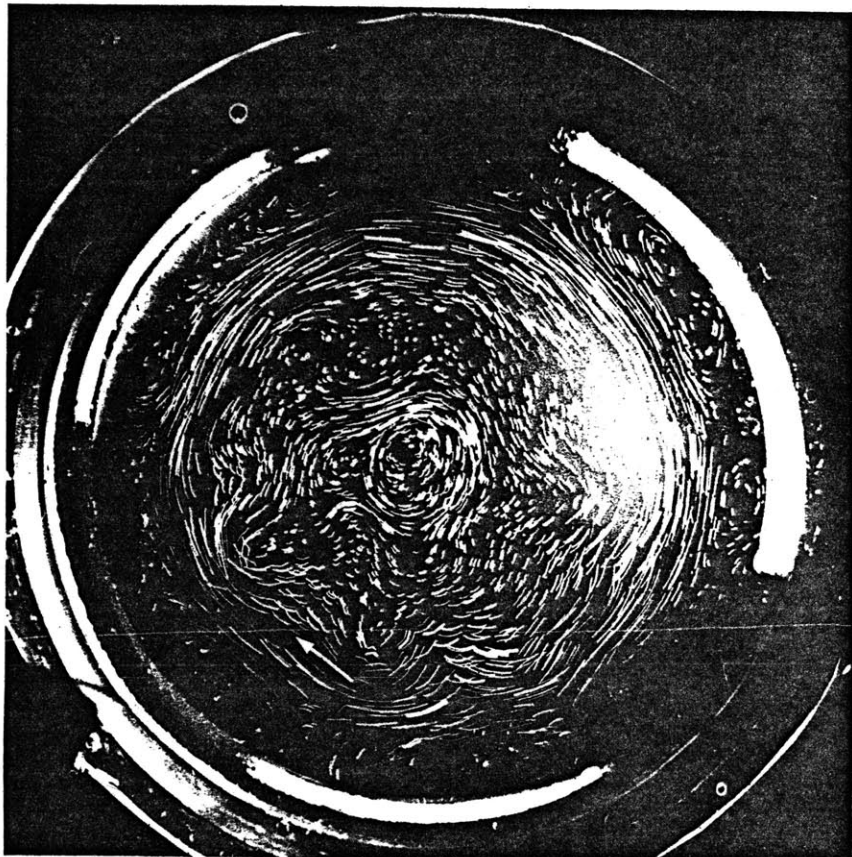
These observations are therefore saying that the westward mean flow is stable to finite amplitude, smaller scale perturbations. In view of the conservation integrals for energy and enstrophy derived in Part II



4-11 A pressure time series showing the fast disappearance of the waves when the driving is switched-off.



.a.

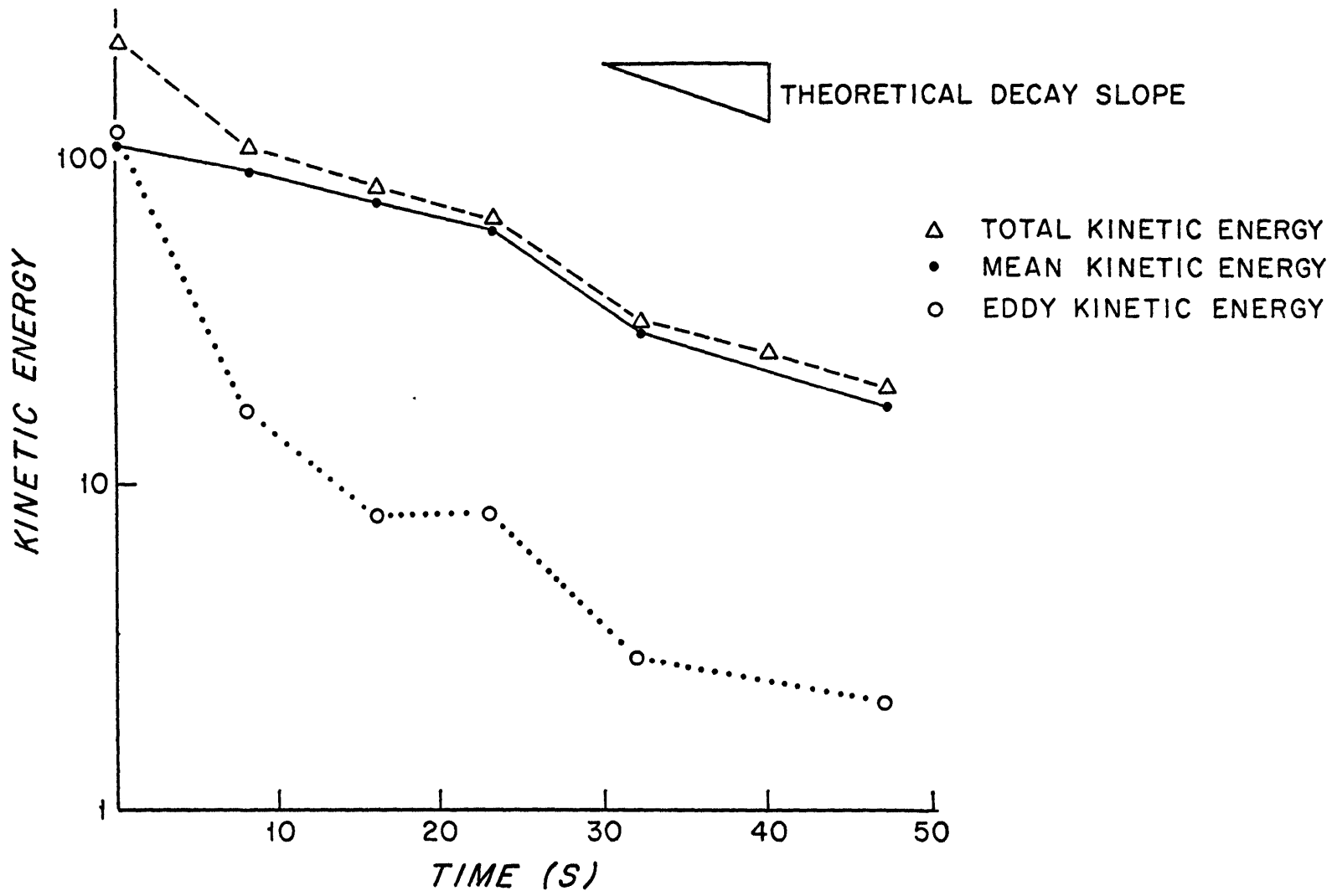


.b.

4-12 The decay period of the velocity field:

(a) the steady state

(b) the decaying state 20 sec after switch-off.



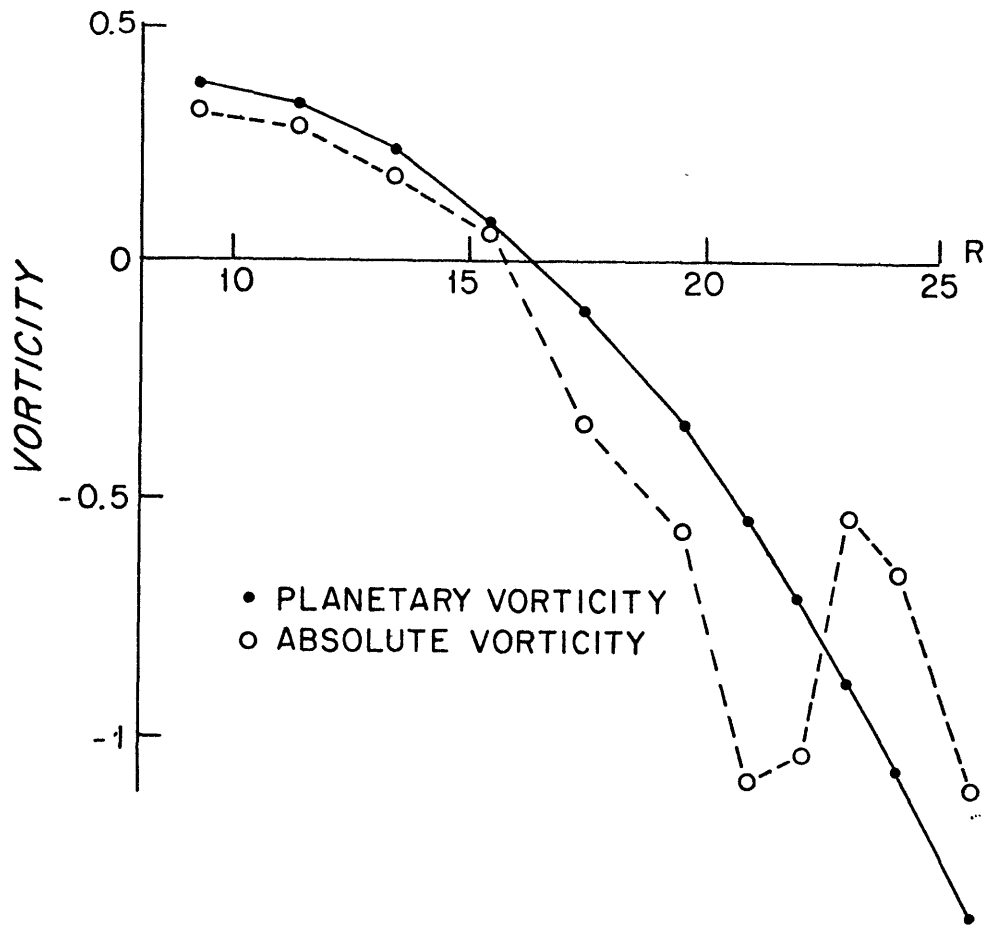
4-13 Temporal decay of mean and eddy kinetic energy.

for the case of a beta plane with closed $\frac{f}{H}$ contours, this is not very surprising. It has been shown there that the energy containing scale must increase in time in freely decaying turbulence. The energy migration from the short waves to the mean flow is after all just following that rule.

The linearised theory of hydrodynamic stability being rather well advanced, it was found interesting to point out the relevance that it bears upon this concrete situation. The barotropic instability of a zonal flow was first studied in detail by KuO (1949) in connection with the large scale fluctuations of the atmospheric westerlies. The perturbations in that context have the nature of shear waves. It is interesting to consider specifically the instability of a westward flow because the perturbations can now be considered as modified Rossby waves whose origin is independent of the existence of a mean flow.

KuO showed that for the flow to be unstable it is necessary that the meridional gradient of the mean potential vorticity $\beta - \overline{U}_{yy}$ vanishes at some point. This condition turned out to be satisfied for the large amplitude runs and the analysis which follows is thus restricted to these cases. This allows unstable waves to exist throughout the flow domain. The mean potential vorticity was computed for a large amplitude run at the onset of the decay and is shown on figure 4-14. The two extremums occur just to the north and south of the band of maximum flow speed. (The corresponding mean flow was depicted on figure 4-6.) Because the potential vorticity gradient vanishes at some point, the actual stability of the westward flow may not be proved without further examination of the linearized theory.

The geometry is that of an infinitely long zonal channel or a beta plane. To investigate the stability properties one first constructs, if possible, a singular neutral wave solution satisfying in this case:



4-14 Experimental values of potential vorticity as a function of radial distance as obtained from figure 4-12 (a).

$$(5) \quad (U - c)(\phi_{YY} - \alpha^2\phi) + (\beta - U_{YY})\phi = 0$$

the stream function being $\phi(y) e^{i\alpha(x - ct)}$.

(5) is to be solved with appropriate boundary conditions at the side walls. It may be shown (Lin (1955)) that the Reynolds stress, which vanishes on the boundaries has a jump discontinuity at the critical point where U equals c . For monotone velocity profiles this implies that $U_{YY} - \beta$ must also vanish at such a critical point for a singular neutral solution to exist. Using these properties the singular neutral solutions can be computed and the remaining task is to investigate the behavior of the solutions around the neutral one. One considers possible unstable solutions with a non zero imaginary part of c , close to the neutral wave solution. To find the sign of c_i for neighboring wavenumbers, one looks at the limit as the unstable solution approaches the neutral solution. The proper limiting process involves the passage of c_i to zero through positive values. Only a consideration of the viscous form of (5) allows the elucidation of this important point (explained at length by Lin).

The result is the following:

$$(6) \quad \left. \frac{dc}{d\alpha^2} \right]_{\alpha=\alpha_s} = \frac{\int_{y_1}^{y_2} \phi_s^2 dy}{\text{pv} \int_{y_1}^{y_2} \frac{k(y)\phi_s^2}{U - c_s} dy + i\pi \frac{k(y_s)\phi_s^2}{|U_y|}}$$

where $k(y) = \frac{\beta - U_{YY}}{U - c}$, ϕ_s , α_s , c_s referring to the neutral solution.

If $k(y)$ is positive throughout the flow, then (6) shows that scales of motion slightly shorter (respectively longer) than neutral are damped (respectively self excited). Within the same hypothesis on $k(y)$, this can be extended by certain related results of Howard (1964) who shows that if the wavenumber of an unstable mode is greater than the largest eigenwavenumber of the singular neutral solution, the flow is stable. His results imply also that, if the boundaries are so close together that the eigenwavenumbers become imaginary then the flow is also stable. The point to be made here is that people interested in the stability characteristics of the westerlies did not use those results extensively because the function $k(y)$ rarely keeps the same positive sign throughout the region of interest. Indeed to satisfy the necessary criterion for instability, an eastward jet profile whose curvature near the axis is negative must possess a point of inflexion allowing the curvature to become positive away from the axis. This makes it very easy for $k(y)$ to change again. Because the natural curvature of a westward jet is positive, no inflexion point is necessary for satisfying KuO's instability criterion, and for smooth profiles, $k(y)$ will usually be positive throughout the channel. In this eventuality, the only remaining problem to decide about the instability is to calculate the eigenwavenumber of the neutral solution. A particular example related to the experiments is appropriate here.

The sine-curve velocity profile being particularly simple to work with the following form of westward mean flow is chosen.

$$(7) \quad U = -(U_1 + U_0 \sin \frac{\pi y}{b}), \quad 0 \leq y \leq a, \quad U_1 \geq U_0 > 0$$

The requirement for a critical point to exist is

$$(8) \quad \sin \frac{\pi y}{b} = R_0 \quad \text{where} \quad R_0 = \frac{\beta b^2}{U_0 \pi^2}$$

If R_0 is smaller than unity, (8) has at least one solution. At such a point y_c ,

$$c = -(U_1 + U_0 \sin \frac{\pi y_c}{b}).$$

The function $k(y)$ is therefore a positive constant equals π^2/b^2 .

The singular neutral solution obeys:

$$\phi_{yy} + (\frac{\pi^2}{b^2} - \alpha^2)\phi = 0 \quad \text{with} \quad \phi(0) = \phi(a) = 0.$$

The eigenvalues and eigenfunctions are:

$$(9) \quad \begin{cases} \alpha_s = \pi^2 (\frac{1}{b^2} - \frac{n^2}{a^2}) \text{ with } n = 1, 2, \dots, \text{ Integral part of } a/b \\ \phi_s = \sin \frac{n\pi y}{a} . \end{cases}$$

If b/a is larger than unity, then no real eigenvalues exist but the flow can be shown to be stable (Howard, Drazin, 1964). If b/a is smaller than unity then a necessary and sufficient condition for instability (i.e., a positive c_i) is that:

$$\alpha^2 \leq \alpha_M^2 \quad \text{where} \quad \alpha_M^2 = \pi^2 (\frac{1}{b^2} - \frac{1}{a^2}).$$

The marginal scale (α_M^{-1}) predicted by the theory is of the order of the scale of the mean flow if b/a is much less than unity. If b/a is

order 1, the marginal scale tends to infinity and the flow will therefore be stable to all perturbations. This latter case seems to be relevant to the experiment judging by the aspect of figure 4-6. Lin's formula (6) can then be used to estimate the damping rate of the perturbations. In the above example, such a calculation was done for the case $a = b$.

$$\text{Let } \frac{dc}{d\alpha^2} = \frac{1}{A + iB}$$

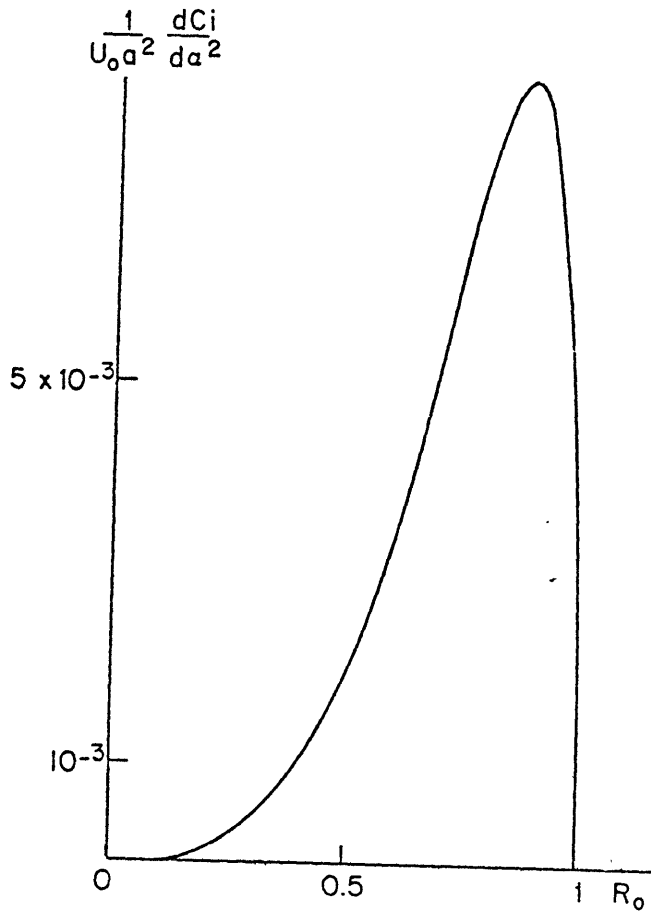
Evaluation of the integrals in (6) using eigenfunctions (9) gave:

$$A = \frac{-4\pi}{a^2 U_0} \left\{ 1 + \frac{R_0 \pi}{2} + (1 - R_0^2)^{-\frac{1}{2}} \log \left| \frac{1 + (1 - R_0^2)^{\frac{1}{2}}}{1 - (1 - R_0^2)^{\frac{1}{2}}} \right| - (1 - R_0^2)^{\frac{1}{2}} \log \left| \frac{-1 + (1 - R_0^2)^{\frac{1}{2}}}{R_0} \right| \right\}$$

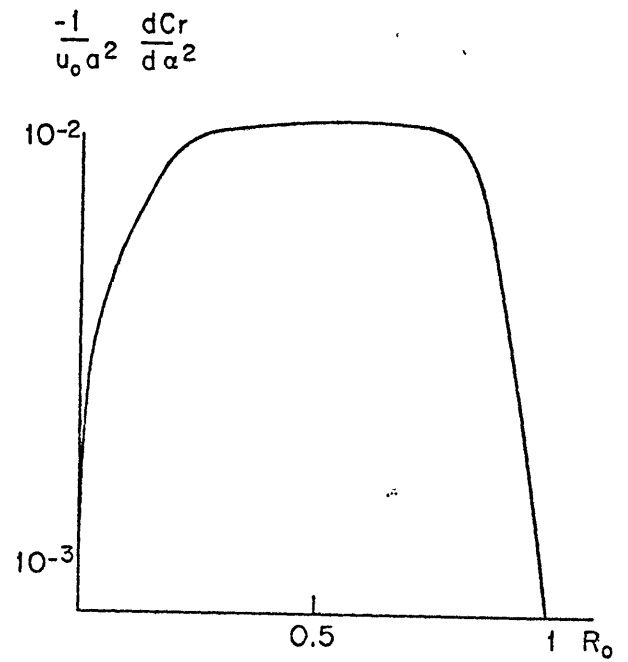
$$B = \frac{4\pi^2}{a^2 U_0} \left\{ \frac{R_0^2}{(1 - R_0^2)^{\frac{1}{2}}} \right\}.$$

Because B is always positive and the marginal neutral scale infinite the flow is stable. The scaled values of $\frac{dci}{d\alpha^2}$ and $\frac{dc_r}{d\alpha^2}$ are plotted on figure 4.15 as a function of R_0 . The contrast between the shapes of the real and imaginary part of $\frac{dc}{d\alpha^2}$ is prominent. Significant damping rates occur in the vicinity of $R_0 = 0.88$. This value corresponds to critical points situated at $a/2.92$ and $a/1.52$ respectively, symmetrical and close to the point of maximum velocity as in the experiments. The corresponding maximum values of the damping rate αc_i that one gets using experimental parameters can be estimated as:

$$\alpha c_i = 8.5 \times 10^{-3} \cdot U_0 (\alpha a)^2 \cdot \alpha$$



.a.



.b.

4-15 The perturbation phase velocity as a function of

$$R_0 = \frac{\beta b^2}{U_0 \pi^2}$$

(a) imaginary part

(b) real part.

with $U_0 = 2$ cm/s, $\alpha a = 12$ and $\alpha = \frac{12}{30}$ one obtains:

$$\alpha C_i = 0.97 \text{ rad/s.}$$

This rough estimate falls well within the order of magnitude of the experimental damping rate.

The general statements that we made about the behavior of the function $k(y)$ for the case of a westward jet suggest that the conclusions drawn above for the sin profile remain valid for other potentially unstable westward flow as long as they do not include "intense" regions of negative curvature. In these cases (when $k(y)$ is positive), Lin's formula (6) which indicates that scales shorter (respectively longer) than neutral are damped (respectively unstable) agrees with the general spectral tendency for the total flow (eddies + mean) to evolve to larger scales.

II. The Rossby wave critical layer

Because the experimental simulation of the interaction of a Rossby wave and an externally forced mean zonal flow turned out to be straightforward, interest in the subject developed quickly in view of its geophysical importance. The extensive literature available today reveals that it is only recently that the physical role of the region, where the wave phase speed matches the velocity of the mean flow, has been recognised. Excluding these regions, Eliassen and Palm (1960) demonstrated in the internal gravity wave context that the Reynolds stress is independent of height. Somewhat later, Booker and Bretherton (1967) considering initial value problem extended the analysis by showing that most of the interaction between the wave and mean flow occurs at the critical level where the gradient of the Reynolds stress is large. For large Richardson numbers the direction of the energy and momentum transfer is from the wave to the mean flow. Using these ideas, a successful simulation of the atmospheric quasibiennial oscillation was done by Lindzen and Holton (1968). Dickinson (1970) carried out an analytical initial value problem of forced Rossby waves in a shear flow. He shows that the zonal perturbation of the wind never settles down to a steady value at the critical level but diverges logarithmically in time. The eddy momentum transport grows initially in the same way on either side of the critical layer, then goes back slowly to zero beyond the critical level, suggesting a momentum transfer in the ever thinning layer. Classically the singularity that occurs in the steady state at the critical level has been dealt with by including dissipation. This method smears out the Reynolds stress discontinuity over a finite viscous layer of order $(\frac{\nu}{U'k})^{1/3}$, U' being the mean shear at the critical level, and k the wavenumber of the pertur-

bation. An alternative approach was developed by Benney and Bergeron (1969) who considered the effect of the non-linear terms on the steady solution at the critical level. If u is a measure of the eddy velocity, the layer over which non-linear terms become important is order $(u/U'k)^{1/2}$. Asymptotic matching on both sides of this layer reveals that no jump in the momentum transport exists around the critical level. The important parameter determining which of the frictional or finite amplitude effects dominates is therefore $\nu^{1/3} \cdot u^{-1/2} \cdot (U'k)^{-1/6}$. Dickinson's linear analysis was extended by Béland's (1976) numerical analysis. Carrying out numerical integration of the weakly non-linear, inviscid vorticity equation, he finds a tendency for the critical layer thickness to equilibrate at the above length scale. At the same time, the jump in the Reynolds stress across the CL is reduced strongly. Obviously such numerical studies are only tendency calculations. With increasing time, more and more of the fine structure produced at the critical layer becomes unresolvable. As pointed out earlier a laboratory model is free of all these limitations and it offers a unique opportunity to discover what is the steady state of the interactions and its dependence upon the strength of the wave. Before presenting the experiments, it is wished to present the results of a new time dependent linear theory in view of the difficulty of interpretation of past analytical solutions. In particular, one wants to relate the possible absorption of wave energy at a critical level with the resulting momentum transfer. Moreover the model has zonal boundaries and is definitely new in that respect.

A. Linear theory of the Rossby wave-zonal flow interaction

Consider first the interaction described in the framework of ray theory. A slowly varying wave packet is allowed to propagate in a zonal shear flow, the scale of which is much larger than a representative wavelength of the wave packet. Under this formalism, the wave energy moves along ray tube, envelopes of the absolute group velocity, and the amplitude variation along the ray is found from the conservation of wave action. For a Rossby wave with phase $(kx + \ell_y - \omega t)$, the dispersion relation can be written:

$$\omega_a = \omega_r + k \cdot U \quad \text{where} \quad \omega_r = \frac{-\beta k}{k^2 + \ell^2}.$$

Let us consider the simple linear shear flow $U = -\alpha y$ and let the waves start from $y = 0$ at $t = 0$ with a northward component of group velocity. For simplicity of exposition choose $k_0/\ell_0 \ll 1$.

Following a wave packet at the absolute group velocity, the absolute frequency and the zonal wavenumber are conserved. However because the wavecrests rotate under the action of the mean shear, the meridional wavenumber increases linearly with time. Allowing for this, the ray equations can be solved explicitly to yield:

$$x = \frac{-\beta t}{\ell_0^2}$$

$$y = y_c \left[1 - \frac{\ell_0^2}{(\ell_0 + \alpha k t)^2} \right]$$

where $y_c = \frac{\beta}{\alpha \ell_0^2}$ is the point at which the frequency relative to the mean flow vanishes. A wavepacket will thus never reach the critical level as the rays asymptote at y_c . Because total wave action is conserved, the total wave energy as measured by an observer moving with the mean flow

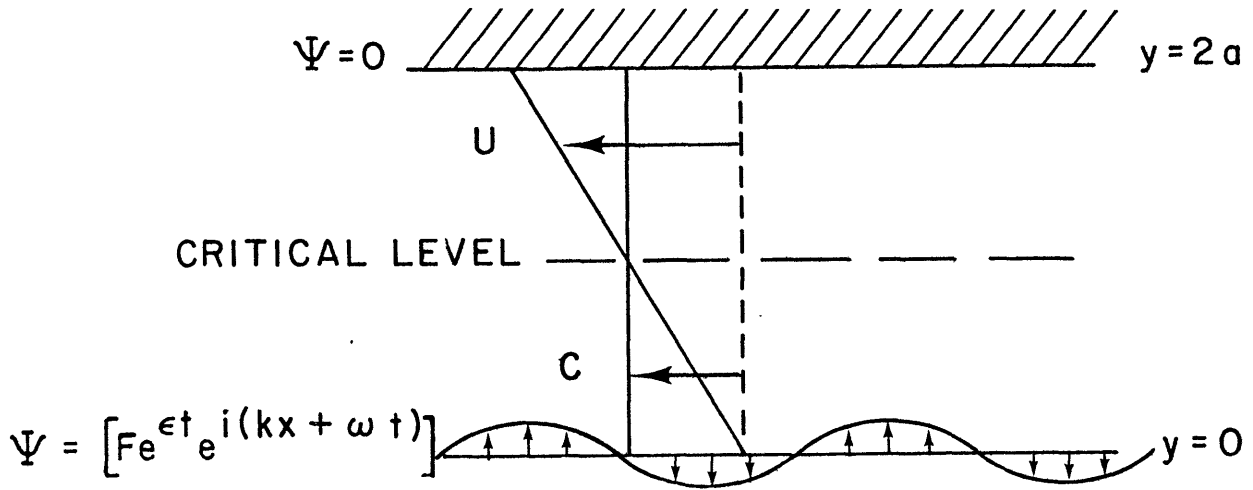
goes to 0 with ω_r as the critical level is approached. On the other hand, because the rays bunch together as time goes on, the local energy density increases linearly with time. The total wave energy is thus neither transmitted nor reflected at the critical level. Since it decreases with time, one might say that the wave energy is effectively absorbed at the critical level. It is difficult to say anything precise about the wave momentum in this framework. Moreover the WKB approximation upon which the ray theory is grounded ceases to be valid as the packet approaches y_c . Indeed, one may show that the relative change of the meridional wavenumber over a wavelength increases linearly with time.

To investigate the questions about the wave momentum transfer the following model is considered.

A linear westward shear flow is constrained between two zonal boundaries on a beta plane. The waves are forced at the southern boundary by the distribution of sources and sinks at the wall. The geometry is shown in figure 4-16. Consideration of a slowly switched-on problem will remove the singularity at the critical level. The time scale of the switch-on is assumed to be the longest scale of the problem, and the linear solutions derived in the following are valid for times smaller than this forcing time scale. The critical level is kept "fixed" at the center of the channel of width $2a$, so that:

$$c + U(y) = U \left(1 - \frac{y}{a}\right).$$

The forcing is introduced through the boundary condition at $y = 0$ where the meridional velocity is imposed as $(F \cdot e^{\epsilon t} \cdot e^{i(kx + \omega t)})$. Postulating a solution of the form $\psi = [\phi(y) e^{\epsilon t} e^{i(kx + \omega t)}]$, and



4-16 The geometry of the critical layer problem.

scaling y by the length a , yields the following two point boundary value problem:

$$\begin{aligned} \phi_{YY} - \left(\frac{R^{-1}}{y-1+i\delta} + \mu^2 \right) \phi &= 0 \\ (10) \quad \phi(2) &= 0 \\ \phi(0) &= F \end{aligned}$$

with the following definitions: $\delta = \epsilon/\omega$, $\mu = ka$, $R = U/\beta a^2$, $M = \mu^2 R = \frac{Uk^2}{\beta}$.

The parameter δ , the ratio of the wave period to the forcing time scale, is assumed to be small. Its main purpose is to prevent the differential equation (10) from becoming singular at the critical level $y = 1$.

The solutions to (10) will now be presented when the parameter M is much smaller and much greater than unity.

$$(a) \quad M \ll 1, \quad R \ll 1$$

This regime implies short waves with almost horizontal wave crests. In a sense it contains the WKB solution valid far from the critical level that we just discussed. (10) can now be approximated throughout the channel by:

$$(11) \quad \phi_{YY} - \frac{R^{-1}}{(y-1+i\delta)} \phi = 0$$

By changing variables to $z = 2R^{-\frac{1}{2}} (y-1+i\delta)^{\frac{1}{2}}$ and $\phi = z\psi(z)$ one obtains the following equation for ψ :

$$z^2 \psi_{zz} + z\psi_z - (1+z^2)\psi = 0$$

This differential equation is satisfied by modified Bessel functions $I_1(z)$ and $K_1(z)$. The solution to (11) is therefore:

$$\phi = z(AI_1 + BK_1)$$

The constants A and B are found by using the boundary conditions. The parameter $\alpha = 2R^{-\frac{1}{2}}$ being large, the variable z is also large near the walls and in this region one can expand the Bessel function for large arguments. The correct determination of z must be used according to whether the regions of interest are situated above or below the critical level:

$$\text{when } y - 1 < 0 \text{ and } \frac{|y-1|}{\delta} \gg 1, z = 2R^{-\frac{1}{2}} e^{i\pi/2} |y-1|^{\frac{1}{2}}$$

$$\text{when } y - 1 > 0 \text{ and } \frac{|y-1|}{\delta} \gg 1, z = 2R^{-\frac{1}{2}} |y-1|^{\frac{1}{2}}$$

On that basis, one expects to find wavelike solutions below the CL and evanescent solutions above. The critical point in the Rossby wave context has the nature of both a singular and a turning point. This is an essential difference from the internal gravity case which possesses the second order pole $((U - c)^{-2})$ rather than $(U - c)^{-1}$. Oscillating internal gravity waves may therefore be sustained "above" the CL (their amplitude is non negligible if the Richardson number is small).

The determination of A and B yields the solution:

$$(12) \quad \phi = \frac{F e^{i(\pi/4 + \zeta)}}{[\alpha\pi(\cosh 2\alpha - \cos 2\alpha)]^{\frac{1}{2}}} z [e^{\alpha} K_1(z) - \pi e^{-\alpha} I_1(z)]$$

$$\text{where } \tan \zeta = - \frac{\tanh \alpha}{\tan \alpha}.$$

Using asymptotic expansions, this solution may be simplified in

in various regions

$$*|y - 1| \gg R$$

South of the critical layer ($y < 1$) the solution may be approximated by:

$$(13) \phi = \frac{F e^{i(\zeta + \pi/2)}}{\sqrt{2(\cosh 2\alpha - \cos 2\alpha)}} \frac{1}{2} |y - 1|^{\frac{1}{2}} \left[e^{\alpha} e^{i\theta - \epsilon \left(t - \frac{\alpha}{2\omega} |y - 1|^{-\frac{1}{2}}\right)} - e^{-\alpha} e^{i\theta + \epsilon \left(t + \frac{\alpha}{2\omega} |y - 1|^{-\frac{1}{2}}\right)} \right]$$

where $\theta^\pm = kx + \omega t \pm \alpha |y - 1|^{\frac{1}{2}}$.

In this large region, the solution (13) is the sum of two waves. The first term represents an incident wave whose amplitude modulation moves north although the phase propagates southward. The second term represents a reflected wave whose amplitude travels southward and phase northward.

The ratio of the incident to reflected amplitude is given by:

$$\frac{A_i}{A_r} = e^{4R^{-\frac{1}{2}}}$$

This quantity is large in this limit and goes to ∞ as the width of the channel. (The reflected wave must disappear in an infinite medium to satisfy the radiation condition.) In a bounded fluid, however, part of the wave energy sent up north is reflected back at the critical level.

North of the critical layer the solution is:

$$(14) \phi = \mathcal{R} \left\{ \frac{F\sqrt{2} e^{\epsilon t} e^{i(kx + \omega t)}}{(\cosh 2\alpha - \cos 2\alpha)^{1/2}} e^{i(\zeta + \pi/4)} |y - 1|^{1/4} \sinh \alpha (1 - |y - 1|^{1/2}) \right\}$$

There is no propagation in the meridional direction other than slowly moving transients. However some kinetic energy is able to tunnel through the critical layer. To determine the acceleration regions of the mean flow (if any), the wave Reynolds stress \overline{uv} needs to be calculated. South of the CL the incident wave is associated with a negative \overline{uv} correlation while the smaller reflected wave has a positive correlation. This agrees with the Rossby wave dispersion relation. On the other hand it is the divergence of the Reynolds stress which indicates if there is any momentum transfer between the wave and the mean flow. In solution (13), this mean vortex force (so called by Lighthill) vanishes to $O(\delta)$. Both the incident and reflected waves conserve their momentum, but incident wave energy decreases as the CL is approached while reflected energy increases with distance away from the CL. North of the CL, both the wave stresses and the vortex force vanish to $O(\delta)$. These last results indicate that the definition of mean wave zonal momentum as wave action times zonal wavenumber in the earlier ray theory description would have correctly predicted conservation of wave momentum in the WKB regions.

$$\delta \ll |y - 1| \ll R$$

In this narrow layer, the Bessel functions in (12) are expanded in series for small arguments.

South of the CL, the solution is:

$$\phi = \mathcal{R} \left\{ A(x, t) \left\{ e^{\alpha} \left[1 - \frac{\alpha^2}{4} |1 - y| (\log \alpha^2 |1 - y| + i\pi) \right] + \pi e^{-\alpha} \frac{\alpha^2}{2} |1 - y| \right\} \right\}$$

$$\text{where } A = \frac{F e^{\epsilon t} e^{i(kx + \omega t)} e^{i(\pi/4 + \zeta)}}{(\alpha\pi)^{1/2} (\cosh 2\alpha - \cos \alpha)^{1/2}}$$

and north of the CL, one obtains:

$$\phi = \mathcal{R}\{A(x,t) \{e^{\alpha} [1 + \frac{\alpha^2}{4} |1 - y| \log \alpha^2 |1 - y|] - \pi e^{-\alpha} \frac{\alpha^2}{2} |1 - y|\}\}$$

The main formal difference between the two expressions comes from the introduction of $i\pi$ in the former. The Reynolds stress, scaled by $F^2 e^{2\epsilon t}$, turns out to be:

$$\text{for } y - 1 < 0, \overline{uv} = -\frac{k\alpha e^{2\alpha}}{2(\cosh 2\alpha - \cos \alpha)} [1 + \frac{\alpha^2}{4} (1 - y)]$$

$$\text{for } y - 1 > 0, \overline{uv} = 0.$$

No anisotropy and momentum transfer is found north of the CL, however southward, a negative \overline{uv} is again present. Furthermore the divergence of the Reynolds stress is

$$\frac{d\overline{uv}}{dy} = \frac{+k\alpha^3 e^{2\alpha}}{8(\cosh 2\alpha - \cos \alpha)}.$$

The vortex force is thus negative and accelerating the mean flow in that narrow layer. For large α , the impulse of momentum flux integrated meridionally is of order $kR^{-3/2} \cdot aR$ or $\frac{M^2}{R}$. The final form for \overline{uv} below the critical layer shows that the reflected wave does not play any role in the momentum transfer. Formally there is a third inner layer of order δ where the solution can be expanded. One may show that the momentum transfer is in the same direction as above. However because $\frac{\delta}{R}$

~~is much smaller than unity, that layer does not contribute much to the~~
total impulse of momentum flux. In contrast with the above results, the following parameter regime will now be considered:

$$(b) M \ll 1, R \gg 1.$$

The same differential equation (11) is valid throughout the channel. Expansion of the Bessel functions for small arguments is needed to satisfy the boundary conditions. The detailed solutions will not be reproduced here but the conclusions will be discussed. In the interior region away from the inner layer of order δ , the Reynolds stresses are:

$$y - 1 < 0, |y - 1| \gg \delta, \overline{uv} = \frac{8k}{\pi\alpha^2} (3 - 2y)$$

$$y - 1 > 0, |y - 1| \gg \delta, \overline{uv} = 0.$$

Below the CL the Reynolds stress is positive and the mean vortex force "decelerates" the mean westward flow. The order of magnitude of the momentum flux impulse is $(RM)^{\frac{1}{2}}$. The waves are now able to extract momentum from the mean flow. This is not surprising: the limit small M and large R implies a very small value for the parameter $\mu = ka$. The waves have a wavelength much larger than the channel width which is also the scale of the mean flow. Therefore the direction of the momentum transfer agrees with general requirements deduced from energy and enstrophy conservations: namely that the flow of energy must be toward the large scale structure either waves or mean flow.

$$(c) M \gg 1, R \ll 1$$

This last case may also be handled simply. It corresponds physically to short waves with vertical wavecrests. When $|y - 1|$ is smaller than

M^{-1} the solution will satisfy the differential equation (11). However in the interior where $|y - 1|$ is much larger than M^{-1} , the solution has to be found from the full equation (10). Fortunately the WKB solution may be used with good accuracy in that region.

$$\text{if } |y - 1| \gg M^{-1}: \phi = Q^{-1/4} [A' e^{-\int Q^{1/2} dy} + B' e^{+\int Q^{1/2} dy}]$$

$$\text{where } Q = \mu^2 + \frac{R^{-1}}{y - 1 + i\delta}$$

$$\text{if } |y - 1| \ll M^{-1}: \phi = z[A I_1(z) + BK_1(z)]$$

A' and B' are found by using the boundary conditions. A and B are calculated by asymptotic matching between the two above solutions. The oscillating solutions are now trapped below the CL in a narrow region between $y = 1$ and $y = 1 - M^{-1}$ which is a pseudo turning point. In this oscillating region the solution has basically the same form as (12) in (a), and contains most of the same physics. When $R \ll |y - 1| < M^{-1}$, an incident and a reflected wave may be identified transporting energy respectively toward and away from the critical layer. The ratio of their amplitudes is now:

$$\frac{A_i}{A_r} = e^{4ka}, \quad \text{a large value in this limit.}$$

The wave momentum is again conserved in that layer. In the region $\delta \ll |y - 1| \ll R$ most of the momentum transfer occurs as in (a). The Reynolds stress is negative, and the vortex force is such as to accelerate the mean flow. The meridionally integrated impulse of momentum flux

is of order $\frac{M}{R}$.

In light of these 3 cases, one realises that the sign of the vortex force is sensitive to the parameter R which compares the scale of the wave to the channel width. Relating to earlier infinite beta plane studies, one realises that new physics may arise in the bounded case for long wavelength excitation: the mean flow is now decelerated in a broad region. On the contrary, when the wavelength is small, the flow is accelerated in a narrow region around the critical level. The critical layer appears to play the role of a weakly reflecting barrier for incident wave energy rather than purely absorbing as in an infinite medium. The reflected wave does not appear to play any role in the momentum transfer. The amplitude of the vortex force is sensitive to the parameter M in this regime: for the same short wavelength, it is larger for waves whose crests are oriented more meridionally at the source.

A side benefit from the formulation of this transient theory is that the same solutions may be used to treat the interaction of linear steadily forced waves and mean flows in presence of Ekman dissipation. The earlier parameter ϵ^{-1} must be interpreted as the Ekman spin down time. If the forcing is specified as $[F e^{i(kx + \omega t)}]$ at the southern boundary, all the earlier solutions must be multiplied by $e^{-\epsilon t}$. In particular this identification allows one to predict the momentum transfer in the linear steady regime. This is relevant to the laboratory experiment designed to reveal the wave momentum absorption by the mean flow in both the transient and steady regime in which the important dissipative mechanism is caused by Ekman friction.

B. The laboratory experiment

The wave generating mechanism is the same as described in Part Three, paragraph I. The mean flow is externally driven by a source placed at the center of the basin. Fluid is expelled through a diffuser of a radius of about 3 cm to avoid jetting effects. The corresponding sinks are distributed uniformly along the circumference of the container. Because the mass flux involved in the generation of the mean flow is much smaller than the mass flux running through the wave driving, the influence of the mean steady sinks upon the "wavelike" sources and sinks is negligible. Moreover, the two driving mechanisms were built to operate independently with the only common paths for fluid parcels in the two systems exclusively in the interior of the basin. With a steady source at the center, an "axisymmetric" solution has to satisfy the following vorticity equation in the interior:

$$R\nabla^2\psi = -f \frac{w_o}{H} \frac{\delta(r)}{r}$$

The source has been modelled by a δ -function at the origin. Since the nonlinear and beta terms vanish identically, the solution is simply:

$$\psi = -\frac{1}{2\pi} \frac{f}{RH} w_o \text{Log } r$$

which yields a $1/r$ profile for the zonal westward interior velocity, the fluid being expelled radially toward the sinks in the lower Ekman layer. Because of the existence of dynamical and physical constraints, the parameter range of the critical layer problem that one can explore is small. The preceding theory (and many others in the internal wave context)

suggested that it would be particularly interesting to consider waves much shorter than the scale of the mean flow in order to see the gradual motion of the "acceleration zone" toward the wave source. This turned out to be impossible on account of Ekman friction lowering too much the Q of the resonator for short waves. The same zonal mode number of 12 was therefore kept. A complicating factor is the existence of critical latitudes induced by the variation of beta. One wants these critical latitudes to be situated beyond the critical level in order to avoid interference. Remembering that this necessitates small driving frequencies and hence smaller Q , it limits singularly the possible positions of the critical level. It could not be situated more than one wavelength away from the wave source. This gave the following typical figures for the parameters R and M introduced earlier,

$$R = \frac{U}{\beta a^2} = 2 \times 10^{-3}, \quad M = \frac{U}{\beta} k^2 = 0.3$$

Both the proximity of the critical level from the wave source and the order one value for M prevents a detailed comparison of the simple theory outlined above with the experiments but both of them seem to be interesting in their own right.

The important parameter in determining whether nonlinear terms are important far from the critical level is simply $S = \frac{u' k^2}{\beta}$ where u' is the eddy rms speed. Near the critical layer, however, Benney and Bergeron have shown that linear terms will be large if the ratio of the thickness of nonlinear critical layer to the viscous critical layer thickness is large. If the scales of motion are such that dissipation is dominated by an Ekman friction mechanism, the relevant vorticity equation

for the waves is:

$$(\bar{U} - c)\nabla^2\psi_x + J(\psi, \nabla^2\psi) + (\beta - \bar{U}_{yy})\psi_x = -\frac{\nabla^2\psi}{T}$$

Balancing the first and second terms of this equation at the critical level yields the thickness of the nonlinear critical layer:

$$\delta_n = \left(\frac{u'}{k \frac{\partial \bar{U}}{\partial y}} \right)^{1/2}$$

while balancing the first and the last gives the thickness of the viscous critical layer

$$\delta_v = (Tk \frac{\partial \bar{U}}{\partial y})^{-1}.$$

The important measure of the nonlinearity at the CL is therefore

$$\varepsilon = \frac{\delta_n}{\delta_v} = T(u'k \frac{\partial \bar{U}}{\partial y})^{1/2}.$$

Because of the difficulty of measuring accurately Reynolds stress when u'/\bar{U} is much smaller than unity, most of the experiments were carried out for values of ε which are order one, although S may be smaller than unity.

When the mean flow reaches a steady state, the wave driving is impulsively turned on. Streak photographs of the flow are taken at short intervals until the appearance of a steady state. The velocity data is then digitized in order to measure the mean flow, the Reynolds stress and the eddy kinetic energy at a given instant. Extensive zonal averaging reduced the relative error bars of these estimates below 4%. Because pressure time series

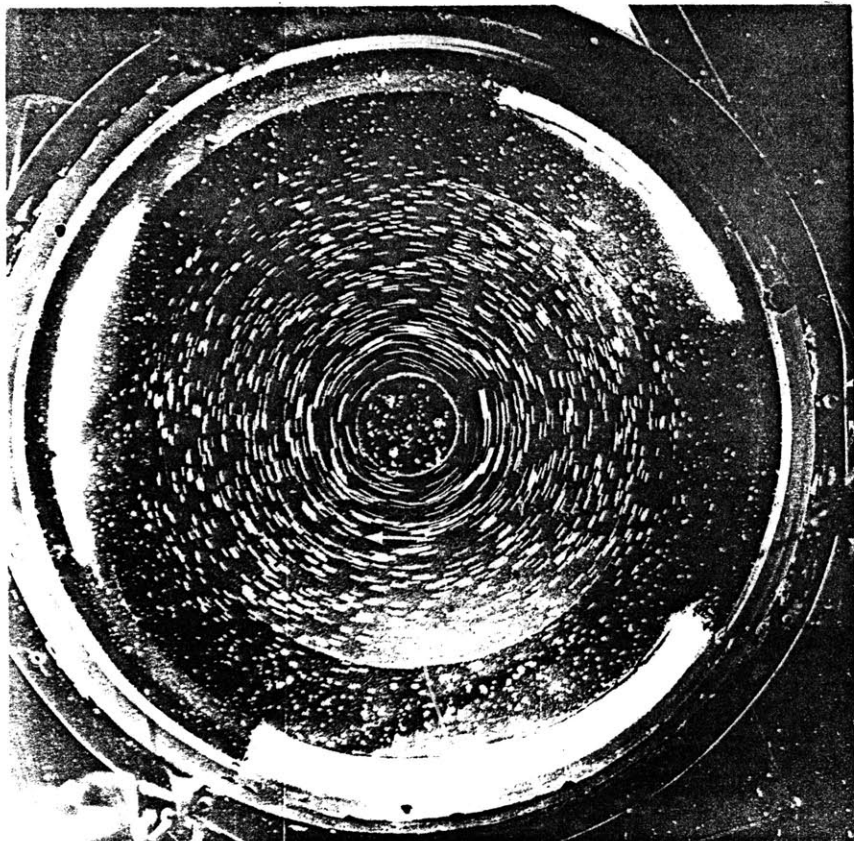
at a fixed point proved invaluable, other similar runs were made with two capacitance probes situated on either side of the CL. (Note that it is not possible to make simultaneous measurements of velocities and pressure because use of capacitance probes necessitates a clean free surface.) Although many runs were carried out for consistency, the essentials of the experiments may be unveiled in presenting only two runs. The parameter regime of these two runs is shown on table 4-17. Run 1 will be called a quasilinear run because S is small although δ_n and δ_v have same order of magnitude (about one fifth of a wavelength). Run 2 is a higher amplitude run, everything else being kept the same. The figures in table 4-17 indicate that the critical layer has definitely a nonlinear character.

Visual information about the steady state of the flow in Run 1 may be seen on figure 4-18. The tilt of the wave troughs needed to accelerate the mean flow is particularly apparent. The transient states of the mean flow are depicted on figure 4-19 (a). Because the transients generated by the impulsive switch-on covers a wide range of frequencies, the mean flow is accelerated everywhere and in particular well beyond the CL. As the steady state is reached, the mean flow beyond the CL has relaxed back to its original profile. The momentum absorption is thus confined between the CL and the wave source. The associated steady state Reynolds stress \overline{uv} shown in figure 4-19 (b), is large and negative between the wave source and the CL and vanishes smoothly away from the CL consistent with the mean flow accelerations. Pressure time series from the two probes which were separated by 12 cm, show that the signals remain fairly monochromatic both in the near forcing region and beyond the CL. This indicates that nonlinear terms

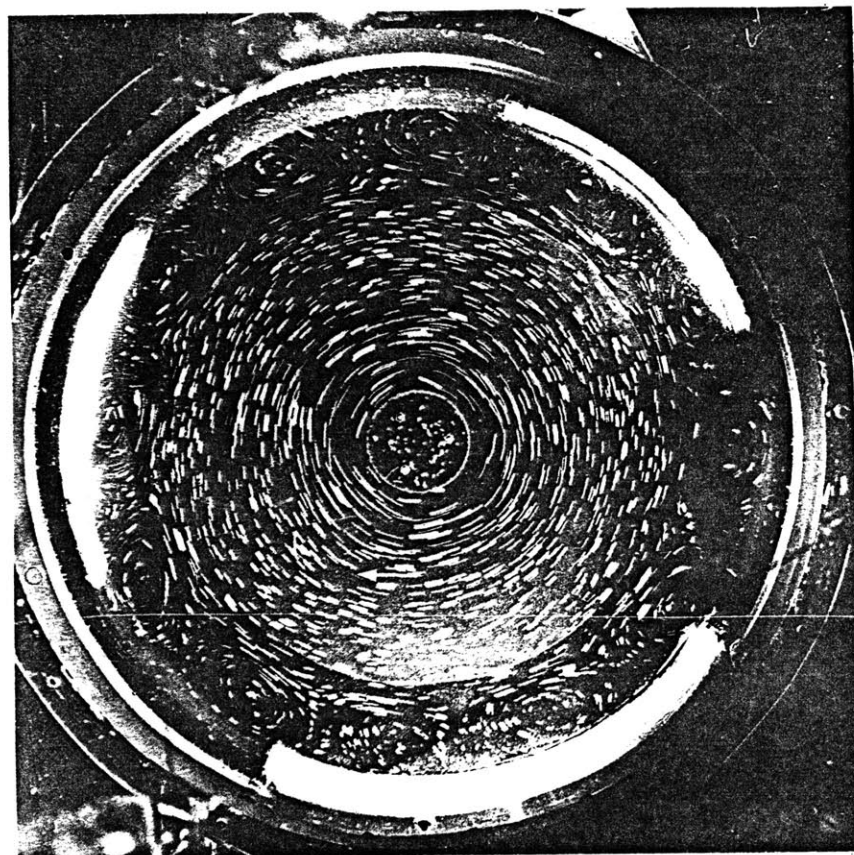
TABLE 4-17

Parameter regime for the critical layer experiments

	Ω (rad/s)	ω (rad/s)	Q_{mean} (cm ³ /s)	Q_{waves} (cm ³ /s)	$R = \frac{\bar{U}c}{\beta a^2}$	$M = \frac{\bar{U}k^2}{\beta}$	$S = \frac{u'k^2}{\beta}$	$\delta_n = \left(\frac{u'}{k \frac{\partial \bar{U}}{\partial y}} \right)^{1/2}$	$\delta_v = \left(\tau_k \frac{\partial \bar{U}}{\partial y} \right)^{-1}$	$\epsilon = \frac{\delta_n}{\delta_v}$
RUN 1	4.0	0.358	1.37	109	2.4×10^{-3}	0.98	0.11	1.6	1.32	1.21
RUN 2	4.0	0.358	1.37	333	2.4×10^{-3}	0.98	0.33	2.8	1.32	2.12

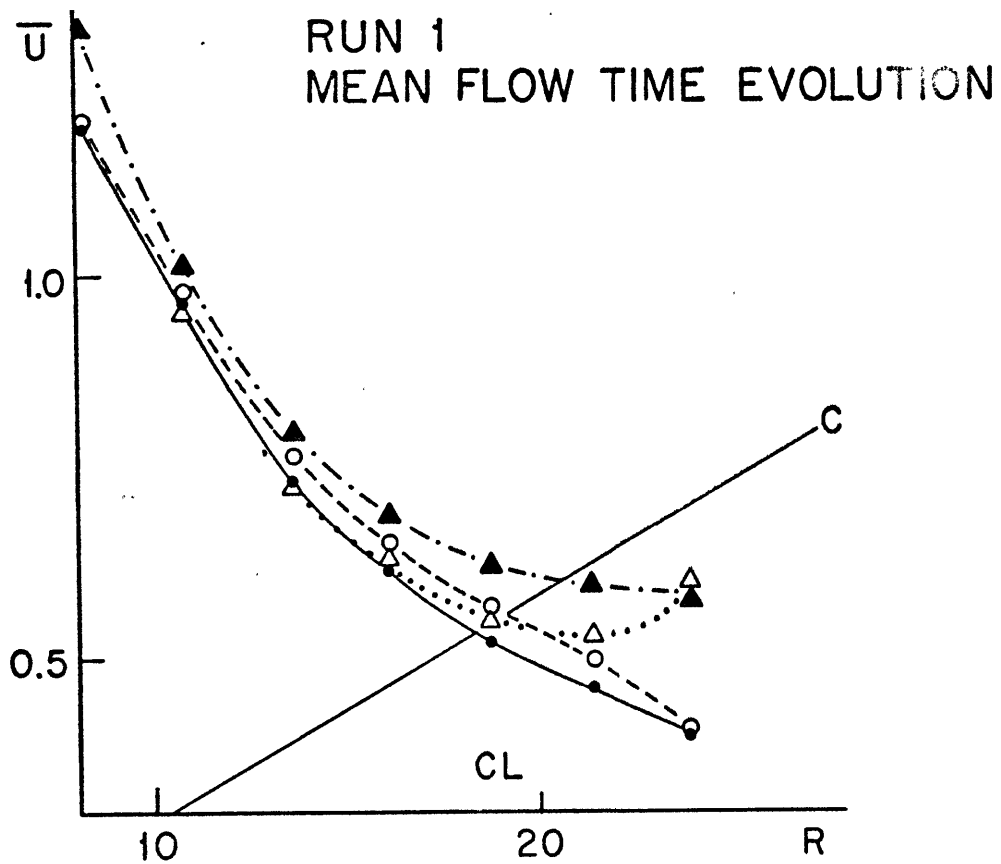


.a.



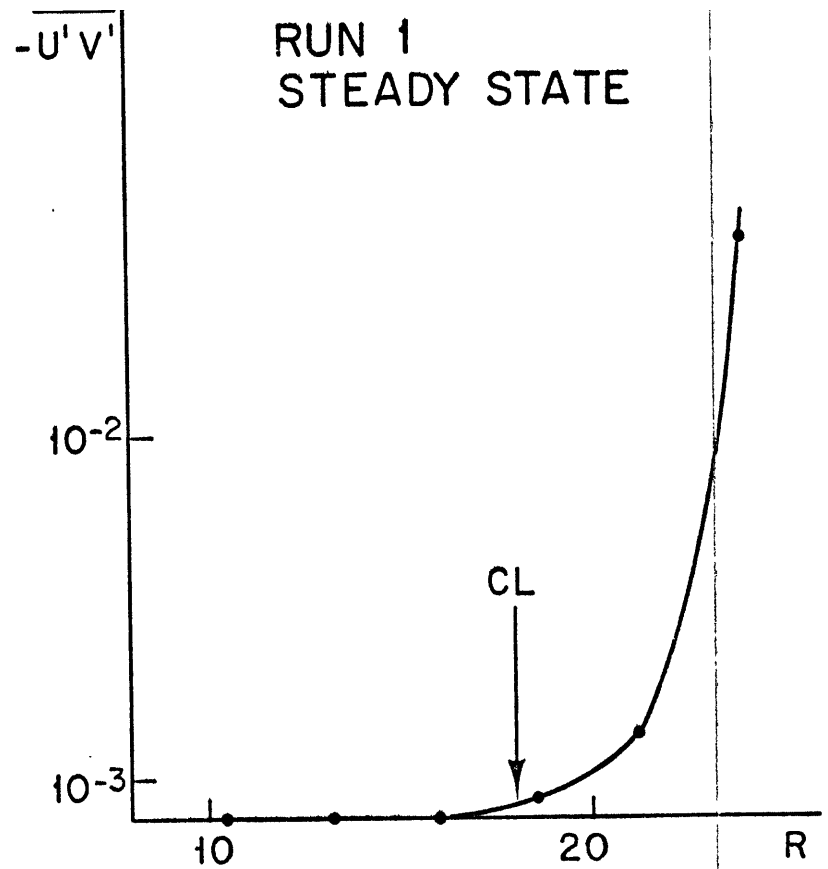
.b.

4-18 (a) The mean flow used in the critical layer experiments
(b) The steady state of run 1.



—●— MEAN FLOW
 ...△... #16
 --○-- # 2 -▲- # 4

-a-



-b-

4-19 Mean flow and Reynolds stress as calculated from run 1

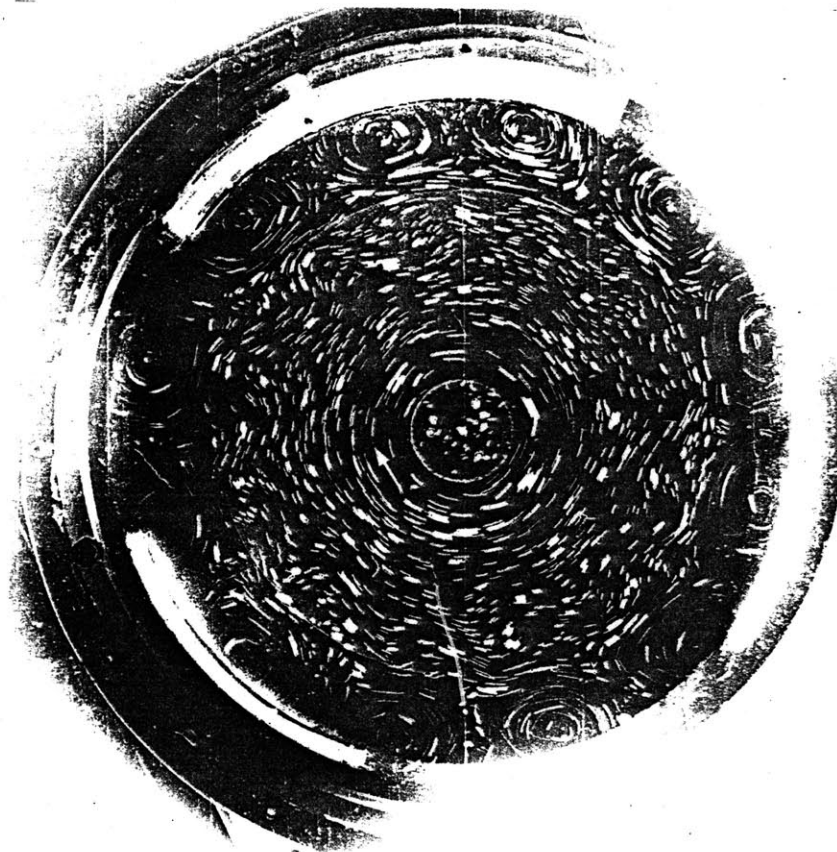
(a) transient and steady state of the zonal flow: curves #2, 4, and 16 correspond to photographs taken respectively at $T/5$, $T/2$ and $4T$, T being the Ekman spin-up time

(b) The steady state Reynolds stress (#16).

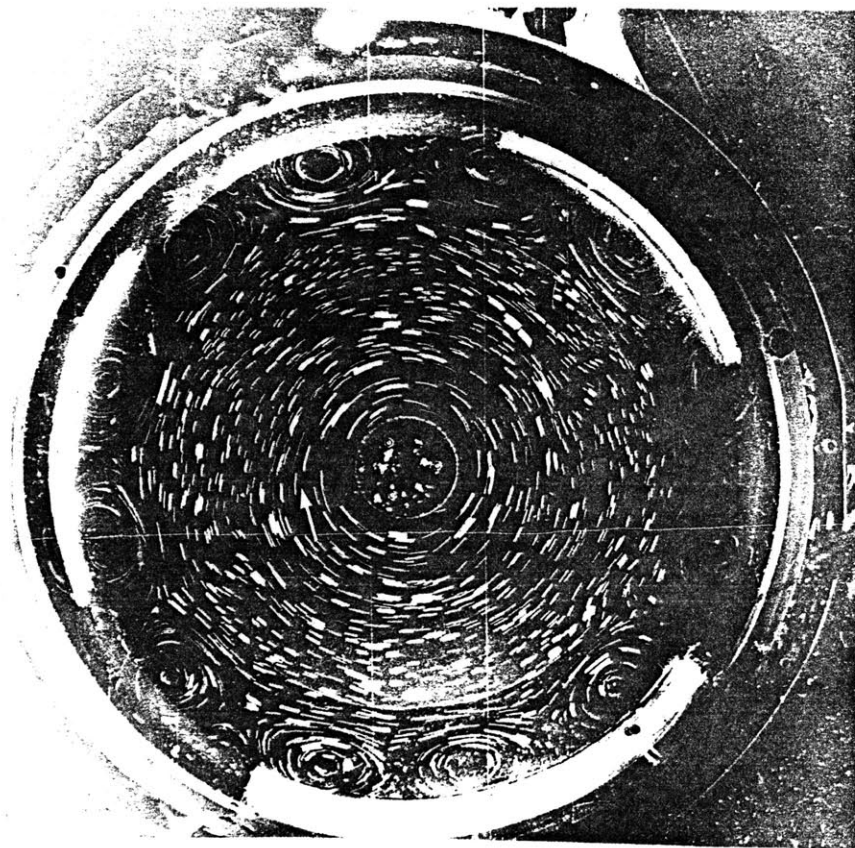
are probably not very important in this run, judging by the absence of harmonics. The eddy kinetic energy "beyond the CL" could be easily compared in presence or absence of the external mean flow. It was found in fact that the rms pressure dropped by about 30% when the mean flow was present. This appears to say that part of the wave energy has been effectively absorbed at the CL and used for conversion to the mean kinetic energy. The simple experiment suggests that the qualitative picture obtained from the linear theory remains of some value in this run. In the steady state the critical layer acts as a rigid wall for mean momentum transfer but allows some eddy kinetic energy to leak through the other side of the CL. In the transient stages, as the mean flow accelerates, the critical level moves toward the wave source but eventually returns close to its original position in the steady state. Note also that the shear of the mean current has been severely reduced.

As we said, Run 2 is much more nonlinear as the speeds of the waves and the mean flow are about of the same order of magnitude. The thickness of the nonlinear critical layer is about two times larger than the viscous thickness. The changes in the time evolution and the steady state of the mean flow are profound as witnessed by the photographs from figures 4-20.

In the initial transient stage, overreflection occurs as the mean flow structure is completely annihilated by the eddies, but then gradually the mean flow regains its strength to attain a steady state shown in figure 4-21 (a). The mean flow has been accelerated everywhere along the profile as wave momentum and energy are able to be transmitted much more easily through the critical layer region. The steady state Reynolds stresses and eddy kinetic energy are shown in figure 4-21 (b). Considerable mean momentum may now be transferred to the mean flow beyond the

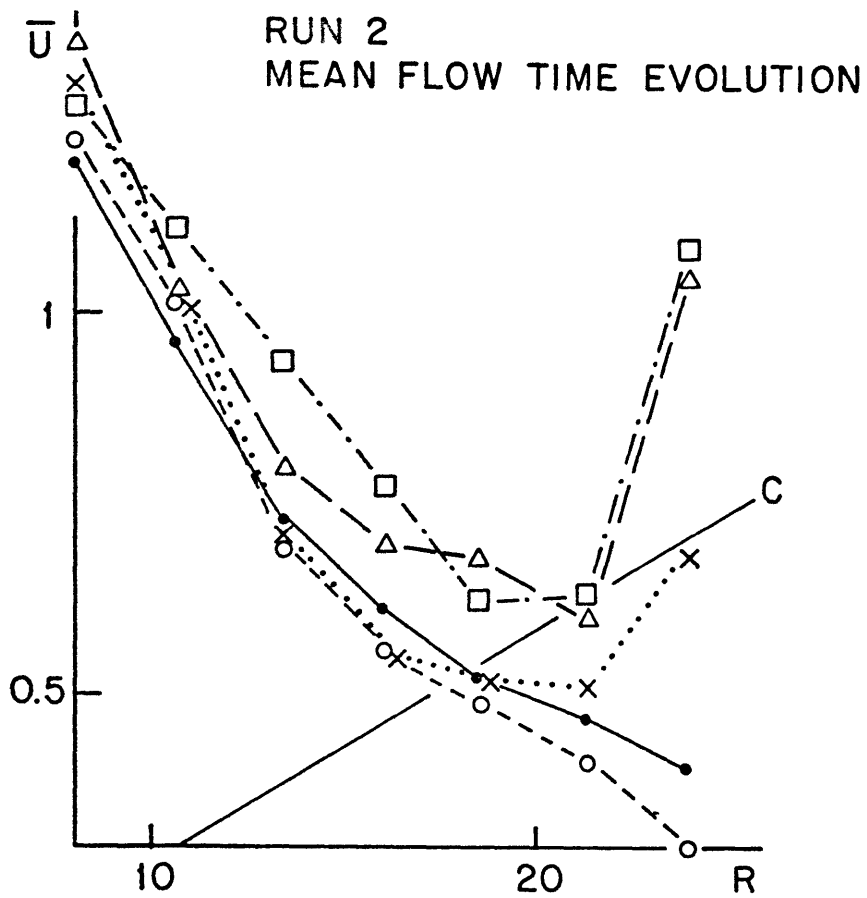


a.



b.

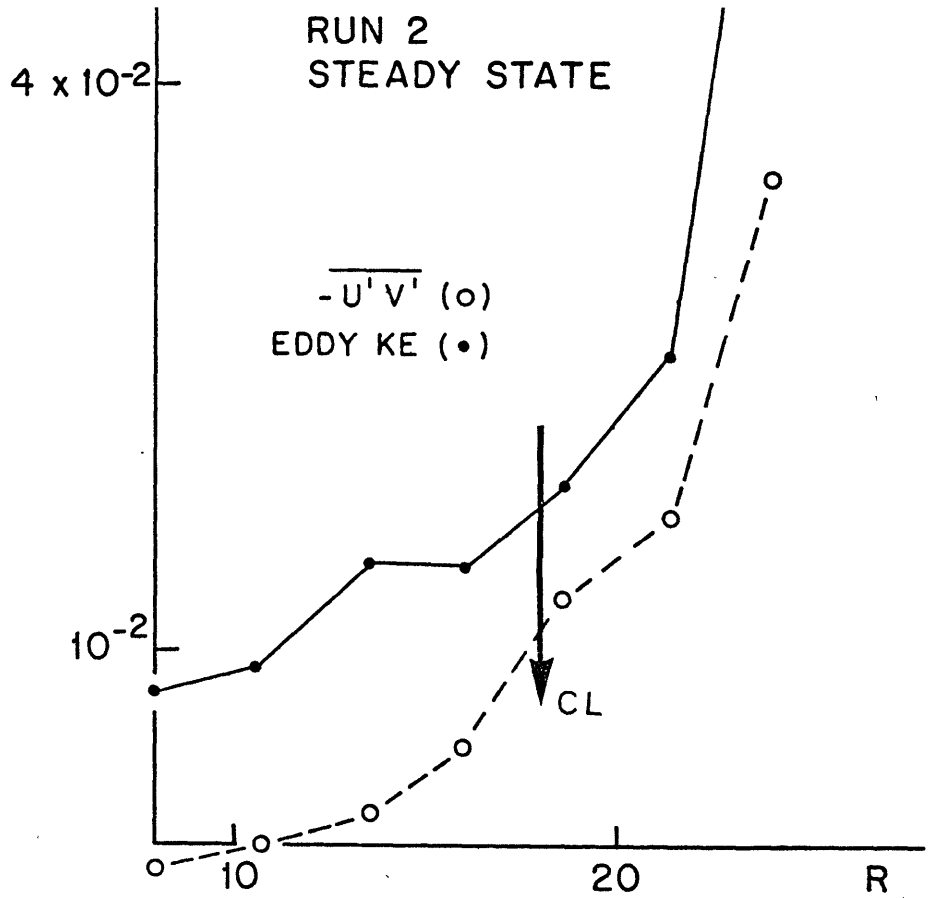
4-20 The transient (a) and steady state (b) of the non-linear run 2.



—●— MEAN FLOW
 - - - ○ # 1
 ···· x # 2
 - · - · - △ # 4
 - · - · - □ # 17

.a. 4-21 Averaged fields as calculated from run 2

(a) Mean zonal flow: curves #1, 2, 4 and 17 correspond to photographs taken respectively at $T/11$, $T/3.5$, $T/1.7$ and $5T$, T being the Ekman spin-up time.

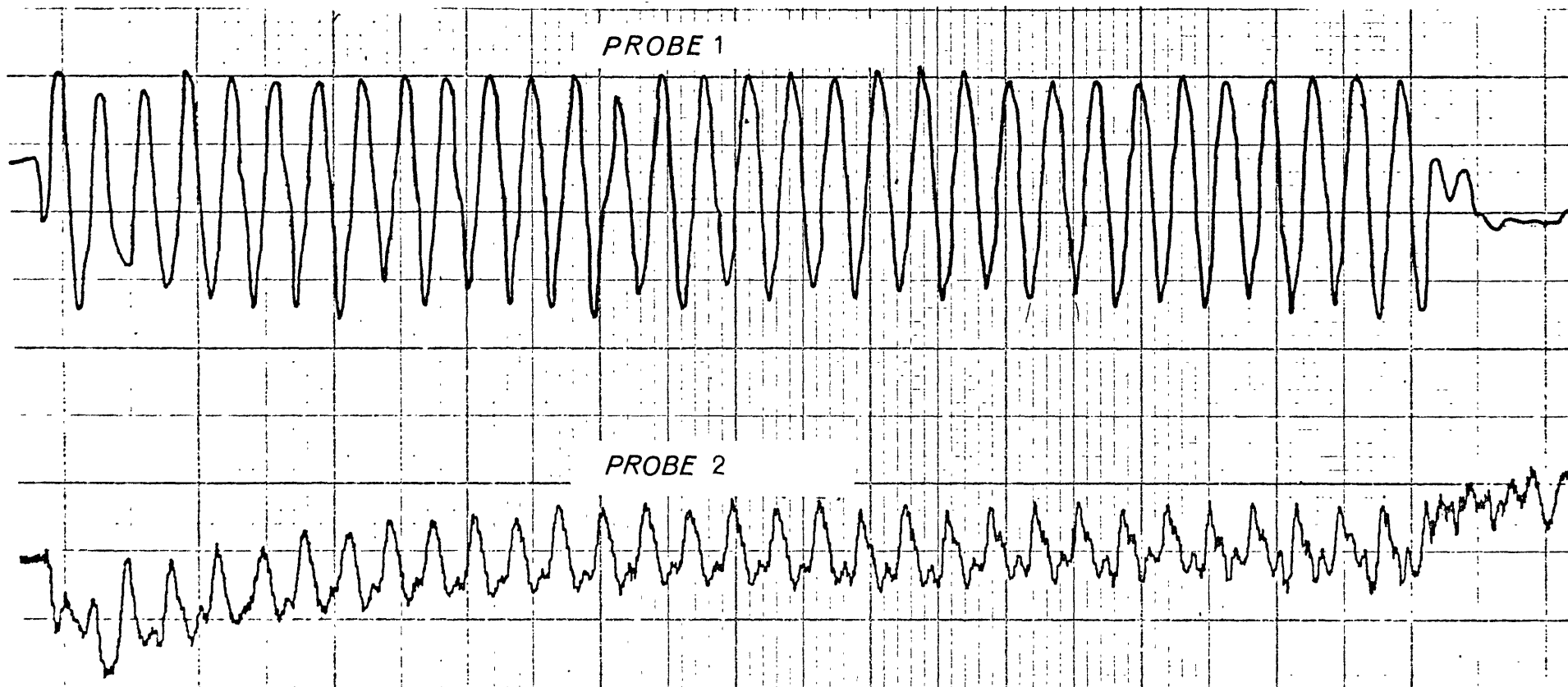


.b.

(b) Reynolds stress and eddy kinetic energy (#17)

critical level as indicated by the value of the eddy stresses. The weaker dependence of the Reynolds stresses upon the meridional scale as compared to Run 1, is also an indication of the larger width of the critical layer.

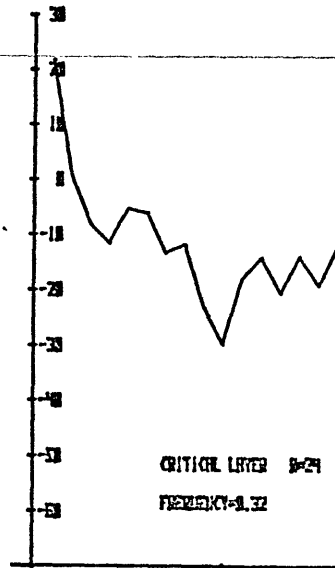
The two capacitance probes #1 and 2 were situated at a radius of 24 and 12 cm on each side of the critical level ($r = 18$ cm). The rms pressure time series showed a very interesting unsteady behavior at the interior position. This appears in figure 4-22 (a). Over a spin up time scale a lot of fine structure develops in the critical layer region. Spectra of the wave form were computed a short time after the switch-on and much later when a statistically steady state had been reached. They are shown on figure 4-22 (b). The spectral broadening as the steady state is reached is evident and reveals the difficulty of numerical studies in reproducing such fine effects. The time series at the interior probe show also that the rms amplitude are large initially but drop somewhat as the steady state is reached. This is consistent with observations of the mean kinetic energy, small initially but building up as time goes on, suggesting a transient transfer from the mean flow to the wave but reversing quickly to feed the mean flow in the steady state. Absorption of wave energy and momentum by the mean flow now occurs in a much broader region revealing an increasing transmission through the critical level. The presence of many harmonics in the steady state indicated by the turbulent aspect of the pressure time series supports the conclusions of Lin (1958) who predicted it in a study of nonlinear-viscous parallel flow problem.



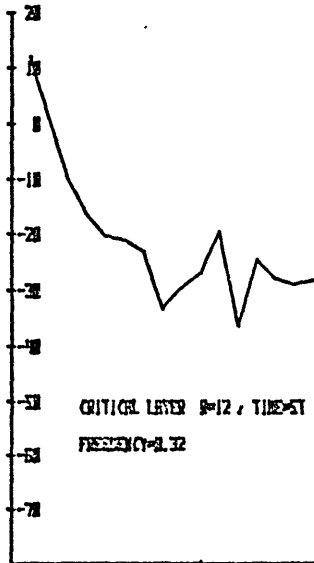
-a-

4-22 (a) Pressure time series near the critical level for
a run analogous with 2

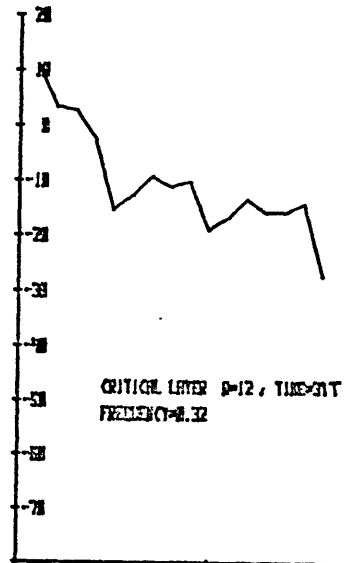
PROBE 1



b.



PROBE 2



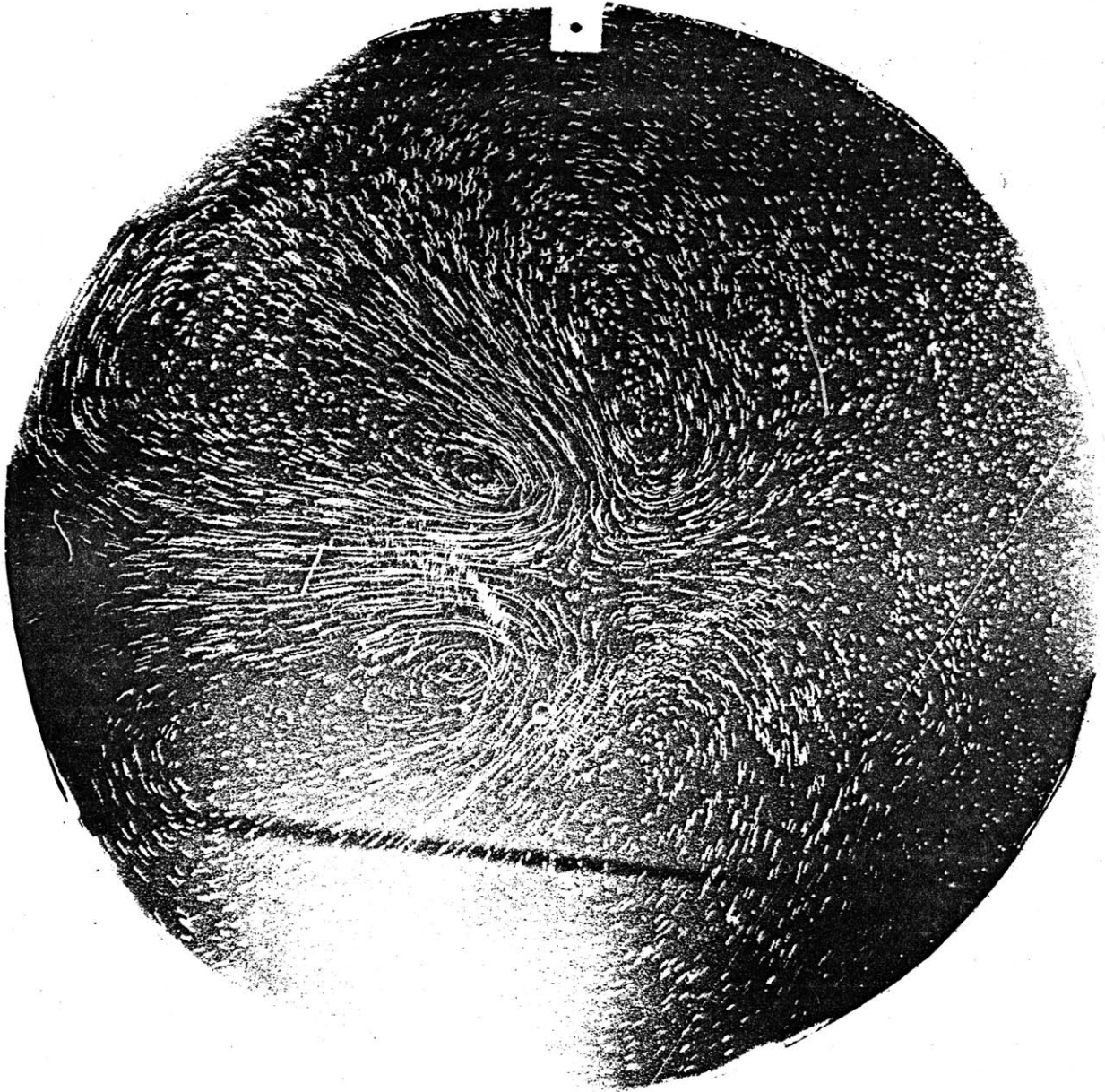
4-22 (b) Pressure autospectra of the above signal at $5T'$ and $31T'$, T' being the wave period.

PART FOUR

Some new results of stationary source-sink flows over a beta plane with meridional barriers are now presented. Stommel, Arons and Faller (1958) pioneered work in that direction by carrying out a remarkable series of experiments exhibiting the tortuous paths that dyed fluid had to follow to go from a source to a sink in a rotating pie-shaped basin with a paraboloidal free surface. These flow patterns are thought to be relevant primarily to the abyssal thermohaline circulation in the ocean. In the latter, the forcing is provided by localized sources of bottom water as for instance the Weddell Sea, the Labrador basin or the Norwegian Sea.

The emphasis in the present study was determined oddly enough by use of different techniques of flow observations which revealed unexpected features. By dyeing the fluid, Stommel et al. mainly interested in the actual mass transport, have put the emphasis on the particular time history of fluid parcels as they are expelled from the source. However, this leaves large regions of the flow field essentially unmapped. On the contrary Eulerian information was provided in our experiments. It highlighted different aspects of the flow and some effort had to be made to reconcile the two pictures. Moreover an investigation of the stability of the small amplitude circulation has brought to light some interesting properties about the relative stable position of stationary cyclones and anticyclones on a beta plane.

north

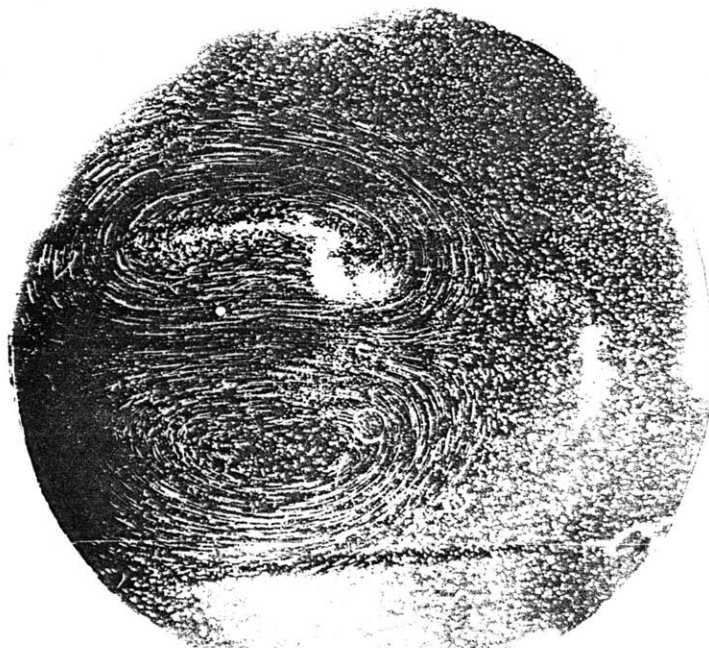


5-1 Time dependent response to an impulsive $\delta(t)$ function dipole in the sliced cylinder. Laboratory parameter values are $\Omega = 5.43$ rad/s, $\alpha = 0.2$, $H = 22$ cm.

north



north



5-2 The flow induced by a steady dipole

(a) transient

(b) steady state

Laboratory parameter values are $\Omega = 4.18$ rad/s,

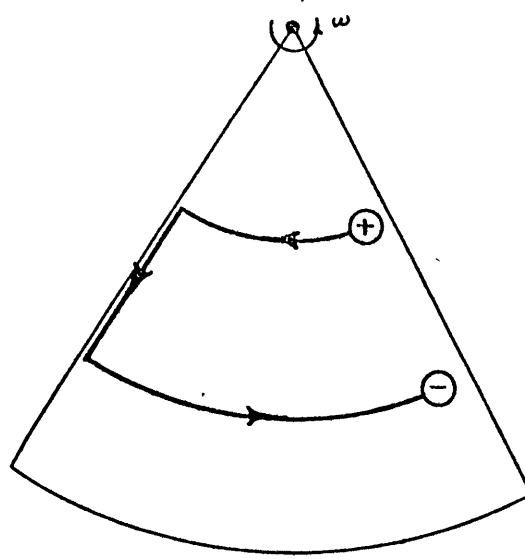
$\alpha = 0.095$, $H = 25$.

I. The small amplitude dipole circulation - Experiments and theory

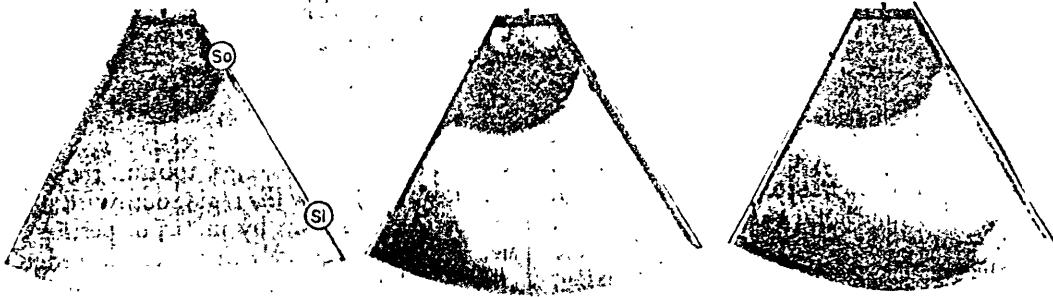
In the sliced cylinder geometry a sink was placed at a distance of 4 cm northward from the center of the basin. The source was situated symmetrically south. Figure 5-1 shows the initial fluid response to an impulsive $\delta(t)$ function dipole. It is included here because it illustrates some remarkable Rossby wave properties. The driving influence has been propagated rapidly to the west yet slowly to the east with considerable anisotropy in the flow. West of the driving, the crests are elongated zonally while more meridionally east of it. This observation is in agreement with what is known about the time dependent propagation of energy for small amplitude Rossby waves.

With steady forcing, the flow develops as in figure 5-2 which shows that the western boundary is a key feature in the evolution to a steady state. The steady flow lying exclusively west of the forced region consists of two counterrotating gyres whose center has been shifted to the west. Viewing the steady forcing as a time dependent one whose frequency goes to 0 explains the absence of flow east of the forced region since the group velocity points to the west. In this run carried out for a large rotation rate, the velocities are actually meridional over the source and the sink. Notice also the flow intensification that occurs near the western boundary. The picture that one gets from the flow seems to differ radically from the qualitative transport lines proposed by Stommel et al. This is recalled in figure 5-3 extracted from their paper. It is proposed to present first a theoretical explanation for our observations and then to reconcile simply the two sets of experiments.

In Part I, a vorticity equation has been derived for small quasi-geostrophic motions forced by vertical velocities imposed at the bottom



- a -



- b -

5-3 The results of Stommel et al. (1958)

(a) Transport lines

(b) Their experiments.

of the basin. The tilt of the lid being a small angle α , the requirement is that frictional terms and vertical motions are small at least of order α . Under these hypotheses, the interior motion is non divergent to zeroth order in α . A streamfunction ψ which satisfies the following steady vorticity equations may be introduced to describe the bulk of the motion.

$$R\nabla^2\psi + \beta\psi_x = \frac{-f_w}{H}(x,y)$$

(1)

$$\psi = 0 \quad \text{on the bounding walls}$$

As usual $R = 2\Omega E^{\frac{1}{2}}$ and $\beta = \frac{2\Omega\alpha}{H}$.

In (1) the scale L_F of the forcing function w is assumed to be large enough, so that lateral friction is negligible. The velocity of the flow is thought to be small enough such that nonlinear advection terms do not play any significant role. This requires that the nondimensional quantity $\frac{WH}{\Omega(\alpha L_F)^2}$ be much smaller than unity. The free length scale that comes out from the homogeneous part of (1) is $L_R = \frac{R}{\beta}$ specifying the scale at which friction becomes important compared to advection of planetary vorticity. It is, in fact, the width of Stommel's frictional Gulf Stream. If a denotes the radius of the basin, different regimes may be found according to the value of $\frac{R}{\beta a}$.

If $\frac{R}{\beta a}$ is much larger than unity, viscous effects are dominant and the flow pattern is the one produced by a steady dipole on an f -plane. It is analogous to the electric field produced by two equal and opposite charges, and completely symmetrical with respect to the meridional axis. The transport of water from the source to the sink is small and of order $E^{\frac{1}{2}}$ and achieved by the upper and lower Ekman layers exclusively.

The inertial regime when $\frac{R}{\beta a}$ is much smaller than unity is the one to be considered here. We are interested in dipole structure for which

the source-sink separation is large of order a typically. On the other hand the effective section of an individual source or sink introduces another length scale L_F much smaller than a . If $\frac{R}{\beta L_F}$ is smaller than unity, the gyre produced by one source (or sink) of size L_F has essentially the behavior of Stommel's wind driven gyre. Over the source, the Sverdrup balance holds and the flow is meridional to the south. Away from the forcing it turns west as a broad, inviscid zonal current. Two ingredients are necessary for the return flow: a western wall and Ekman friction however small. A swift and narrow northward current develops along the wall and turns east again at the latitudes where the forcing vanishes. The circulation is similar around the sink. The other limit when $\frac{R}{\beta L_F}$ is large does not seem to have been previously studied. Because there are important differences with the above case, the solution will be presented thoroughly. The simplest way to make $\frac{R}{\beta L_F}$ small is to take a δ function for the forcing function W . The problem is then to find a Green's function for Stommel's equation (1). We first look at the solution generated by one sink placed at $x = x_0, y = y_0$. Setting $\delta = \frac{\beta}{2R}$, one makes the following change of variable in equation (1): $\psi = G e^{-\delta(x - x_0)}$. G now obeys the following nondimensional equation:

$$(2) \quad \nabla^2 G - \delta^2 G = -2\pi\delta(x - x_0, y - y_0).$$

This elliptic Helmholtz equation has to be solved in the circle $r = a$. Following the general methods of Courant and Hilbert (1962) one introduces first the Green's function valid in an infinite medium. Thus we set

$$G = K_0(\delta R) + V(\underline{x} \mid \underline{x}_0)$$

where K_0 is the zeroth order modified Bessel function, and

$$R = [(x - x_0)^2 + (y - y_0)^2]^{\frac{1}{2}}$$

The function V satisfies now the following Dirichlet problem

$$\nabla^2 V - \delta^2 V = 0 \quad (3)$$

$$V = -K_0 \quad \text{on } r = a$$

The idea is to look for a solution of the form:

$$(4) \quad V = \oint_{r=a} \tau \frac{\partial K_0}{\partial n} \underline{dl} \quad \text{where } V \text{ is}$$

represented as a double layer potential with dipole density τ on the boundary, \vec{n} is the outer normal at the boundary. To determine τ ,

the limit of the potential V as the boundary is approached from the interior is sought. One may find that the following equation holds at the boundary:

$$(5) \quad \oint_{r=a} \tau \frac{\partial K_0}{\partial n} \underline{dl} = +\pi\tau - K_0 \quad \text{on } r = a$$

This is a Fredholm integral equation of the second kind for τ .

Introducing polar coordinates it is easily solved by expanding the terms of (5) in Fourier series. The value of τ is then introduced into (4) to calculate V . The complete solution of (1) for a δ -function source and sink situated at $(r_0, \pi/2)$ and $(r_0, -\pi/2)$ turns out to be:

$$r < r_0: \quad \psi = e^{-\delta r \cos \theta} \sum_{p=0}^{\infty} (-1)^p \sin(2p+1)\theta \cdot I_{2p+1}(\delta r) [K_{2p+1}(\delta r_0) +$$

$$I_{2p+1}(\delta r_0) K_{2p+1}(\delta a) H_{2p+1}(\delta a)]$$

(6)

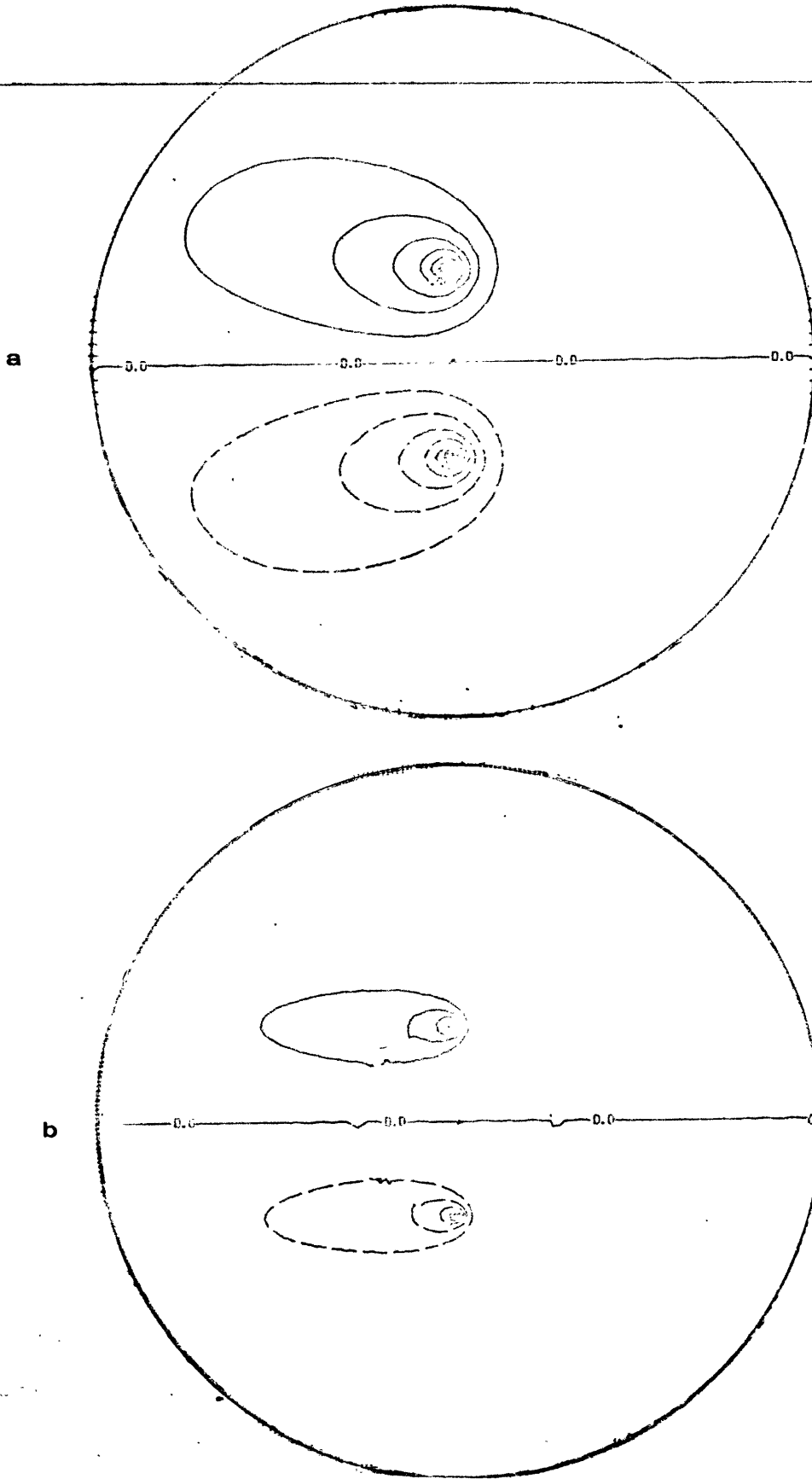
$$r > r_0: \quad \psi = e^{-\delta r \cos \theta} \sum_{r=0}^{\infty} (-1)^p \sin(2p+1)\theta \cdot I_{2p+1}(\delta r_0) [K_{2p+1}(\delta r) +$$

$$I_{2p+1}(\delta r) K_{2p+1}(\delta a) H_{2p+1}(\delta a)]$$

where I_p , K_p are the usual modified Bessel functions and

$$H_{2p+1}(\delta a) = \frac{\delta a [K_{2p+2}(\delta a) + K_{2p}(\delta a)]}{1 - a\delta I_{2p+1}(\delta a) [K_{2p+2}(\delta a) + K_{2p}(\delta a)]}$$

This is admittedly an awkward solution to deal with, although the flow field that it represents is very simple. Note that the summation involves terms symmetric with respect to the y -axis and antisymmetric with respect to the x -axis. Thus the east-west asymmetry is provided solely by the exponential term in front. Notice also that the solution (6) being bounded at infinity is valid in an infinite basin. The solution (6) was numerically evaluated and is exhibited on figure 5-4 for various values of δ . The only regions of intense flow are now situated east of the forcing and no western boundary layer develops as contrasted with the preceding case. In the intermediate limit when $\frac{R}{\beta L_F}$ is order one, rapid flows are thus likely to develop both at the western wall and around the forcing region. These limits describe most of what happens in the experiments. When going from low to high rotation rate, the parameter



5-4 The streamline pattern of theoretical solution (6)

(a) $\delta = 0.15$

(b) $\delta = 0.58$

$\frac{R}{\beta L_F}$ decreases, keeping L_F fixed. This enables us to observe the limits described previously.

The intense gyres found in both theories and experiments do not seem to have been noted by Stommel et al. The reasons for the apparent discrepancies are interesting. Their schematic diagram (figure 5.3 (a)) for the transport lines corresponds to the singular limit when the size of the source sink region and the frictional effects tend to zero. The gyres considered in this study correspond to a finite vorticity appearing when either of the above is non-zero. When the flow is inviscid and the source-sink regions have dimension L_F , the interior vorticity is order $w/\alpha L_F$. When the flow is viscous, driven by source-sink of infinitesimal size, the vorticity is of order $w/(\frac{\nu}{\Omega})^{1/2}$. In both cases it leads to intense gyres. One wonders however how the fluid is transported from the source to the sink in these symmetrical counter rotating gyres with a zonal streamline ($\psi = 0$) isolating the source and sink region. The required transport is achieved because of the meridional depth changes. The contours of the transport $H(y)\vec{u}$ are no longer symmetrical. They originate from the source, turn west, bunch together near the western wall and come back to the sink. When friction and finite size of source-sink are neglected they would exhibit the behavior suggested by Stommel et al. Because the net transport from the source to the sink is small (of order α) compared say to the order one recirculation transport in one of our gyres, it cannot be detected from our short exposure streak photographs which emphasize the order one nondivergent motion. On the other hand Lagrangian dye tracers used by Stommel et al. (figure 5-3 (b)) paint the continuous time history of a set of fluid parcels and may reveal the sluggish transport that occurs from the northern to the southern basin

via the western boundary. From their photographs there is some evidence, however, that gyres of the kind discussed here were also present. The persistence of these gyres was also found in our experiments when the source and the sink were placed near the northern and southern boundary respectively. These experiments suggest caution when comparing the oceanic abyssal flow with theory. The net transport from source to sink may appear to be very small masked by intense flow recirculating gyres. Consideration of only one branch of these gyres would lead to serious errors. Because both bottom friction and size of source-sink are probably non-negligible in the ocean, one must emphasize the need for evaluating mean transport over large regions.

II. The finite amplitude dipole circulation

The behavior of the gyres when augmenting the mass flux was investigated experimentally with source-sink separation fixed at $L = 3$ cm. The meridional extension of the gyres were thus smaller than the diameter of the basin (62 cm). When the flow reaches speed such that $U/\beta L^2$ becomes order 1, the non-linear terms become important, and interesting asymmetries are found. When the source is south and the sink north (configuration A) the flow is absolutely stable and intense steady circulation can be induced. On the other hand, the reverse configuration (B) when the sink is south and the source north leads to an instability of the flow as soon as $\frac{U}{\beta L^2}$ is order one. That such asymmetry may occur results from consideration of the relevant nonlinear steady vorticity equation:

$$(7) \quad J(\psi, \nabla^2 \psi) + \beta \psi_x = -R \nabla^2 \psi - \frac{f w}{H} .$$

In fact the presence of the Jacobian in (7) shows that (7) is not invariant through the transformation $\psi \rightarrow -\psi, w \rightarrow -w$.

The free inviscid part of equation (7), when the right-hand side is neglected, has been studied by different authors. Fofonoff (1954) has found inertial solutions in a closed rectangular basin. The potential vorticity is constant over a streamline for such solutions. Fofonoff shows that very different behavior of the flow occurs according to the sign of the constant of proportionality between q and ψ . When the sign is positive the flow consists of eddies covering the entire ocean which are in fact stationary Rossby waves superimposed on an eastward flow. When the sign is negative, the mean flow consists of an interior broad westward flow with intense return flow to the east along each zonal boundary. This generation of zonal jets was also found in a numerical integration of the complete equation (7) by Veronis (1965) who looked specifically at the effects of nonlinearity upon Stommel's classical solution. These two studies indicate that an anticyclone (resp. cyclone) is stabilized by a zonal wall lying northward (resp. southward). The middle zero streamline between source and sink may be thought of as acting as a rigid wall. It is then significant to realise that the stable configuration A is consistent with the above results.

M. Stern (1975) having in mind eddies rather than gyres has developed isolated free inertial solutions on a beta plane. Furthermore, the dipole must be bounded by a free streamline across which the vorticity has to change discontinuously. This is because the nonlinear quadratic terms cannot balance the smaller linear beta term at infinity. This constraint rules out modons-dipole corresponding to our (unstable) configuration B. All these results seem to suggest that indeed there must be a good

physical reason for the instability that we observed. Rather than developing a complicated numerical study of the instability, it is wished to enhance and isolate physical mechanisms leading to the observed behavior.

As we have seen part of the vorticity equation (7) may be solved analytically. However the complete equation is difficult to deal with because one cannot ascribe à priori the relative importance of the various terms to certain definite regions of space as is customary with perturbation methods. In the following, it is wished to show that a tendency for potential vorticity conservation will occur over certain selected streamlines. The solution is assumed to be known either from theory or experiment. Equation (7) may be rewritten as:

$$(8) \quad \underline{u} \cdot \nabla q + Rq = R\beta V - \frac{fw}{H}$$

In the usual way (8) may be integrated following a fluid parcel whose position is S_0 over a given steady streamline and potential vorticity q_0 at $t = 0$. At time t the potential vorticity of the parcel will be:

$$q = q_0 e^{-RT} + R\beta \int_0^t v(t', S_0) e^{R(t'-t)} dt' - \frac{f}{H} \int_0^t w(t', S_0) e^{R(t'-t)} dt'$$

The motion being steady the particle will come back to its original position with the same potential vorticity q_0 after a revolution time T . We thus have:

$$(9) \quad q_0 (1 - e^{-RT}) = R\beta \int_0^T v(t', S_0) e^{R(t'-t)} dt' - \frac{f}{H} \int_0^T w(t', S_0) e^{R(t'-t)} dt'$$

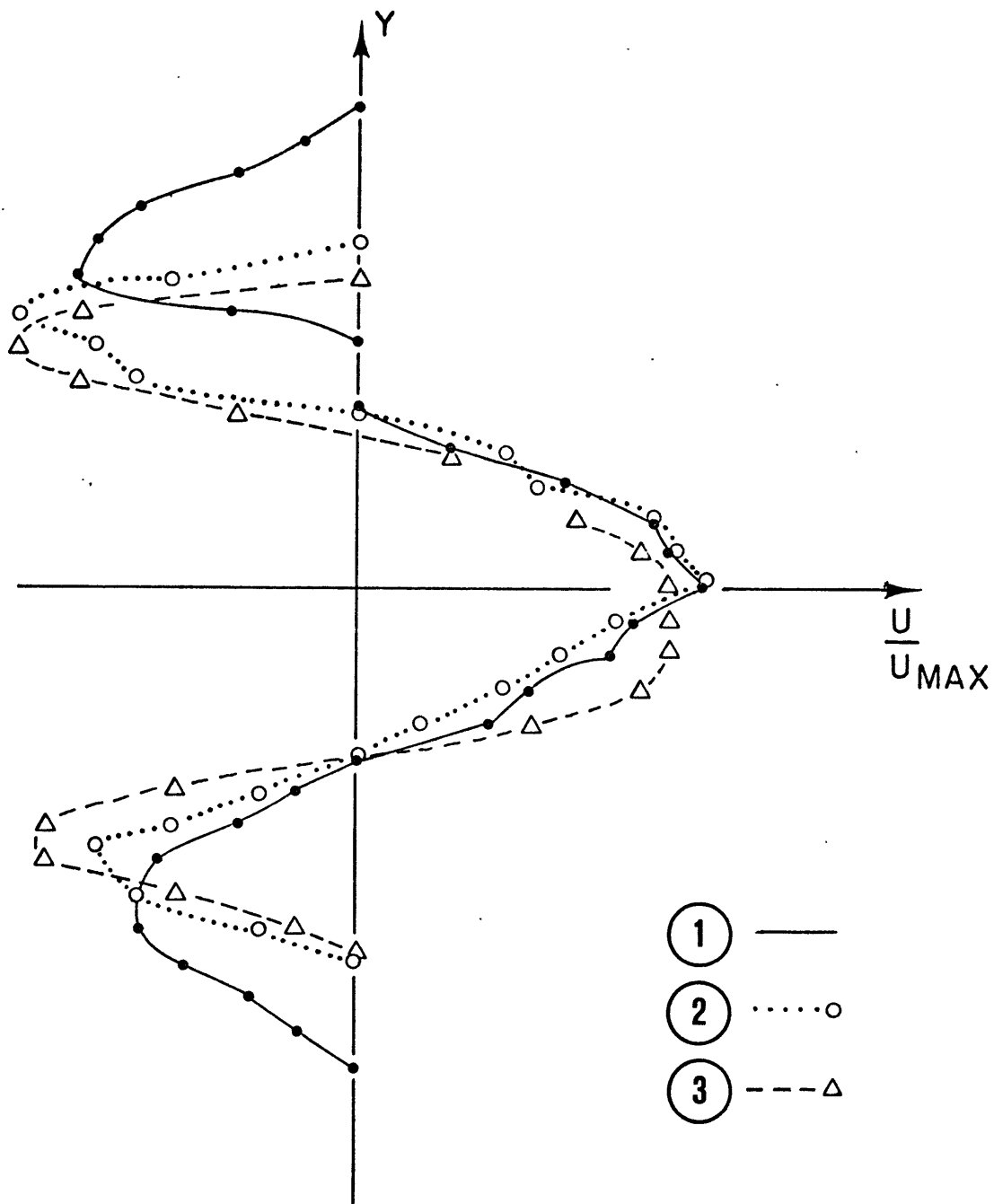
~~In general the right-hand side of (9) is a function of S_0 the~~
 initial position of the parcel on the streamline and this implies that
 q_0 is not conserved over the streamline. Now consider a fast streamline
 (if any) for which RT is much smaller than unity. Expanding (9) in
 that limit, gives to leading order in RT :

$$(10) \quad RT \cdot q_0 = - \frac{f}{H} \int_0^T w(t', S_0) dt' \quad \text{for } RT \ll 1.$$

It is clear in this case that the above Lagrangian integral is independent of S_0 . This implies that q_0 is constant over such a streamline although the forcing is non negligible. This result has some consequence for our experiments. It means that when nonlinear terms are important compared to the viscous terms, there exist streamlines in the flow for which the potential vorticity will be conserved.

Figure 5-5 shows meridional flow profiles for turns which were carried out with the stable configuration A. A tendency for the broadening of the north and south westward flow with increasing forcing amplitude can be detected by comparing Run #1 to Run #3. Following a fluid parcel, initially near the middle zero streamlines over a swift cyclonic streamline (for which $RT \ll 1$) indicates that relative vorticity and hence shear will decrease over the northern westward flow. In the same way the shear of the anticyclone will decrease on its southward side.

Potential vorticity consideration may show in a heuristic manner why configuration B is effectively unstable. The anticyclone is lying north and the cyclone south. A fluid parcel in the middle westward flow with negligible vorticity gains anticyclonic vorticity when moving north in the anticyclone making it impossible for quiet fluid to exist north



5-5 Meridional flow profiles with stable configuration A.

Laboratory parameter values are the following: L

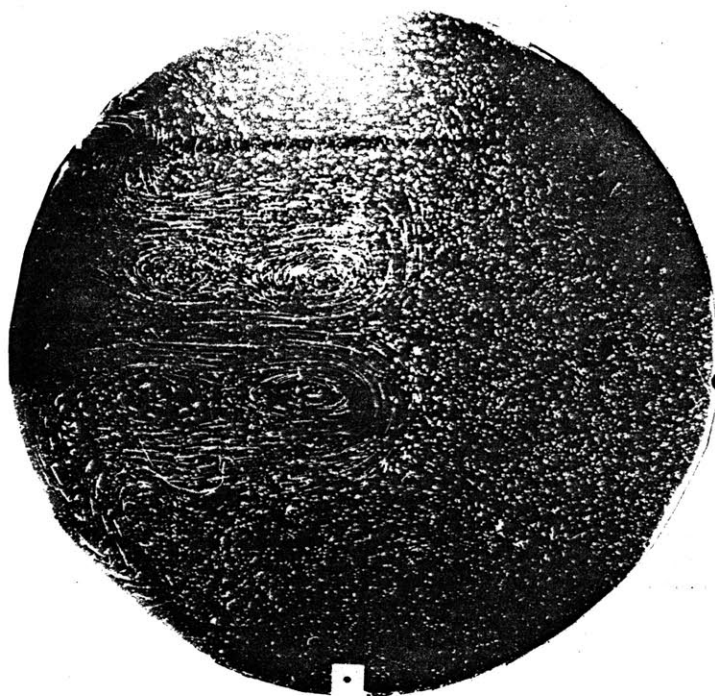
the source-sink distance is kept fixed at 8 cm

	$\frac{U_{MAX}}{\beta L^2}$	$\frac{U_{MAX}}{RL}$	$L_R = \frac{R}{\beta}$	$L_\beta = \left(\frac{U_{MAX}}{\beta}\right)^{\frac{1}{2}}$
①	1.53	15.2	0.8	9.9
②	0.84	7.6	0.87	7.3
③	0.27	6.8	0.3	4.2

of the anticyclone. The same argument applies also for the cyclone and therefore the flow has to become unsteady to escape constraints.

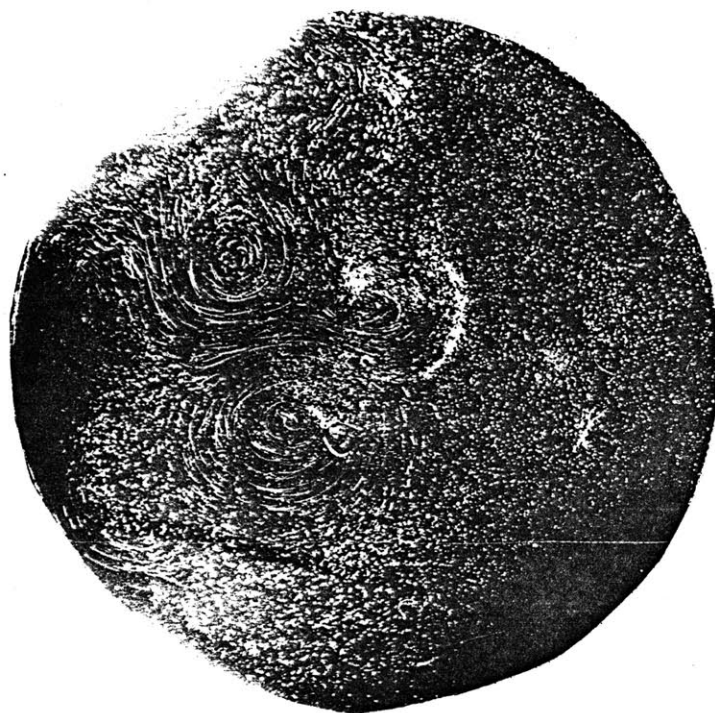
Figures 5-6 show two unstable runs with configuration B. The first one for an order one value of $U/\beta L^2$ reveals the typical inertial overshoot that occurs in the western boundary layer. The second one for which $U/\beta L^2$ is 10 times larger shows the apparition of time dependent eddies in the interior. Finally the heuristic argument advanced for explaining the instability suggests that the proximity of the north and south solid boundaries should stabilize the inertial flow in configuration B, by suppressing the quiet regions north and south of the gyres. This was indeed observed in the experiments with the source and sink situated much closer to the northern and southern boundaries respectively.

north



.a.

north



.b.

5-6 Two runs with unstable configuration B.

(a) $U/\beta L^2 = 1.2$

(b) $U/\beta L^2 = 12.7$

CONCLUSION

Specific conclusions have already been provided at the end of each particular section. Some points are worth emphasizing here.

The course of this work has revealed the feasibility of studying two dimensional turbulence in the laboratory by using sources and sinks acting at the bottom of the fluid. This allows vorticity to be generated by the vertical stretching and squashing of the vortex lines. The influence of beta in various geometries has been shown and it is hoped that in geophysical situations the results of the present experiments will help in unraveling the signature of large scale barotropic mixing processes from a wealth of other natural phenomena. In view of our present results and the inherent difficulties of numerical models in reproducing the richness of scales of turbulent flows, laboratory experiments may prove to be a valuable method of studying two dimensional turbulence. Although no such limitation of scales appears in a laboratory flow, the measurements remain difficult. To bring the usefulness of a laboratory model to its best, considerable effort should be aimed at improving the recording techniques of small scale, slow flow. This is a prerequisite to making accurate, quantitative observations.

The more deterministic experiments focusing on certain finite aspects of topographic Rossby waves show without doubt the far reaching consequences of thinking of wave driven mean flows in terms of potential vorticity mixing. They suggest the need of more theoretical work to elucidate the ways by which potential vorticity transport occurs at forced latitudes.

Nonlinearity in the Rossby wave mean flow interaction enables the wavemomentum to be carried through the critical level and deposited into the steady state mean flow. At the same time very fine structure is

generated within the critical layer. It therefore seems that the primary effect of the finite amplitude waves will be to broaden the effective region of momentum transfer without altering the direction of the ultimate transfer.

The last abyssal circulation experiment has warned us of the difficulties which can arise when one neglects the generation of vorticity caused by friction or by the finite size of the sources. Although the transport predictions are essentially unaffected, the lateral structure of the flow may be richer than implied by a single jet running from source to sink. The asymmetry of the flow stability properties illustrates the peculiar effects which arise from potential vorticity considerations.

Real fluid experiments are attractive for their economy and their ability to isolate important low frequency physical processes which may later be explained within the framework of quasigeostrophic theory. There are a number of experiments that are a natural outgrowth of the present work. However for closer comparisons with geophysical phenomena, the addition of stratification and short scale topography should be given the highest priority.

References

- Batchelor, G. K., 1953
Theory of Homogeneous Turbulence. Cambridge University Press.
- Batchelor, G. K., 1969
 Computation of the energy spectrum in homogeneous two dimensional turbulence. The Physics of Fluids, Supplement II, 233-239.
- Beardsley, R. C., 1969
 A laboratory model of the wind driven ocean circulation. J. Fluid Mech., 38, 255.
- Beardsley, R. C., 1975
 The sliced cylinder laboratory model of the wind driven ocean circulation.
 Part 2. Oscillatory forcing and Rossby wave resonance. J. Fluid Mech., 69, part 1, 41-64.
- Béland, M., 1976
 Numerical study of the nonlinear Rossby wave critical level development in a barotropic zonal flow. J. Atmos. Sci., 33, 2066-2078.
- Benjamin, R., and J. Feir, 1967
 The disintegration of wave trains on deep water. J. Fluid Mech., 27, part 3, 417-430.
- Benney, D. J., and R. F. Bergeron, 1969
 A new class of nonlinear waves in parallel flows. Studies Appl. Math., 48, 181-204.
- Booker, J. R., and F. P. Bretherton, 1967
 The critical layer for internal gravity waves in a shear flow. J. Fluid Mech., 27, 513-539.
- Dickinson, R. E., 1970
 Development of a Rossby wave critical level. J. Atmos. Sci., 27, 627-633.
- Drazin, P. G. and L.N. Howard, 1966
 Hydrodynamic stability of parallel flows of inviscid fluid. Advances in Applied Mechanics, vol 9, 1-89.
- Eliassen, A., and E. Palm, 1960
Geof. Publ., 22, 3, 1.
- Fjortoft, R., 1953
 On the changes in the spectral distribution of kinetic energy for two dimensional, nondivergent flow. Tellus, 5, 3, 225-230.

References (cont.)

- Fofonoff, N. P., 1954
Steady flow in a frictionless homogeneous ocean. J. Mar. Res.,
13, 254-262.
- Freeland, H., P. Rhines, H. T. Rossby, 1975
Statistical observations of the trajectories of neutrally buoyant
floats in the North Atlantic. J. of Mar. Res., 33, 3, 383-404.
- Greenspan, H. P., 1969
A note on the laboratory simulation of planetary flows.
Studies Applied Math, 48, 2, 147-152.
- Gould, W. J., W. J. Schmitz, and C. Wunsch, 1974
Preliminary field results for a Mid Ocean Dynamics Experiment
(MODE-0). Deep-Sea Res., 21, 911-931.
- Howard, L. N., 1964
The number of unstable modes in hydrodynamic stability problems.
J. de Mécanique, 3, 433-443.
- Howard, L. N., and P. G. Drazin, 1964
On instability of parallel flows of inviscid fluid in a rotating
system with variable Coriolis parameter. J. of Math. and Physics,
nd 63, no. 2.
- Ibbetson, A., and R. E. Frazel, 1965
W.H.O.I. Ref. 65-41 (unpublished manuscript).
- Kraichnan, R., 1967
Inertial ranges in two dimensional turbulence. Physics of Fluids,
vol. 10, 7, 1417-1423.
- Kuo, H., 1949
Dynamic instability of two dimensional non divergent flow in a
barotropic atmosphere. J. Met., 6, 105-122.
- Lighthill, M. J., 1967
On waves generated in dispersive system by travelling forcing
effects, with applications to the dynamics of rotating fluids.
J. Fluid Mech., vol. 27, part 4, 725-752.
- Lilly, D. K., 1969
Numerical simulation of two-dimensional turbulence. Physics of
Fluids, Supp. II, 240-249.
- Lilly, D. K., 1970
Numerical simulation of developing and decaying two-dimensional
turbulence. J. Fluid Mech. (1971) vol. 45, part 2, 395-415.

References (cont.)

- Lilly, D. K., 1972
Numerical simulation studies of two-dimensional turbulence.
Geophys. Fluid Dyn., vol. 3, 289-319.
- Lin, C. C., 1955
Theory of Hydrodynamic Stability. Cambridge University Press.
- Lindzen, R. S., and J. R. Holton, 1968
A theory of the quasibiennial oscillation. J. Atmos. Sci., 25,
1095-1107.
- McGoldrick, L. F., 1969
Technical Report No. 3, Department of the Geophysical Sciences,
University of Chicago (unpublished manuscript).
- Pedlosky, J., 1965
A study of the time dependent ocean circulation. J. Atmos.
Sciences, vol. 22, 267-272.
- Pedlosky, J., and H. P. Greenspan, 1967
A simple laboratory model for the oceanic circulation. J. Fluid
Mech., 27, 291-304.
- Phillips, N. A., and A. Ibbetson, 1967
Some laboratory experiments on Rossby waves with application to
the ocean. Tellus, 19, 81-88.
- Rhines, P. B., 1975
Waves and turbulence on a Beta-plane. J. Fluid Mech., vol. 69,
part 3, 417-443.
- Rhines, P. B., 1977
Dynamics of unsteady currents. The Sea, Vol. 6, Wiley and Sons, Inc.
- Richman, J., 1976
Kinematics and energetics of the mesoscale mid-ocean circulation:
MODE. Ph.D. Thesis, W.H.O.I.-M.I.T. Joint Program in Oceanography.
- Schmitz, W. J., Jr., 1977
Observations of the vertical distribution of low frequency kinetic
energy in the western North Atlantic. Submitted to J. Mar. Res.
- Stern, M., 1975
Minimal properties of planetary eddies. J. Mar. Res., vol. 33,
no. 1, 1-13.
- Stommel, H., A. B. Aarons, and A. J. Faller, 1958
Some examples of stationary planetary flow patterns in bounded
basins. Tellus, 10, number 2

References (cont.)

- Taylor, G. I., 1915
Eddy motion in the atmosphere. Phil. Trans. Roy. Soc. A. 240,
pp 1-26.
- Taylor, G. I., 1921
Diffusion by continuous movements. Proc. Lond. Math. Soc.,
ser. 2, vol. 20 pp 196-212.
- Thompson, R., 1971
Topographic Rossby waves at a site north of the Gulf Stream.
Deep-Sea Research, 18, 1-19.
- Veronis, G., 1966
Wind-driven ocean circulation. Part 2. Numerical solutions of
the non linear problems. Deep-Sea Res., 13, 31-55.
- Whitehead, J. A., 1975
Mean flow driven by circulation in a β -plane. Tellus, 27, 358-364.

Biographical Note

The author was born on September 25, 1948 at Bordeaux, FRANCE. He graduated from Ecole Supérieure de Physique et Chimie de la Ville de Paris in July 1973. This same month he married Edith Nicolet. Both moved to New England in September 1973. Interest in Oceanography grew from intensive cruising and racing in "La Manche" and many thanks are due to Guy for providing this unique opportunity.